Optimization of Nonlinear Dynamics in Nanomechanical Resonators

Li, Z.

DOI
10.4233/uuid:73a99850-8097-404b-af60-8c4b631b37a9

Publication date
2025

Document Version
Final published version

Citation (APA)
Li, Z. (2025). *Optimization of Nonlinear Dynamics in Nanomechanical Resonators*. [Dissertation (TU Delft), Delft University of Technology]. https://doi.org/10.4233/uuid:73a99850-8097-404b-af60-8c4b631b37a9

Optimization of Nonlinear Dynamics in Nanomechanical Resonators

Zichao Li

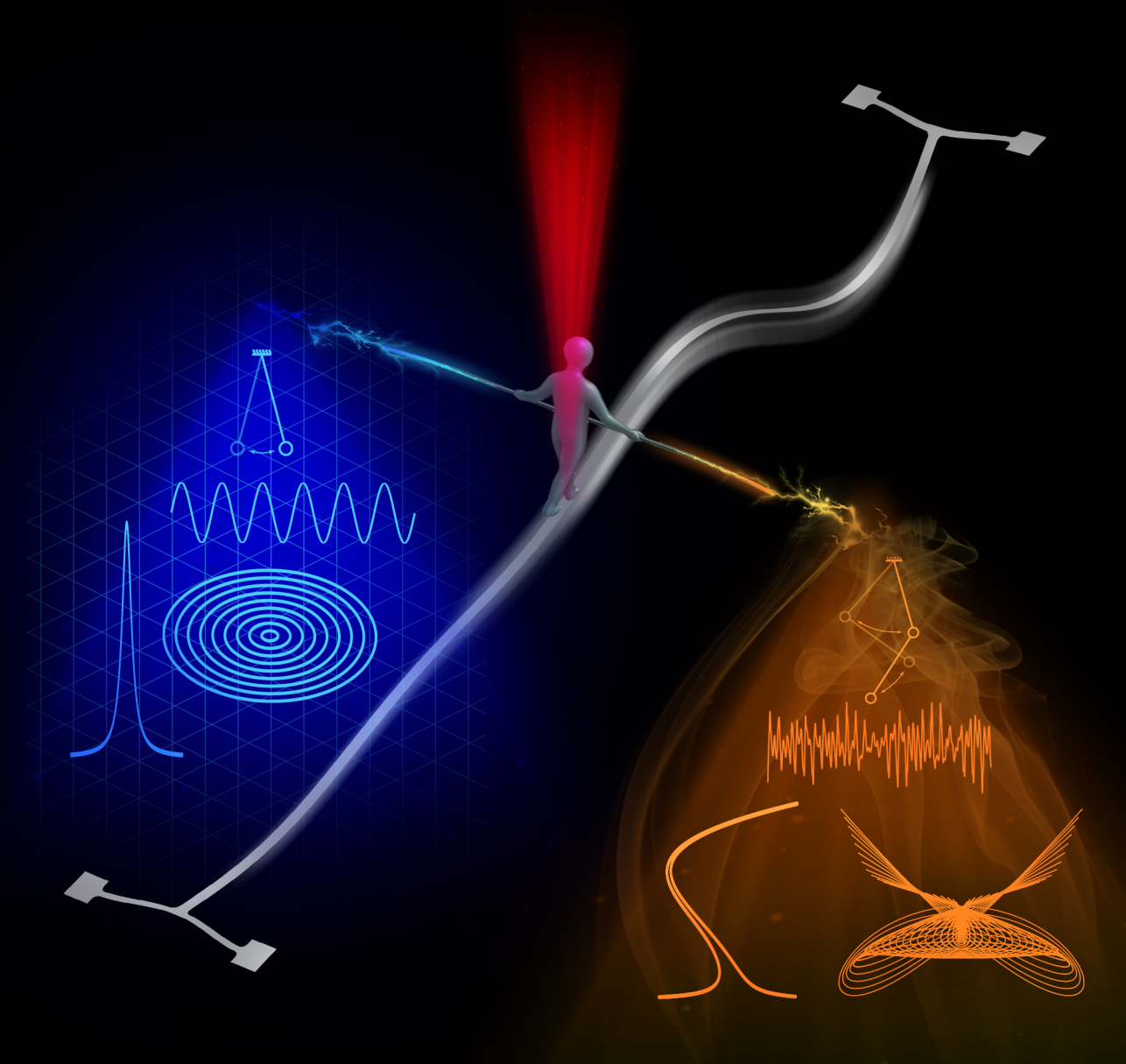

Optimization of Nonlinear Dynamics in Nanomechanical Resonators

Optimization of Nonlinear Dynamics in Nanomechanical Resonators

Dissertation

for the purpose of obtaining the degree of doctor
at Delft University of Technology
by the authority of the Rector Magnificus, prof. dr. ir. T.H.J.J. van der Hagen,
chair of the Board for Doctorates
to be defended publicly on Tuesday 13 May 2025 at 15:00 o'clock

by

Zichao Li

Master of Engineering in Aerospace Propulsion Theory and Engineering,
Beihang University,
born in Tianjin, China.

This dissertation has been approved by the promotors

promotor: Prof. dr. P. G. Steeneken
promotor: Dr. F. Alijani
promotor: Dr. A. M. Aragón

Composition of the doctoral committee:

Rector Magnificus,	Chairperson
Prof. dr. P. G. Steeneken,	Delft University of Technology, promotor
Dr. F. Alijani,	Delft University of Technology, promotor
Dr. A. M. Aragón,	Delft University of Technology, promotor
Independent members:	
Prof. dr. ir. H. S. J. van der Zant,	Delft University of Technology
Prof. dr. S. W. Shaw,	Florida Institute of Technology
Prof. dr. S. Schmid,	Vienna University of Technology
Dr. A. Eichler,	Federal Institute of Technology Zurich
Prof. dr. U. Staufer,	Delft University of Technology, reserve member

Keywords: Nonlinear dynamics, nanomechanics, optimization, support design, high-Q resonators
Printed by: ProefschriftMaken
Cover art: A figure walks on a nanostring while holding a pole, navigating the balance between linear and nonlinear dynamics. Concept generated by Zichao Li with ChatGPT.

ISBN 978-94-6384-776-6

An electronic version of this dissertation is available at
http://repository.tudelft.nl/.

Unify knowledge and action.

Yangming Wang, AD 1472-1529, China (Ming Dynasty)

Contents

SUMMARY

Most micro- and nanomechanical devices are designed to operate within the linear dynamic range by using simple geometries, primarily due to the limited knowledge in utilizing nonlinearity and constraints in fabrication techniques. However, it is anticipated that the scope of applications and fundamental research can be significantly expanded, if these tiny systems can be precisely engineered to account for and exploit their various nonlinear dynamic behaviors. This thesis provides a comprehensive study on the optimization of dynamical properties of high-Q nanomechanical resonators, spanning from linear to nonlinear dynamics and evolving from single-mode to multi-mode analysis.

We first give an introduction to the development of micro- and nanomechanical resonators in Chapter 1. We focus on their unique mechanics, including very low dissipation and strong nonlinearities. Furthermore, we elaborate on the motivation behind this thesis and the need for linking engineering optimization with micro- and nanomecahincal resonators. Followed by Chapter 2, we elaborate on the methodology we use throughout this thesis, including fabrication techniques of nanomechanical Si_3N_4 devices, characterization approaches by optical measurements, and modeling procedures for structural dynamics. Among all methodologies, we highlight the Finite Element (FE)-based Reduced Order Models (ROMs) that can accurately capture the geometric details and boundary conditions, which facilitate the design of resonators with predictable dynamical properties.

We start from investigating linear dynamics of Si_3N_4 nanostrings in Chapter 3, where the tuning effects of their soft-clamping supports on resonance frequency and Q-factor are evaluated. We experimentally and theoretically reveal a trade-off between maintaining high stress and low stiffness of the supports in designing high-Q resonators fabricated with initial strain. By optimizing this trade-off with our soft-clamping design, we obtain a 50% enhancement of Q-factor compared to doubly-clamped string resonators. With stronger drive levels, in Chapter 4, we show that the nonlinear dynamics can also be substantially tailored by soft-clamping supports. Through careful engineering of support geometries, we introduce softening nonlinearity by stress-induced buckling, allowing precise control over the nonlinear dynamic responses in doubly supported nanostrings, which conventionally exhibit hardening behaviors.

Based on the accurate modeling of both linear and nonlinear dynamics that is validated by experiments, we integrate our FE-based ROM technique with a derivative-free optimization algorithm for the design of nonlinear mechanical resonators in Chapter 5. By optimizing the support's geometry of our nanostrings, we show that the proposed methodology is not only capable of handling a single optimization goal, but also multiple conflicting objectives, such as the simultaneous enhancement of Q-factor and the Duffing constant. Besides, we generate Pareto frontiers that visualize the trade-offs among

multiple optimization objectives, verify the optimized results with brute-force simulations and validate the numerical framework with experiments.

Apart from the dynamics in a single mode, we observe modal interactions between multiple vibrational modes of our nanostrings in the strong nonlinear regime. In Chapter 6, we demonstrate that soft-clamping techniques, commonly utilized to achieve high-Q resonators, can be employed to engineer mode coupling. We verify the analytically derived two-degree-of-freedom system between the lowest two out-of-plane modes by FE-based ROMs and experiments. We further reveal the significant impact of multi-mode interactions on the nanostrings' frequency response, demonstrating additional opportunities to tailor the nonlinear dynamics of mechanical resonators facilitated by soft clamping. Moreover, we highlight the design potential of soft-clamping supports through the geometric optimization of two-mode coupling, showcasing the effective Duffing constant of the driven mode can be increased by 70%, as well as the onset of mode coupling can be geometrically programmed to either facilitate or inhibit its occurrence.

We conclude all works presented for achieving the optimization of nonlinear dynamics in nanomechanical resonators, and give an outlook for future directions in Chapter 7.

SAMENVATTING

De meeste micro- en nanomechanische apparaten zijn ontworpen om in het lineaire gebied te werken door het gebruik van simpele geometrieën, voornamelijk vanwege een gelimiteerde kennis in het gebruiken van niet-lineariteiten en beperkingen in fabricagetechnieken. Er wordt echter verwacht dat de reikwijdte van de toepassingen en het fundamentele onderzoek aanzienlijk kan worden uitgebreid als deze kleine systemen nauwkeurig kunnen worden ontworpen om rekening te houden met hun verschillende soorten niet-lineair dynamisch gedrag en deze te benutten. Dit proefschrift biedt een uitgebreide studie naar de optimalisatie van dynamische eigenschappen van nanomechanische resonatoren met een hoge Q-factor, variërend van lineaire tot niet-lineaire dynamica en uitbreidend van single-mode- naar multi-mode-analyse. We geven eerst een introductie tot de ontwikkeling van micro- en nanomechanische resonatoren in Hoofstuk 1. We richten ons op hun unieke mechanica, waaronder zeer lage dissipatie en sterke niet-lineariteiten. Verder gaan we dieper in op de motivatie achter deze thesis en de noodzaak om technische optimalisatie te koppelen aan micro- en nanomechanische resonatoren. Gevolgd door Hoofstuk 2, gaan we dieper in op de methodologie die we in deze thesis gebruiken, waaronder fabricagetechnieken van nanomechanische Si_3N_4-apparaten, karakteriseringsmethodes door optische metingen en modelleringsprocedures voor structurele dynamica. Van alle methodologieën benadrukken we de op Finite Element (FE) gebaseerde Reduced Order Models (ROM's) die nauwkeurig de geometrische details en randvoorwaarden kunnen vastleggen, wat het ontwerp van resonatoren met voorspelbare dynamische eigenschappen vergemakkelijkt.

We beginnen met het onderzoeken van lineaire dynamica van Si_3N_4 nanostrings in Hoofstuk 3, waar de effecten van hun soft-clamping supports op resonantiefrequentie en Q-factor worden geëvalueerd. We onthullen experimenteel en theoretisch een afweging tussen het behouden van hoge spanning en lage stijfheid van de supports bij het ontwerpen van resonatoren met een hoge Q-factor die zijn gefabriceerd met initiële spanning. Door deze afweging te optimaliseren met ons soft-clamping ontwerp, verkrijgen we een verbetering van 50% van de Q-factor vergeleken met dubbel ondersteunde stringresonatoren. Met sterkere aandrijfniveaus laten we in Hoofstuk 4 zien dat de niet-lineaire dynamica ook substantieel kan worden aangepast door soft-clamping supports. Door zorgvuldige engineering van supportgeometrieën introduceren we verzachtende niet-lineariteit door stress-geïnduceerde knik, wat nauwkeurige controle over het niet-lineaire dynamische gedrag in dubbel ondersteunde nanostrings mogelijk maakt, die conventioneel verhardingsgedrag vertonen. Gebaseerd op het nauwkeurig modelleren van zowel lineaire als niet-lineaire dynamica die gevalideerd is door experimenten, integreren we onze FE-gebaseerde ROM-techniek met een optimalisatiealgoritme zonder afgeleiden voor het ontwerp van niet-lineaire mechanische resonatoren in Hoofstuk 5. Door de ondersteuningsgeometrie van onze nanostrings te optimaliseren, laten we zien

dat de voorgestelde methodologie niet alleen in staat is om één enkel optimalisatiedoel te verwerken, maar ook meerdere conflicterende doelstellingen, zoals de gelijktijdige verbetering van de Q-factor en de Duffing-constante. Bovendien genereren we Pareto-frontiers die de afwegingen tussen meerdere optimalisatiedoelstellingen visualiseren, verifiëren we de geoptimaliseerde resultaten met brute-force-simulaties en valideren we het numerieke raamwerk met experimenten.

Naast de dynamica in een enkele eigenmodus, observeren we modale interacties tussen meerdere vibratiemodi van onze nanostrings in het sterk niet-lineaire regime. In Hoofdstuk 6 tonen we aan dat soft-clamping technieken, die vaak worden gebruikt om resonatoren met een hoge Q-factor te realiseren, ook kunnen worden ingezet om moduskoppeling te ontwerpen. We verifiëren het analytisch afgeleide tweevrijheidsgradensysteem tussen de twee laagste out-of-plane modi met behulp van op FE-gebaseerde ROM's en experimenten. Verder onthullen we de significante invloed van multi-modale interacties op de frequentierespons van de nanostrings, waarmee we extra mogelijkheden aantonen om de niet-lineaire dynamica van mechanische resonatoren te veranderen met behulp van soft clamping. Bovendien benadrukken we het potentieel voor ontwerpen van soft-clamping steunpunten door de geometrische optimalisatie van tweemodale koppeling, waarbij we aantonen dat de effectieve Duffing-constante van de aangedreven modus met 70% kan worden verhoogd, en dat het beginpunt van moduskoppeling geometrisch geprogrammeerd kan worden om het voorkomen juist te bevorderen of te onderdrukken.

We sluiten alle gepresenteerde werken af voor het bereiken van de optimalisatie van niet-lineaire dynamica in nanomechanische resonatoren, en geven een vooruitzicht voor toekomstige richtingen in Hoofstuk 7.

1

1

Introduction

In this chapter, I provide an overview of the evolution of micro/nanoelectromechanical systems (M/NEMS) and the development in mechanical engineering of nonlinear dynamics. I also give the motivation for investigating and optimizing the nonlinear dynamics of nanomechanical resonators in this thesis.

1

WITH the advent of microscale fabrication techniques, humanity has entered the era of microsystems engineering. Microfabricated devices have enabled a plethora of applications, ranging from clocks and sensors to frequency filters [1]. This has been achieved by coupling mechanical motion to various physical quantities, such as electrical signals, optical waves, thermal fluctuations, and magnetic fields. In our daily life, sensors are used as inertial and gyroscopic navigation electronic devices in cellphones and computers [2–5]. As fabrication techniques have progressed, the size of microelectromechanical systems (MEMS) has been further miniaturized, leading to the emergence of nanoelectromechanical systems (NEMS). The limit of detection resolution was further pushed accordingly, to applications such as gas and biochemical sensing [6], atomic force microscopy [7], and even single molecule detection [8]. NEMS are also critical components for future computer technologies [9, 10], and they hold promise for future quantum information applications due to their ability to couple with quantum systems [11–13]. More potential has been identified as the size of these devices is reduced to the atomic scale, like resonators made from 2D materials [14, 15]. These atomic-scale resonators can achieve a resonance frequency tuning range of more than 20 times [16], a capability not readily attainable with mechanical resonators machined from microfabricated materials. Together with the strong electro and optomechanical coupling, NEMS made from 2D materials are prime candidates for the next generation of wearable devices [17]. Most MEMS and NEMS are designed to operate in the linear dynamic range by using simple geometries [18, 19] due to the limited knowledge in utilizing nonlinear behaviours and fabrication techniques. However, we foresee that the frontiers of applications and fundamental research can be greatly expanded if the nonlinear properties of MEMS and NEMS can be fully exploited, which can be accomplished by means of accurate modeling and optimization.

1.1. MECHANICS OF MICRO AND NANOSYSTEMS

Miniaturizing resonators down to the nanoscale has led to the realization of ultrasensitive mechanical systems that exhibit high frequencies and Q-factors, while also making the effects of various damping and nonlinearity sources more pronounced compared to their macroscale counterparts. Particularly, the increased Q-factor enhances sensitivity when the resonators are used as sensors, but it also makes them more prone to nonlinear effects under minute excitations [19]. Researchers have developed various techniques to take advantage of the unique opportunities offered by these small-scale systems, while mitigating their disadvantages [18, 20]. Both passive strategies during fabrication and active control in operation are being explored to design resonators by nonlinear behaviours with a high Q-factor [19]. In addition to tuning mass and linear stiffness, tailoring Q-factor and nonlinearity requires more advanced design techniques, which, in turn, offer greater possibilities for pushing the limits of MEMS/NEMS. In the next two section, I detail out the sources of dissipation and nonlinearity in these tiny mechanical systems.

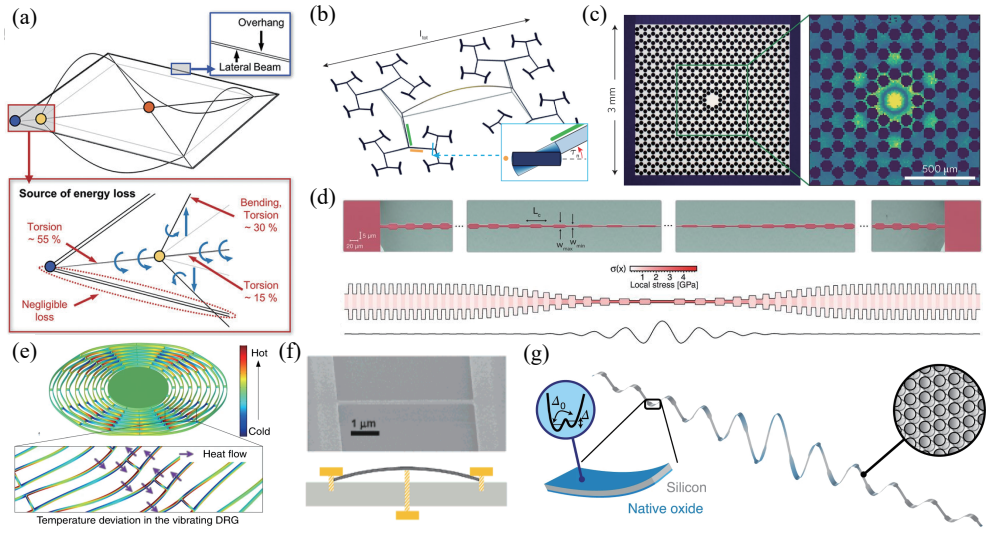

Figure 1.1: **Different techniques for improving mechanical Q-factor in high-stress nanomechanical silicon-based resonators.** (a,b) Soft-clamping [21, 22]; (c,d) Phononic crystals [23, 24]; (e) Decreasing operating frequency [25]; (f) Increasing tensile stress [26]; (g) Crystalline materials [27].

1.1.1. Q-FACTOR

The mechanical Q-factor evaluates the capability to retain the vibrational energy in a specific eigenmode of the resonator. A higher Q-factor means that coherent energy remains in the eigenmode for a longer period before dissipating into the environment. The Q-factor is defined as the ratio between the energy stored in the resonator W to the energy dissipated during one oscillation cycle ΔW [1, 28, 29]

$$Q = 2\pi \frac{W}{\Delta W}. \tag{1.1}$$

As shown in Fig. 1.1, the Q-factor can be tuned from two aspects: the stored energy W and the dissipated energy ΔW. On one hand, the stored energy W can be increased by increasing the stress in the resonator [30], a process known as dissipation dilution [26, 31, 32]. Various materials with high initial tension or high yield strength, such as Si_3N_4, SiC and 2D materials have been investigated for this purpose [33]. On the other hand, there are several sources of dissipated energy ΔW. For instance, sealing the resonator in a vacuum can minimize damping from the environment. Soft-clamping techniques can be used to reduce the curvature of the mode shape, as the inter-layer dislocation contributes to friction loss [21, 22, 34, 35]. Accordingly, materials with low intrinsic damping coefficients, such as crystalline materials, are favored over amorphous ones for resonators requiring a high Q-factor [27]. Additionally, phononic crystals can be designed to shield against radiation loss, preventing the leakage of vibrational energy from the resonator to the substrate [23, 24, 36]. Apart from designing the stored and dissipated energy in the fabrication stage, several mechanisms have been demonstrated for enhancing or suppressing Q-factor of MEMS/NEMS during operation by managing the

energy of the targeted eigenmodes [20]. Methods like external feedback control, optical pumping, and mechanical pumping are known to actively modify Q-factor [37–41].

1.1.2. NONLINEARITY

Nonlinear dynamical phenomena are ubiquitous in nature and human society, ranging from the well-known butterfly effect in chaotic global weather systems [42] to the synchronization in groups of individuals [43]. Nonlinearity refers to the behaviors that deviate from the superposition principle or exhibit coexisting steady states [18]. For instance, the slipping of a block under a linearly increasing force or the output saturation of a piezoelectric actuator under a linearly increasing drive level. MEMS/NEMS are particularly prone to nonlinearities arising both from their intrinsic properties and from interactions with their surrounding environment [19]. These effects become especially prominent at smaller scales, where factors such as air, magnetic fields, or even optical readouts become significant and generate back-actions on the vibrating structures. In contrast to the external nonlinear effects, even a slight shake of the chip will excite the nanomechanical resonators fabricated on it into the nonlinear regime, exhibiting geometric nonlinearity caused by the additional stiffness under large-amplitude vibrations. Nonlinearity in MEMS/NEMS is often modeled using the Duffing equation, which can lead to characteristic backbone curves representing the locus of peak amplitudes in frequency response curves around certain eigenmode [44–46].

Over the past few decades, a wealth of nonlinear phenomena were showcased in MEMS/NEMS, including bi-stability [52–55], self-oscillations [56–58], mode coupling [48, 50, 59], and stochastic resonance [49, 60–62]. Many of these nonlinear phenomena in MEMS/NEMS can be utilized to provide additional information and design space absent in the linear regime of operation, as shown in Fig. 1.2. For instance, nonlinear resonances could be used to characterize material properties [14, 63], stabilize vibration amplitude [48], and generate mechanical frequency combs [51, 64]. By leveraging the interplay between geometric and electrostatic nonlinearities, frequency stability of MEMS/NEMS can be significantly enhanced at large signal-to-noise ratios (SNRs). This is attributed to the intentionally created non-monotonic backbones that the amplitude is independent of the drive frequency at the turning point [47, 65], as shown in Fig. 1.2a. However, introducing external competing nonlinear forces can give rise to a series of unwanted side-effects and noise [66, 67], which further complicate the nonlinear dynamic behaviours and increase the complexity of fabrication as well as operation. Therefore, methodologies that can tailor the dynamic characteristics of nanomechanical devices solely through geometric design in the fabrication stage are highly desirable.

1.2. ENGINEERING NONLINEAR DYNAMICS

Being aware of the ubiquitous presence of nonlinear phenomena, engineers across various research fields—including mechanical, electrical, and optical—have studied these effects for decades and found ways to harness them. Exploiting nonlinearity in dynamical systems offers significant potential for improving device performance, ranging from vibration suppression in aeronautical and civil structures [68–70], to broadband energy harvesting devices [71]. However, it still remains challenging to convince MEMS/NEMS

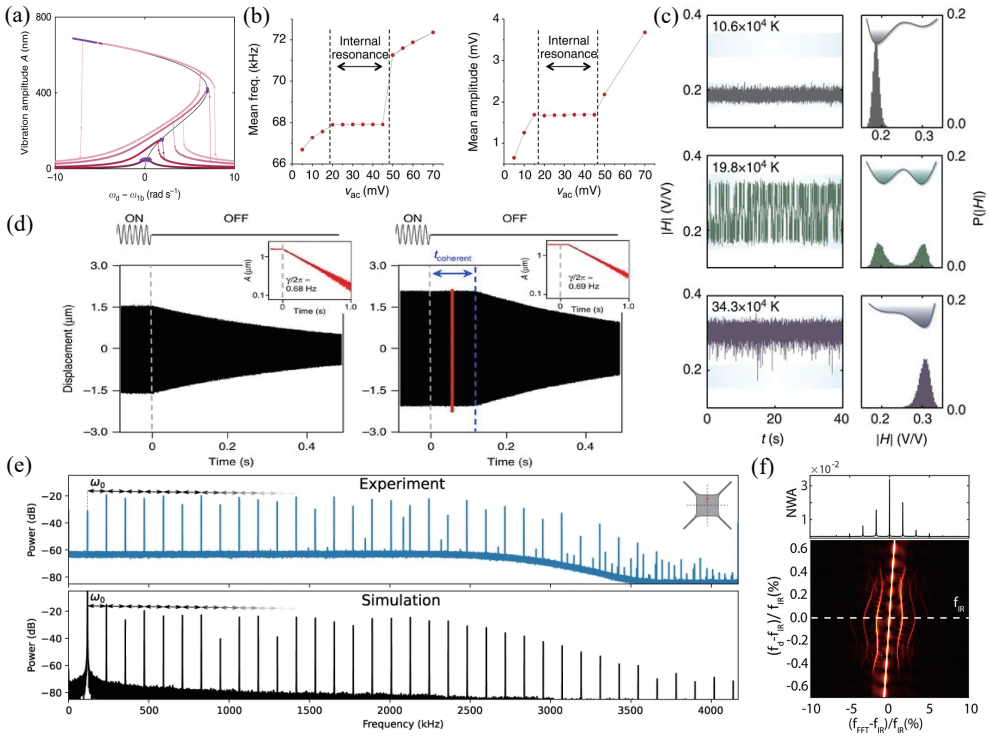

Figure 1.2: **Different nonlinear phenomena in MEMS/NEMS.** (a) Zero-dispersion [47]. (b) Frequency/Amplitude stabilization [48]. (c) Stochastic switching [49]. (d) Coherent energy transfer [50]. (e)(f) Frequency combs [51].

engineers to design systems based on nonlinear behaviors. For many decades, the goal has been to avoid nonlinearity due to the lack of control diagrams for their operational conditions. The difficulty arises from several aspects [19], such as the lack of optimization techniques targeting the nonlinear responses, the challenge of accurately determining the onset of nonlinearity, the operating schematics of bifurcation-based resonators, and the lack of quantitative investigation of mode coupling in strong nonlinear regime. Nevertheless, if these difficulties could be overcome, nonlinearity could then be harnessed by design considering the operational conditions and configurations of MEMS/NEMS, and thus revolutionize the design paradigm for the MEMS/NEMS community. This paradigm shift requires revisiting computational modeling techniques for nonlinear dynamical systems, improving their performance and linking them to design optimization methodologies, which are flourishing in all research areas with the advent of computational technologies [72, 73]. In the next two sections, I introduce the key techniques for modeling nonlinear systems and optimization used in this thesis.

1.2.1. REDUCED ORDER MODELING

In order to efficiently engineer a dynamical system, we should first build an accurate model for it. The full model typically involves a large number of degrees of freedom (DOFs), so it is more efficient to project the full model in physical coordinates into a reduced-order model (ROM) in modal coordinates. This significantly reduces the DOFs required for nonlinear computation while maintaining the fidelity of the full model close to the selected eigenfrequencies. Through reduced-order modeling, we can express terms explicitly and quantitatively, thereby facilitating the process of engineering. It is trivial to build a ROM for a linear dynamic system, where eigenmodes are decoupled. However, as nonlinearities come into play, the superposition principle fails and the eigenvalues of the dynamical system become state-dependent. An even greater challenge arises when different eigenmodes start to couple with each other in the dynamical system.

In the realm of numerical analysis in solid mechanics, the Finite Element (FE) method is currently the most commonly used technique, which is capable of discretizing physical fields into a large number of DOFs. However, implementing nonlinear analysis on a full FE model is computationally intensive. As a result, reduced-order modeling is indispensable when nonlinear dynamic simulations are of interest [73], which are scenarios more common in MEMS/NEMS. Many techniques have been proposed to build ROMs, including Proper Orthogonal Decomposition (POD) [74], Nonlinear Normal Modes (NNM) [75, 76] and Spectral Submanifolds (SSM) [77]. With an FE-based ROM, one can distinctly elucidate the relevant physical properties, enabling thorough study and efficient optimization. It is worth mentioning that, with most FE codes commercialized nowadays, a non-intrusive ROM approach is preferred, which deals only with basic outputs of FE analysis, such as stress field, eigenvalues and eigenmodes [78].

1.2.2. OPTIMIZATION

A reliable optimization procedure is crucial for engineering problems where conducting experiments with a specific design consumes significant time and money. The choice of an appropriate optimization algorithm depends on the characteristics of the problem. Considering the optimization of dynamic performance in MEMS/NEMS, gradient-based shape optimization has been employed to maximize and minimize the Duffing constant of a doubly clamped beam [79, 80]. Moreover, topology optimization has proven its success in minimizing the linear damping in trampoline nanoresonators [81]. However, on one hand, the complexity of MEMS/NEMS geometry may prohibit accurate predictions of eigenmodes analytically. On the other hand, the nonlinear analysis using FE-based ROM further complicates the sensitivity analysis required for gradient-based optimization algorithms. Thus, non-gradient based optimization methods are particularly well-suited for optimizing these nonlinear dynamical systems, such as Genetic Algorithms (GA) [82] and Particle Swarm Optimization (PSO) [83, 84]. The characteristics of these optimization algorithms make them highly suitable for problems involving large numbers of design variables and can be accelerated through parallel computing. Moreover, evolutionary computing and swarm intelligence are key components of computational intelligence—a branch of artificial intelligence focused on adaptive mechanisms that enable intelligent behaviors in complex environments [85]. The influence of artificial

intelligence theories and methodologies is rapidly growing due to the advancements in computing power and the explosion of available data. This new approach to searching for optimal solutions meet the need for balancing complexity, efficiency, and reliability in engineering problems, as well as for developing fully physics-based models.

1.3. AIM AND OUTLINE OF THE THESIS

Building on the overview of current advancements in MEMS/NEMS and engineering techniques, there is a clear need to exploit nonlinear dynamics in the next-generation miniaturized devices and a promising route to leverage the computer-aided design strategies. In this thesis, We go beyond conventional linearization techniques, and develop accurate nonlinear reduced-order models to build the link between geometric parameters and linear as well as nonlinear behaviours of mechanical resonators. Chapter 3 to Chapter 6 are based on four published or submitted journal articles. The structure of the thesis is shown in Fig. 1.3.

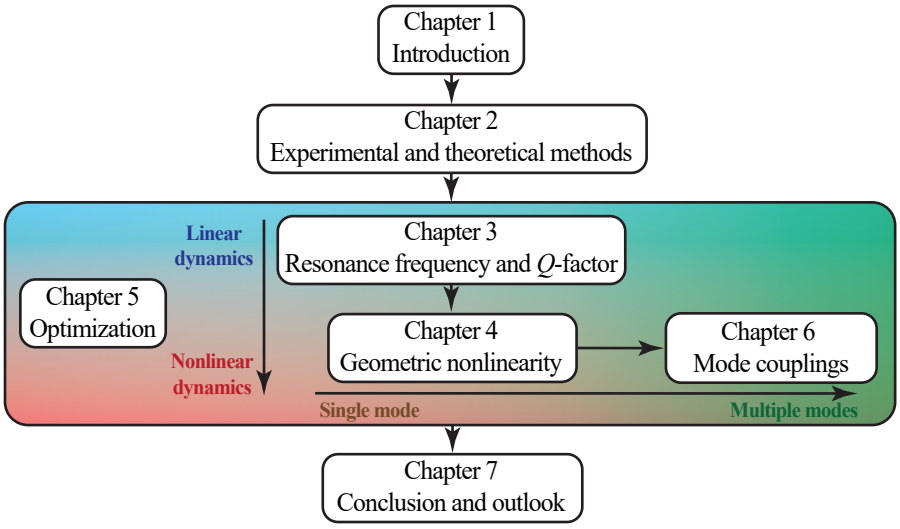

Figure 1.3: **Structure of this thesis.**

In Chapter 2, we first introduce the fabrication and the non-intrusive characterization of Si_3N_4 nanomechanical string resonators that are model systems used in this thesis. In this chapter, we also go through different modeling techniques of nonlinear dynamics in string resonators with compliant supports using the Lagrangian method. In Chapter 3, we explore the mechanical Q-factor limits of nanostrings that are suspended by soft-clamping supports. We discover that there is a trade-off between the requirement of maintaining high stress in the string, and maintaining low stiffness in the supports. By optimization of this trade-off, we obtain a 50% enhancement of Q-factor as compared to the doubly-clamped Si_3N_4 string resonators. Transitioning from linear to nonlinear dynamics in Chapter 4, we show that the geometric nonlinearity can also be substantially tuned by support design. Our approach also allows control over the sign of the Duffing

constant resulting in nonlinear softening of the mechanical mode that conventionally exhibits hardening behavior. With the capability of accurately modeling both linear and nonlinear dynamic properties, in Chapter 5 we integrate a finite element-based nonlinear reduced-order modeling technique with a gradient-free optimization algorithm to design nonlinear mechanical resonators. The resulting methodology is used to optimize the support in the presence of conflicting objectives such as simultaneous enhancement of Q-factor and the Duffing constant. Based on the thorough study of nonlinear dynamics of a single eigenmode, in Chapter 6 we demonstrate that soft-clamping techniques, commonly utilized to achieve high-Q, can also be employed to engineer mode coupling. We discuss that soft-clamping supports allow for tuning the onset of mode coupling and thus can control its occurrence in string resonators. By considering more coupled modes, we reveal the significant impact of multi-mode interactions on the dynamic response, providing additional opportunities to customize the nonlinear dynamics of mechanical resonators. Furthermore, we show the geometric design potential of the soft-clamping supports, whereby the spring hardening nonlinearity of the driven mode can be enhanced by 70% by two-mode coupling. Finally, we give a general conclusion in Chapter 7 and provide an outlook for future directions.

BIBLIOGRAPHY

[1] L. Sementilli, E. Romero, and W. P. Bowen, "Nanomechanical dissipation and strain engineering", Advanced Functional Materials **32**, 2105247 (2022).

[2] A. G. Krause, M. Winger, T. D. Blasius, Q. Lin, and O. Painter, "A high-resolution microchip optomechanical accelerometer", Nature Photonics **6**, 768–772 (2012).

[3] D. K. Shaeffer, "Mems inertial sensors: a tutorial overview", IEEE Communications Magazine **51**, 100–109 (2013).

[4] F. Ayazi and K. Najafi, "A harpss polysilicon vibrating ring gyroscope", Journal of Microelectromechanical Systems **10**, 169–179 (2001).

[5] P. Dabove, G. Ghinamo, and A. M. Lingua, "Inertial sensors for smartphones navigation", SpringerPlus **4**, 1–18 (2015).

[6] K. Eom, H. S. Park, D. S. Yoon, and T. Kwon, "Nanomechanical resonators and their applications in biological/chemical detection: nanomechanics principles", Physics Reports **503**, 115–163 (2011).

[7] G. Binnig, C. F. Quate, and C. Gerber, "Atomic force microscope", Physical Review Letters **56**, 930 (1986).

[8] A. K. Naik, M. Hanay, W. Hiebert, X. Feng, and M. L. Roukes, "Towards single-molecule nanomechanical mass spectrometry", Nature Nanotechnology **4**, 445–450 (2009).

[9] H. Liu, Y. Qin, H.-Y. Chen, J. Wu, J. Ma, Z. Du, N. Wang, J. Zou, S. Lin, X. Zhang, et al., "Artificial neuronal devices based on emerging materials: neuronal dynamics and applications", Advanced Materials **35**, 2205047 (2023).

[10] Z. Qi, L. Mi, H. Qian, W. Zheng, Y. Guo, and Y. Chai, "Physical reservoir computing based on nanoscale materials and devices", Advanced Functional Materials **33**, 2306149 (2023).

[11] M. Aspelmeyer, T. J. Kippenberg, and F. Marquardt, "Cavity optomechanics", Reviews of Modern Physics **86**, 1391–1452 (2014).

[12] S. Barzanjeh, A. Xuereb, S. Gröblacher, M. Paternostro, C. A. Regal, and E. M. Weig, "Optomechanics for quantum technologies", Nature Physics **18**, 15–24 (2022).

[13] A. Alfieri, S. B. Anantharaman, H. Zhang, and D. Jariwala, "Nanomaterials for quantum information science and engineering", Advanced Materials **35**, 2109621 (2023).

[14] P. G. Steeneken, R. J. Dolleman, D. Davidovikj, F. Alijani, and H. S. van der Zant, "Dynamics of 2d material membranes", 2D Materials **8**, 042001 (2021).

[15] P. F. Ferrari, S. Kim, and A. M. van der Zande, "Nanoelectromechanical systems from two-dimensional materials", Applied Physics Reviews **10** (2023).

[16] Z. Ning, T. Shi, M. Fu, Y. Guo, X. Wei, S. Gao, and Q. Chen, "Transversally and axially tunable carbon nanotube resonators in situ fabricated and studied inside a scanning electron microscope", Nano Letters **14**, 1221–1227 (2014).

[17] R. Yin, D. Wang, S. Zhao, Z. Lou, and G. Shen, "Wearable sensors-enabled human–machine interaction systems: from design to application", Advanced Functional Materials **31**, 2008936 (2021).

[18] S. Tiwari and R. N. Candler, "Using flexural mems to study and exploit nonlinearities: a review", Journal of Micromechanics and Microengineering **29**, 083002 (2019).

[19] N. Ghaemi, A. Nikoobin, and M. R. Ashory, "A comprehensive categorization of micro/nanomechanical resonators and their practical applications from an engineering perspective: a review", Advanced Electronic Materials **8**, 2200229 (2022).

[20] J. M. L. Miller, A. Ansari, D. B. Heinz, Y. Chen, I. B. Flader, D. D. Shin, L. G. Villanueva, and T. W. Kenny, "Effective quality factor tuning mechanisms in micromechanical resonators", Applied Physics Reviews **5** (2018).

[21] D. Shin, A. Cupertino, M. H. de Jong, P. G. Steeneken, M. A. Bessa, and R. A. Norte, "Spiderweb nanomechanical resonators via bayesian optimization: inspired by nature and guided by machine learning", Advanced Materials **34**, 2106248 (2022).

[22] S. A. Fedorov, A. Beccari, N. J. Engelsen, and T. J. Kippenberg, "Fractal-like mechanical resonators with a soft-clamped fundamental mode", Physical Review Letters **124**, 025502 (2020).

[23] Y. Tsaturyan, A. Barg, E. S. Polzik, and A. Schliesser, "Ultracoherent nanomechanical resonators via soft clamping and dissipation dilution", Nature Nanotechnology **12**, 776–783 (2017).

[24] A. H. Ghadimi, S. A. Fedorov, N. J. Engelsen, M. J. Bereyhi, R. Schilling, D. J. Wilson, and T. J. Kippenberg, "Elastic strain engineering for ultralow mechanical dissipation", Science **360**, 764–768 (2018).

[25] Q. Li, D. Xiao, X. Zhou, Y. Xu, M. Zhuo, Z. Hou, K. He, Y. Zhang, and X. Wu, "0.04 degree-per-hour mems disk resonator gyroscope with high-quality factor (510 k) and long decaying time constant (74.9 s)", Microsystems & Nanoengineering **4**, 32 (2018).

[26] S. S. Verbridge, J. M. Parpia, R. B. Reichenbach, L. M. Bellan, and H. G. Craighead, "High quality factor resonance at room temperature with nanostrings under high tensile stress", Journal of Applied Physics **99** (2006).

[27] A. Beccari, D. A. Visani, S. A. Fedorov, M. J. Bereyhi, V. Boureau, N. J. Engelsen, and T. J. Kippenberg, "Strained crystalline nanomechanical resonators with quality factors above 10 billion", Nature Physics **18**, 436–441 (2022).

[28] S. Schmid, K. Jensen, K. Nielsen, and A. Boisen, "Damping mechanisms in high-q micro and nanomechanical string resonators", Physical Review B—Condensed Matter and Materials Physics **84**, 165307 (2011).

[29] S. Schmid, L. G. Villanueva, and M. L. Roukes, *Fundamentals of nanomechanical resonators*, Vol. 49 (Springer, 2016).

[30] S. S. Verbridge, D. F. Shapiro, H. G. Craighead, and J. M. Parpia, "Macroscopic tuning of nanomechanics: substrate bending for reversible control of frequency and quality factor of nanostring resonators", Nano Letters **7**, 1728–1735 (2007).

[31] S. Schmid and C. Hierold, "Damping mechanisms of single-clamped and prestressed double-clamped resonant polymer microbeams", Journal of Applied Physics **104** (2008).

[32] B. Zwickl, W. Shanks, A. Jayich, C. Yang, A. Bleszynski Jayich, J. Thompson, and J. Harris, "High quality mechanical and optical properties of commercial silicon nitride membranes", Applied Physics Letters **92** (2008).

[33] M. Xu, D. Shin, P. M. Sberna, R. van der Kolk, A. Cupertino, M. A. Bessa, and R. A. Norte, "High-strength amorphous silicon carbide for nanomechanics", Advanced Materials **36**, 2306513 (2024).

[34] Q. P. Unterreithmeier, T. Faust, and J. P. Kotthaus, "Damping of nanomechanical resonators", Physical Review Letters **105**, 027205 (2010).

[35] Z. Li, M. Xu, R. A. Norte, A. M. Aragón, F. van Keulen, F. Alijani, and P. G. Steeneken, "Tuning the Q-factor of nanomechanical string resonators by torsion support design", Applied Physics Letters **122**, 013501 (2023).

[36] A. H. Ghadimi, D. J. Wilson, and T. J. Kippenberg, "Radiation and internal loss engineering of high-stress silicon nitride nanobeams", Nano Letters **17**, 3501–3505 (2017).

[37] J. Mertz, O. Marti, and J. Mlynek, "Regulation of a microcantilever response by force feedback", Applied Physics Letters **62**, 2344–2346 (1993).

[38] C. H. Metzger and K. Karrai, "Cavity cooling of a microlever", Nature **432**, 1002–1005 (2004).

[39] W. J. Venstra, H. J. Westra, and H. S. van der Zant, "Q-factor control of a microcantilever by mechanical sideband excitation", Applied Physics Letters **99** (2011).

[40] P. Steeneken, K. Le Phan, M. Goossens, G. Koops, G. Brom, C. van der Avoort, and J. van Beek, "Piezoresistive heat engine and refrigerator", Nature Physics **7**, 354–359 (2011).

[41] D. Rugar and P. Grütter, "Mechanical parametric amplification and thermomechanical noise squeezing", Physical Review Letters **67**, 699 (1991).

[42] E. Lorenz, "The butterfly effect", World Scientific Series on Nonlinear Science Series A **39**, 91–94 (2000).

[43] S. H. Strogatz, *Sync: how order emerges from chaos in the universe, nature, and daily life* (Hachette UK, 2012).

[44] M. Amabili, *Nonlinear vibrations and stability of shells and plates* (Cambridge University Press, 2008).

[45] A. H. Nayfeh and D. T. Mook, *Nonlinear oscillations* (John Wiley & Sons, 2008).

[46] O. Shoshani and S. W. Shaw, "Resonant modal interactions in micro/nano-mechanical structures", Nonlinear Dynamics **104**, 1801–1828 (2021).

[47] L. Huang, S. Soskin, I. Khovanov, R. Mannella, K. Ninios, and H. B. Chan, "Frequency stabilization and noise-induced spectral narrowing in resonators with zero dispersion", Nature Communications **10**, 3930 (2019).

[48] D. Antonio, D. H. Zanette, and D. López, "Frequency stabilization in nonlinear micromechanical oscillators", Nature Communications **3**, 1–6 (2012).

[49] W. J. Venstra, H. J. Westra, and H. S. van Der Zant, "Stochastic switching of cantilever motion", Nature Communications **4**, 2624 (2013).

[50] C. Chen, D. H. Zanette, D. A. Czaplewski, S. Shaw, and D. López, "Direct observation of coherent energy transfer in nonlinear micromechanical oscillators", Nature Communications **8**, 1–7 (2017).

[51] A. Keskekler, H. Arjmandi-Tash, P. G. Steeneken, and F. Alijani, "Symmetry-breaking-induced frequency combs in graphene resonators", Nano Letters **22**, 6048–6054 (2022).

[52] S. O. Erbil, U. Hatipoglu, C. Yanik, M. Ghavami, A. B. Ari, M. Yuksel, and M. S. Hanay, "Full electrostatic control of nanomechanical buckling", Physical Review Letters **124**, 046101 (2020).

[53] M. Yuksel, E. Orhan, C. Yanik, A. B. Ari, A. Demir, and M. S. Hanay, "Nonlinear nanomechanical mass spectrometry at the single-nanoparticle level", Nano Letters **19**, 3583–3589 (2019).

[54] H. Okamoto, I. Mahboob, K. Onomitsu, and H. Yamaguchi, "Rapid switching in high-Q mechanical resonators", Applied Physics Letters **105**, 083114 (2014).

[55] F. Bayram, D. Gajula, D. Khan, and G. Koley, "Mechanical memory operations in piezotransistive GaN microcantilevers using au nanoparticle-enhanced photoacoustic excitation", Microsystems & Nanoengineering **8**, 1–14 (2022).

[56] L. Villanueva, E. Kenig, R. Karabalin, M. Matheny, R. Lifshitz, M. Cross, and M. Roukes, "Surpassing fundamental limits of oscillators using nonlinear resonators", Physical Review Letters **110**, 177208 (2013).

[57] C. Chen, D. H. Zanette, J. R. Guest, D. A. Czaplewski, and D. López, "Self-sustained micromechanical oscillator with linear feedback", Physical Review Letters **117**, 017203 (2016).

[58] J. M. Miller, A. Gomez-Franco, D. D. Shin, H.-K. Kwon, and T. W. Kenny, "Amplitude stabilization of micromechanical oscillators using engineered nonlinearity", Physical Review Research **3**, 033268 (2021).

[59] J. Güttinger, A. Noury, P. Weber, A. M. Eriksson, C. Lagoin, J. Moser, C. Eichler, A. Wallraff, A. Isacsson, and A. Bachtold, "Energy-dependent path of dissipation in nanomechanical resonators", Nature Nanotechnology **12**, 631–636 (2017).

[60] R. L. Badzey and P. Mohanty, "Coherent signal amplification in bistable nanomechanical oscillators by stochastic resonance", Nature **437**, 995–998 (2005).

[61] H. Mofatteh, B. Shahryari, A. Mirabolghasemi, A. Seyedkanani, R. Shirzadkhani, G. Desharnais, and A. Akbarzadeh, "Programming multistable metamaterials to discover latent functionalities", Advanced Science **9**, 2202883 (2022).

[62] P. Belardinelli, W. Yang, A. Bachtold, M. Dykman, and F. Alijani, "Hidden mechanical oscillatory state in a carbon nanotube revealed by noise", arXiv preprint arXiv:2312.14034 (2023).

[63] D. Davidovikj, F. Alijani, S. J. Cartamil-Bueno, H. S. van der Zant, M. Amabili, and P. G. Steeneken, "Nonlinear dynamic characterization of two-dimensional materials", Nature Communications **8**, 1253 (2017).

[64] D. A. Czaplewski, C. Chen, D. Lopez, O. Shoshani, A. M. Eriksson, S. Strachan, and S. W. Shaw, "Bifurcation generated mechanical frequency comb", Physical Review Letters **121**, 244302 (2018).

[65] C. Samanta, N. Arora, and A. Naik, "Tuning of geometric nonlinearity in ultrathin nanoelectromechanical systems", Applied Physics Letters **113**, 113101 (2018).

[66] M. Sansa, E. Sage, E. C. Bullard, M. Gély, T. Alava, E. Colinet, A. K. Naik, L. G. Villanueva, L. Duraffourg, M. L. Roukes, et al., "Frequency fluctuations in silicon nanoresonators", Nature Nanotechnology **11**, 552–558 (2016).

[67] L. G. Villanueva, R. B. Karabalin, M. H. Matheny, E. Kenig, M. C. Cross, and M. L. Roukes, "A nanoscale parametric feedback oscillator", Nano Letters **11**, 5054–5059 (2011).

[68] J. Yuan, C. Gastaldi, E. D. Goy, and B. Chouvion, "Friction damping for turbomachinery: a comprehensive review of modelling, design strategies, and testing capabilities", Progress in Aerospace Sciences **147**, 101018 (2024).

[69] C. Firrone and S. Zucca, "Passive control of vibration of thin-walled gears: advanced modelling of ring dampers", Nonlinear Dynamics **76**, 263–280 (2014).

[70] A. F. Vakakis, O. V. Gendelman, L. A. Bergman, D. M. McFarland, G. Kerschen, and Y. S. Lee, *Nonlinear targeted energy transfer in mechanical and structural systems*, Vol. 156 (Springer Science & Business Media, 2008).

[71] A. F. Vakakis, O. V. Gendelman, L. A. Bergman, A. Mojahed, and M. Gzal, "Nonlinear targeted energy transfer: state of the art and new perspectives", Nonlinear Dynamics **108**, 711–741 (2022).

[72] G. Rega, "Nonlinear dynamics in mechanics and engineering: 40 years of developments and ali h. nayfeh's legacy", Nonlinear Dynamics **99**, 11–34 (2020).

[73] C. Touzé, A. Vizzaccaro, and O. Thomas, "Model order reduction methods for geometrically nonlinear structures: a review of nonlinear techniques", Nonlinear Dynamics **105**, 1141–1190 (2021).

[74] G. Berkooz, P. Holmes, and J. L. Lumley, "The proper orthogonal decomposition in the analysis of turbulent flows", Annual Review of Fluid Mechanics **25**, 539–575 (1993).

[75] R. M. Rosenberg, "The normal modes of nonlinear n-degree-of-freedom systems", Journal of Applied Mechanics **29**, 7–14 (1962).

[76] G. Kerschen, M. Peeters, J.-C. Golinval, and A. F. Vakakis, "Nonlinear normal modes, part i: a useful framework for the structural dynamicist", Mechanical Systems and Signal Processing **23**, 170–194 (2009).

[77] G. Haller and S. Ponsioen, "Nonlinear normal modes and spectral submanifolds: existence, uniqueness and use in model reduction", Nonlinear Dynamics **86**, 1493–1534 (2016).

[78] A. A. Muravyov and S. A. Rizzi, "Determination of nonlinear stiffness with application to random vibration of geometrically nonlinear structures", Computers & Structures **81**, 1513–1523 (2003).

[79] S. Dou, B. S. Strachan, S. W. Shaw, and J. S. Jensen, "Structural optimization for nonlinear dynamic response", Philosophical Transactions of the Royal Society A: Mathematical, Physical and Engineering Sciences **373**, 20140408 (2015).

[80] L. L. Li, P. M. Polunin, S. Dou, O. Shoshani, B. Scott Strachan, J. S. Jensen, S. W. Shaw, and K. L. Turner, "Tailoring the nonlinear response of mems resonators using shape optimization", Applied Physics Letters **110**, 081902 (2017).

[81] D. Høj, F. Wang, W. Gao, U. B. Hoff, O. Sigmund, and U. L. Andersen, "Ultra-coherent nanomechanical resonators based on inverse design", Nature Communications **12**, 5766 (2021).

[82] J. H. Holland, *Adaptation in natural and artificial systems: an introductory analysis with applications to biology, control, and artificial intelligence* (MIT press, 1992).

[83] R. C. Eberhart, Y. Shi, and J. Kennedy, *Swarm intelligence* (Elsevier, 2001).

[84] C. A. C. Coello, G. T. Pulido, and M. S. Lechuga, "Handling multiple objectives with particle swarm optimization", IEEE Transactions on Evolutionary Computation **8**, 256–279 (2004).

[85] G. Quaranta, W. Lacarbonara, and S. F. Masri, "A review on computational intelligence for identification of nonlinear dynamical systems", Nonlinear Dynamics **99**, 1709–1761 (2020).

2

2

METHODOLOGY

In this chapter, we introduce the experimental and theoretical methodologies referred to and developed in this thesis. The experimental part contains the introduction of fabrication techniques for nanomechanical Si_3N_4 devices and the characterization of linear and nonlinear dynamics with the laser Doppler interferometry. The theoretical part contains the derivation of the governing equations of nonlinear dynamics in string resonators, and the finite element-based reduced-order modeling technique.

2.1. EXPERIMENTS

Silicon-based materials are commonly used in MEMS/NEMS. Due to the mature fabrication technique and the high yield, we select Si_3N_4 resonators as our testing platform for studying nonlinear dynamics at the nanoscale. Additionally, the built-in high stress in Si_3N_4 grown by low pressure chemical vapor deposition (LPCVD) also helps to significantly enhance the mechanical Q-factor, which makes the hidden nonlinearity more prominent under the same vibration amplitude.

2.1.1. FABRICATION

As demonstrated in Fig. 2.1, the string resonators in this work are fabricated from a high-stress Si_3N_4 layer with an in-plane isotropic pre-stress around $\sigma_0 = 1.1$ GPa and Poisson's ratio $\nu = 0.23$ grown by LPCVD on a silicon substrate [1]. The devices are suspended by a fluorine-based (SF_6) deep reactive ion underetching step. After the release etching, the predefined Si_3N_4 pattern is suspended, and the isotropic stress field will redistribute in order to satisfy the force equilibrium of new boundary conditions.

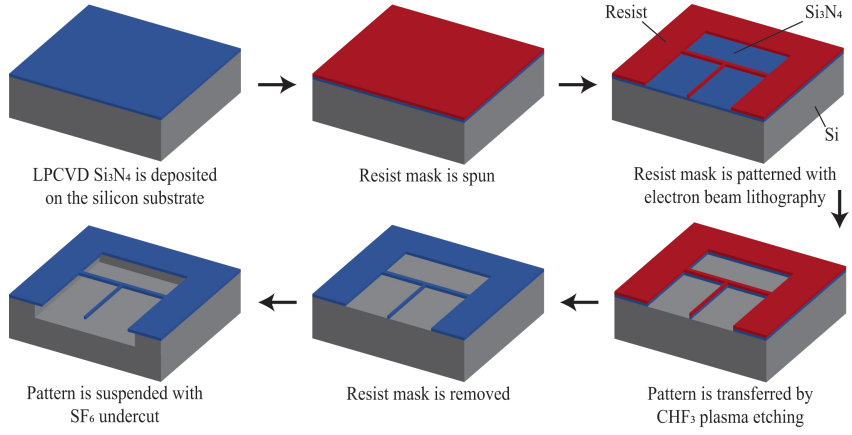

Figure 2.1: **Fabrication process of suspended Si_3N_4 nanomechanical resonators.**

2.1.2. MEASUREMENT

To measure the dynamics of the fabricated nanomechanical devices, as shown in Fig. 2.2, we attach the chip with doubly sided tape to a piezo actuator that drives the resonator by an out-of-plane harmonic base actuation. We use a Zurich Instruments HF2LI lock-in amplifier, connected to an MSA400 Polytec laser Doppler vibrometer, to measure the out-of-plane motion of the string resonator. We perform all measurements in a vacuum chamber with a pressure below 2×10^{-6} mbar at room temperature.

CHARACTERIZING MATERIAL PROPERTIES OF SI_3N_4

Since the pre-stress in a Si_3N_4 cantilever disappears completely after the release etching, the Q-factor of these devices becomes equal to the intrinsic value Q_0 determined from the material parameters. With the known length L, thickness h, and density ρ we can use

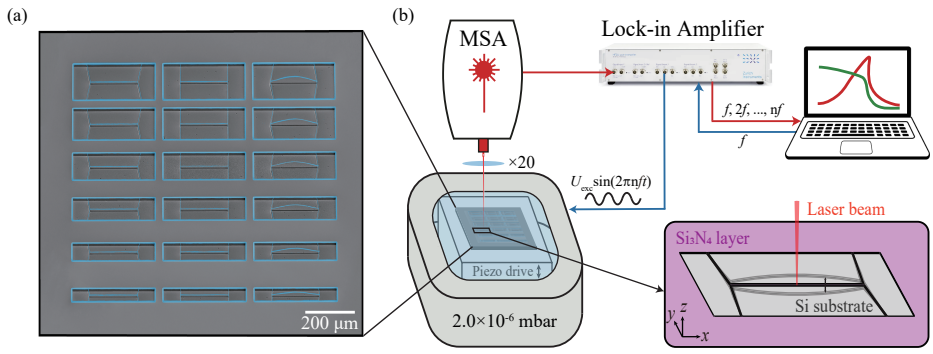

Figure 2.2: **Measurement set-up of Si_3N_4 nanomechanical resonators.**

the resonance frequency and Q of the fundamental mode of a cantilever to characterize the Young's modulus E and loss modulus E'. As all of our samples have a non-negligible undercut of 5 µm due to the dry etching technique, it is less accurate to directly use the analytical expression for the eigenfrequency of cantilevers to calculate the Young's modulus E. The reason is that the undercut increases the effective length of the cantilever, leading to a reduction in both the resonance frequency and the calculated value of E compared to a cantilever without undercut. To estimate the value of E we use a finite element model in COMSOL, which also takes the undercut into consideration as shown in Fig. 2.3a, and use it to determine the Young's modulus E, by tuning its value in the finite element model such that the simulated fundamental resonance frequency matches the experimental value.

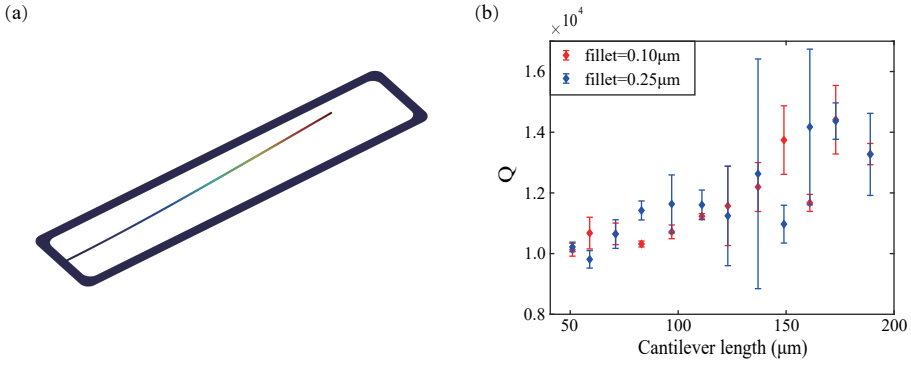

Figure 2.3: (a) Out-of-plane fundamental mode shape of a cantilever with 161 µm length, 1 µm width and 340 nm thickness. (b) Measurements of Q-factor of different cantilever lengths and two fillet values at clamping boundary.

To determine the Q-factor of the cantilevers, we perform ring-down measurement after driving the device at its out-of-plane fundamental resonance frequency. The residual stress in cantilevers fabricated by high-stress Si_3N_4 is negligible, so the Q-factor obtained from the measurement is approximately equivalent to $Q_0 = E/E'$. As shown in

Fig. 2.3(b), we measure cantilevers with different lengths and different fillets at a pressure below 2.0×10^{-6}mbar. The Q-factor of each cantilever is measured three times, and the standard deviation of these measurements is used to determine the error bars in Fig. 2.3(b). The error bars for longer cantilevers are bigger, possibly because they are slightly bent due to gravity, which makes the measurement more difficult. We take the average value $Q_0 = 11774$ of all devices in Fig. 2.3(b) as the intrinsic Q-factor.

To compare the measured intrinsic Q_0 to earlier works, we use the analytical expression [1, 2] that includes the effect of surface losses:

$$\begin{aligned}\frac{1}{Q_0} &= \frac{1}{Q_{\text{Volume}}} + \frac{1}{Q_{\text{Surface}}} \\ &= \frac{1}{28000} + \frac{1}{\lambda h}.\end{aligned} \tag{2.1}$$

By setting the measured Q_0 equal to Eq. (2.1), and using that the thickness of our samples is $h = 340$ nm, the surface loss parameter is determined to be $\lambda = 6\times10^{10}(\text{m}^{-1})$. This value of λ and the obtained Q_0 are in close agreement with the values reported in the literature [2].

MEASURING NONLINEAR DYNAMICS OF A SINGLE MODE

After introducing the measurement of linear dynamical properties, here we discuss our fitting strategy to extract the mass-normalized Duffing constant β of the string resonators from frequency sweeps at higher drive levels. In performing our measurements with a Polytec laser Doppler vibrometer, we use the velocity decoder with a calibration factor of 200 mm/s/V. We note that the resonance frequency f_0 of a nanomechanical resonator with high stress is sensitive to temperature variations. Both the measurement laser and the environment can induce thermal variations, which may cause the resonance frequency of our resonators to shift by a few tens of hertz during consecutive frequency sweep measurements under different drive levels. This in turn can make the estimation of the Duffing constant very difficult, since we need to fit for the backbone (see the red curve in Fig. 2.4b) to obtain β:

$$f_{\text{max}}^2 = f_0^2 + \frac{3}{16\pi^2}\beta A_{\text{max}}^2, \tag{2.2}$$

where A_{max} is the maximum amplitude of each frequency response curve and f_{max} is the frequency corresponding to A_{max}. In order to correct for this, we first fit the off-resonance response of multiple frequency response curves at different drive levels to estimate the resonance frequency f_0 using the damped harmonic oscillator model:

$$A_{\text{d}} = \frac{\dfrac{A_{\text{max}}}{Q}}{\sqrt{\left[1-\left(\dfrac{f}{f_0}\right)^2\right]^2 + \left(\dfrac{1}{Q}\dfrac{f}{f_0}\right)^2}}, \tag{2.3}$$

where A_{d} is the measured amplitude of the device at its center and f is the drive frequency, as shown in Fig. 2.4a. To be able to estimate β from the backbone, we then fix the response curve of the lowest drive level and horizontally adjust all the other curves

at higher drive levels, according to the differences between their linearly fitted f_0 and the one of the lowest drive level (see blue arrows in Fig. 2.4a). This would allow us to extract the Duffing constant with good accuracy from multiple frequency response curves at different drive levels, as shown in Fig. 2.4b.

It is worth mentioning that we can also obtain the resonance frequency f_0 and Q-factor for our devices using this off-resonance fitting technique, as demonstrated in Eq. (2.3). However, for the resonators with extremely high Q-factors [3, 4], the resolution bandwidth of the measurement set-up might be larger than the bandwidth (FWHM) of the measured eigenmode. So it is necessary to perform ring-down measurements at the resonance peak to characterize the Q-factors.

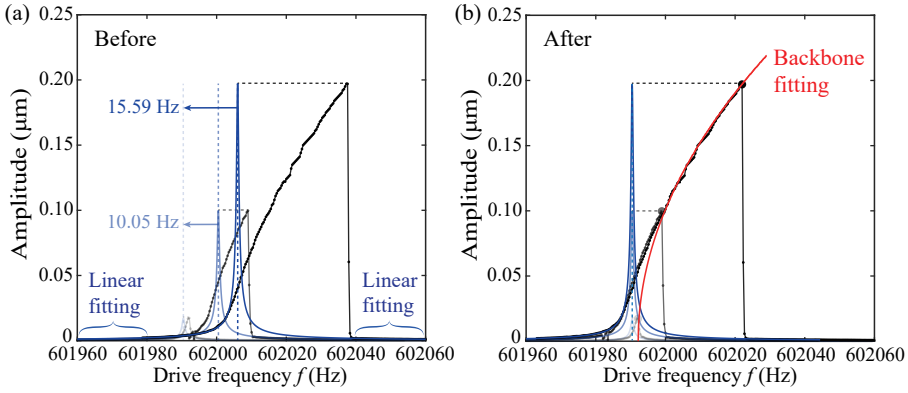

Figure 2.4: **Fitting the backbone of multiple frequency response curves.** We choose three frequency sweeps (black lines with dots) from the string resonator before (a) and after (b) implementing the fitting technique. The red curve shows the backbone fitted by multiple frequency sweeps after aligning the resonance frequencies of the different curves. The blue curves show the linear fits using the off-resonance response of the nonlinear resonance curves at different drive levels.

Additionally, we find that the backbone curve overlaps with the response curves at large amplitudes, as shown in Fig. 2.4b. Consequently, we can fit a single frequency response curve to obtain β to improve the efficiency when characterizing arrays of devices. Notably, selecting an appropriate fitting range is essential. On the one hand, if the amplitude is not large enough, the backbone does not yet overlap with the response curve, which would lead to an underestimation of β. On the other hand, if the devices are driven too hard, the resonator would enter the strong nonlinear regime. In the latter case, the nonlinear damping would kick-in and lead to an overestimation of β. In general, one should use the part of the response curve right before the nonlinear damping initiates for this fitting technique to work. We have validated by experiments that the fitted values of f_0 and β match well with the ones fitted through multiple frequency sweeps.

2.2. MODELING OF NONLINEAR DYNAMICS

With known material and geometric parameters, we can effectively optimize the desired dynamic properties of resonators using precise modeling techniques. We choose vibrating strings as our model to test our design strategies due to the simplicity of their dy-

namics. Initially, we apply the Lagrangian method to investigate the nonlinear dynamics of string resonators with a pair of compliant supports. We simplify these supports as in-plane springs to explore their impact on the central string's stress and clamping conditions. However, in structures with high stress, even minor variations in geometries or boundary conditions may lead to a huge change in their dynamical properties. Consequently, in order to capture all these details to the greatest extent and guide the design effectively, we also build finite element (FE)-based reduced-order models for our fabricated nanoresonators.

2.2.1. STRESS TUNING THROUGH THE COMPLIANT SUPPORTS

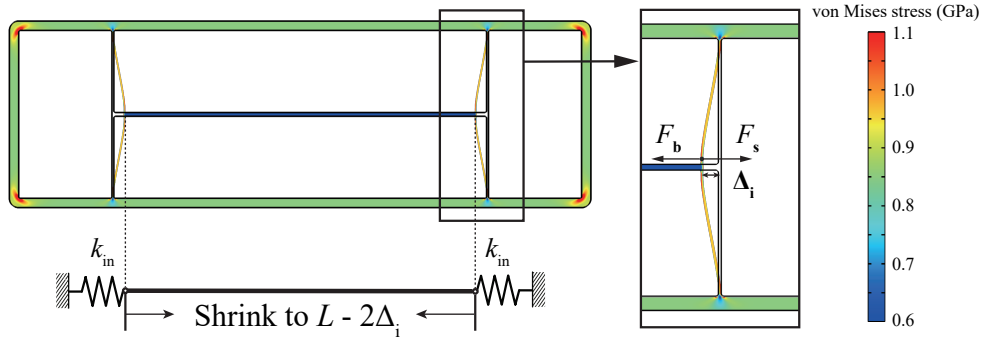

Figure 2.5: **The stress redistribution in fabricated high-stress Si_3N_4 devices.** The schematic simplifies the two support beams as two linear springs k_{in}. The zoom-in inset shows the force equilibrium between supports and the central string.

As demonstrated in Fig. 2.5, the supports of an H-shaped nanomechanical Si_3N_4 resonator can be treated as a pair of in-plane springs, that affect the stress along the central string after the release etching as described in Fig. 2.1. In order to quantify this stress tuning effect, we derive the analytical expression of the in-plane stiffness k_{in} by simplifying the compliant supports as stressed doubly clamped beams. To relate the simplified spring model in Fig. 2.5 to the actual geometry of the device, we build an in-plane force equilibrium between the supports and the central string: $F_b = F_s$. The in-plane force of the central string F_b and the force of the support structure F_s are given by:

$$\begin{aligned} F_s &= k_{in}\Delta_i, \\ F_b &= \sigma_b A, \end{aligned} \tag{2.4}$$

where Δ_i is the in-plane deflection of the support beam and $A = hw$ is the area of the central string's cross section. The initial stress in the Si_3N_4 layer is isotropic: $\sigma_{x,0} = \sigma_{y,0} = \sigma_0$, and the initial strain along the length of the beam (x-direction) obeys $\epsilon_{x,0} = (\sigma_{x,0} - \nu\sigma_{y,0})/E$ from linear elasticity theory. During release of the string, the stress along the y-direction relaxes and becomes zero while the strain in the x-direction does not change, such that one gets $\epsilon_{x,0} = \sigma_{b0}/E$ and the stress along the central string reduces to $\sigma_{b0} = \sigma_0(1-\nu)$. Now the stress reduces further due to the deflection of the supports to a value σ_b, with $\sigma_{b0} - \sigma_b = 2\Delta_i E/L$. By using that $\Delta_i = \sigma_b A/k_{in}$ from Eq. (2.4), we obtain:

$$\sigma_b = (1-\nu)\sigma_0 \left(1 + \frac{2EA}{k_{in}L}\right)^{-1}. \tag{2.5}$$

Now we derive an analytical equation for the in-plane stiffness k_{in} that we can combine with Eq. (2.5) to determine the stress along the central string after release σ_b. A challenge in deriving such an analytical expression is that, depending on the support width and length, the in-plane bending stiffness k_{Ei}, shear stiffness k_{si}, and stiffness due to stress in the support beams $k_{\sigma i}$ can all be relevant, thus no simple analytical model in literature is available that captures all three factors simultaneously. We therefore introduce an approximate three-spring model (see Eq. (2.6)), which consists of the series combination of k_{Ei} and k_{si} in parallel to $k_{\sigma i}$. The series combination of k_{Ei} and k_{si} ensures that the weakest of the shear and bending rigidity dominates their combined effect, whereas the parallel combination with $k_{\sigma i}$ results in an approximated additive contribution from the stress-induced stiffness. We will later show (left in Fig. 3.7), that this approximate analytical model for k_{in}, yields comparable results for the estimated string stress σ_b to those obtained via finite element simulations. The equation for k_{in} in this three-spring model is

$$k_{in} = \left(\frac{1}{k_{Ei}} + \frac{1}{k_{si}}\right)^{-1} + k_{\sigma i}. \tag{2.6}$$

We now determine the individual equations for the three springs in the model. The in-plane bending stiffness of the support beams k_{Ei}, which is derived from the central deformation of a doubly clamped Euler-Bernoulli beam under a central force, is

$$k_{Ei} = \frac{192EI_{si}}{L_s^3}. \tag{2.7}$$

Here $I_{si} = hw_s^3/12$ is the in-plane moment of inertia of the support beam, and w_s is the support width. The in-plane shear stiffness k_{si} of the support beams is significant because the ratio w_s/h is large. To determine its value, the support beams are treated as Timoshenko beams with in-plane stiffness k_{si} given by [5]

$$k_{si} = \frac{4A_sG}{\eta L_s}. \tag{2.8}$$

Here, G is the shear modulus, with $G = E/(2(1+\nu))$ for an isotropic material and $A_s = w_s h$ is the cross-section of the support beam. $\eta = 1.2$ is a factor determined by the rectangular cross section of the support beams [5]. The equation for the in-plane stiffness $k_{\sigma_b i}$ caused by the stress in the support beams is

$$k_{\sigma i} = \frac{4A_s\sigma_s}{L_s}, \tag{2.9}$$

where σ_s is the stress along the length direction of support beams and approximately equals the initial stress σ_0 of Si_3N_4.

2.2.2. LAGRANGE EQUATIONS

NONLINEAR EQUATION OF A SINGLE MODE

After determining the stress redistribution in the string induced by the supports, here we obtain the equations of motion for a high-stress string resonator with finite in-plane stiffness k_{in} at its two ends, as shown in Fig. 2.6. The motion is assumed as the fundamental mode shape $q_1(t)\sin(\pi/Lx)$ of a doubly clamped string, where $q_1(t)$ is the displacement as a function of time. Since our goal is to investigate the influence of in-plane to out-of-plane coupling on geometric nonlinearity, we model the support via in-plane springs k_{in}, and neglect the torsional and out-of-plane (z direction) stiffness of the support for simplicity [6], i.e.,

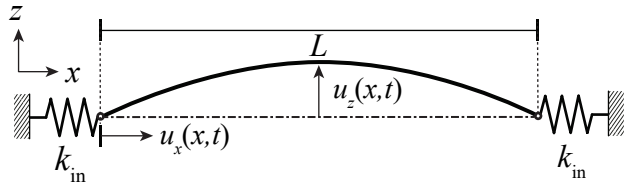

Figure 2.6: **Simplified model for a string resonator with compliant supports.** The influence from supports on the geometric nonlinearity is equivalent to a pair of in-plane translational springs, which relaxes the in-plane stiffening when the string vibrates at large amplitudes.

$$u_z(x,t) = q_1(t)\sin\left(\frac{\pi}{L}x\right), \tag{2.10a}$$

$$u_x(x,t) = u_0\left(\frac{2x}{L}-1\right) + \sum_{i=1}^{N} u_i(t)\sin\left(\frac{2i\pi x}{L}\right) + u_{\text{a}}(t)\left(1-\frac{2x}{L}\right), \tag{2.10b}$$

where u_x and u_z are the displacements of the string in x (in-plane) and z (out-of-plane) directions, respectively. $u_i(t)$ represents the in-plane counterpart of a stressed doubly hinged string under the out-of-plane motion $u_z(x,t)$. u_0 is a constant that represents the initial stress in the x direction of the string, i.e.,

$$u_0 = \frac{(1-\nu)\sigma_0 L}{2E}, \tag{2.11}$$

$u_{\text{a}}(t)$ in Eq. (2.10b) is the additional in-plane motion that is considered to ensure satisfaction of the boundary conditions of the finite in-plane stiffness k_{in}, which is in constrast to the ones in doubly hinged strings ($k_{\text{in}}\to\infty$, $u_{\text{a}}(t)\to 0$). $u_{\text{a}}(t)$ can be obtained from applying force balance to the point at which the beam is connected to the support:

$$\begin{aligned} k_{\text{in}}u_{\text{a}}(t) &= \frac{EA}{L}\int_0^L \varepsilon \,\mathrm{d}x \\ &= \frac{EA}{L}\int_0^L \left[\frac{\partial u_x}{\partial x} + \frac{1}{2}\left(\frac{\partial u_z}{\partial x}\right)^2\right]\mathrm{d}x, \end{aligned} \tag{2.12}$$

where $A = hw$ is the area of the string's cross section and ε is the strain along the x direction. Then by substituting Eqs. (2.10a) and (2.10b) to Eq. (2.12) we obtain

$$u_{\mathrm{a}}(t) = \frac{\pi^2 q_1^2(t)}{8L}\left(1 + \frac{k_{\mathrm{in}} L}{2EA}\right)^{-1}. \tag{2.13}$$

The strain energy of a string can be written as

$$U_{\mathrm{s}} = \frac{1}{2}\int_0^L EA\varepsilon^2 \mathrm{d}x. \tag{2.14}$$

The energy stored in the two in-plane springs k_{in} is

$$U_{\mathrm{k}} = 2 \times \frac{1}{2} k_{\mathrm{in}} u_{\mathrm{a}}^2(t). \tag{2.15}$$

Furthermore, the kinetic energy of the string, neglecting the in-plane inertia, is given by

$$T = \frac{1}{2}\rho A \int_0^L \left(\frac{\partial u_z}{\partial t}\right)^2 \mathrm{d}x. \tag{2.16}$$

Using Eqs. (2.14) - (2.16), the Lagrange equations can be constructed as

$$\frac{\mathrm{d}}{\mathrm{d}t}\left(\frac{\partial T}{\partial \dot{\boldsymbol{q}}}\right) - \frac{\partial T}{\partial \boldsymbol{q}} + \frac{\partial U}{\partial \boldsymbol{q}} = \frac{\partial W}{\partial \boldsymbol{q}}, \tag{2.17}$$

where $\boldsymbol{q} = [q_1(t), u_1(t), u_2(t), ..., u_i(t)], i = \{3, 4, ..., N\}$, is the vector that includes all the generalized coordinates, and W is the work done by the external forces. Since the in-plane inertia has been neglected, after substituting the potential energy $U = U_{\mathrm{s}} + U_{\mathrm{k}}$ and the kinetic energy T in Eq. (2.16), we have a system of nonlinear equations consisting of two differential equations associated with the generalized coordinates $q_1(t)$ and N algebraic equations in terms of $u_i(t)$. By solving the N algebraic equations we can determine $u_i(t)$ in terms of $q_1(t)$

$$\begin{aligned} u_1(t) &= -\frac{\pi q_1^2(t)}{8L} \\ u_2(t) &= u_3(t) = ... = u_N(t) = 0, \end{aligned} \tag{2.18}$$

which will reduce the $N+1$ nonlinear equations to a single Duffing equation

$$m_{\mathrm{eff},1}\ddot{q}_1 + c_1\dot{q}_1 + k_{1,1}q_1 + k_{3,1}q_1^3 = 0. \tag{2.19}$$

where $k_{1,1}$ is the linear stiffness, c_1 is the damping factor, $k_{3,1}$ is the coefficient of cubic nonlinearity. By dividing Eq. (2.19) by the effective mass $m_{\mathrm{eff},1}$, one can find the mass normalized linear stiffness

$$\omega_1^2 = \frac{k_{1,1}}{m_{\mathrm{eff},1}} = \frac{\pi^2(1-\nu)\sigma_0}{\rho L^2}\left(1 + \frac{2EA}{k_{\mathrm{in}} L}\right)^{-1}, \tag{2.20}$$

where $m_{\mathrm{eff},1} = \rho AL/2$. Accordingly, we can obtain the resonance frequency of the first mode:

$$f_1 = \frac{1}{2L}\sqrt{\frac{1}{\rho}\frac{(1-\nu)\sigma_0}{1+\frac{2EA}{k_{\text{in}}L}}} = \frac{1}{2L}\sqrt{\frac{\sigma_{\text{b}}}{\rho}}, \tag{2.21a}$$

where σ_{b} is the stress of the string in the x direction after the release etch, as shown in Eq. (2.5).

The mass-normalized nonlinear coefficient β_1 is

$$\beta_1 = \frac{k_{3,1}}{m_{\text{eff},1}} = \frac{\pi^4 E}{4\rho L^4}\left(1+\frac{2EA}{k_{\text{in}}L}\right)^{-1}. \tag{2.22a}$$

It is worth noting that $(1+2EA/k_{\text{in}}L)^{-1}$ serves as a tuning factor introduced by the finite in-plane stiffness k_{in}, which rescales σ_{b}, ω_1^2, and β_1 of a doubly-clamped string with pre-tension $(1-\nu)\sigma_0$ in the same rate. The additional finite k_{in} will relax the pre-tension as shown in Eq. (2.5). Consequently, the mass-normalized linear stiffness $k_{1,1}/m_{\text{eff},1} = \omega_1^2 = (2\pi f_0)^2$, which is proportional to the tension, is scaled down by $(1+2EA/k_{\text{in}}L)^{-1}$. In contrast, the finite in-plane springs k_{in} rescale the mass-normalized Duffing constant β_1 in a different way that brings an additional in-plane motion $u_{\text{a}}(t)\,(1-2x/L)$, neutralizing the elongation of the central string under large-amplitude vibrations. Surprisingly, β_1 is scaled down at the same rate, i.e., the tuning factor $(1+2EA/k_{\text{in}}L)^{-1}$ of σ_{b} and ω_1^2, which is demonstrated by the solid line in Fig. 2.7a and b. The dotted lines in Fig. 2.7 show the analytical results of a doubly-clamped string under different σ_{b}, which show an opposite trend against σ_{b} compared to the ones with soft-clamping.

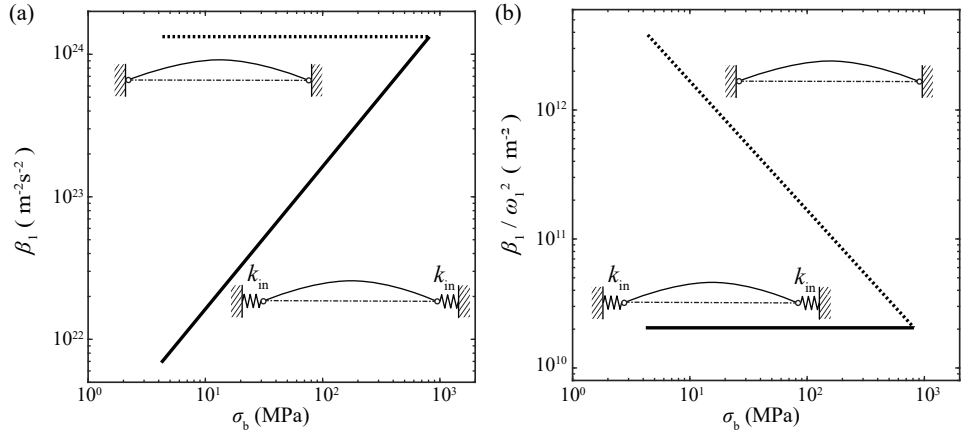

Figure 2.7: **Dependence of linear and nonlinear stiffness on stress σ_{b} tuned by supports' in-plane stiffness k_{in}.** The solid lines represent the strings with finite stiffness k_{in} and the dotted lines are results of doubly-clamped strings.

NONLINEAR EQUATIONS OF MULTIPLE MODES

In the previous subsection, a detailed investigation into compliant supports has demonstrated their ability to tune the nonlinear dynamics of the fundamental mode in a string resonator. Moreover, the mode coupling is particularly intriguing, since it represents the interaction among different resonance modes with high efficiency in a single resonator. Using the Lagrangian method, we also obtain the equations of motion for a string resonator supported with in-plane springs k_{in} under mode coupling between two lowest out-of-plane modes, as shown in Fig. 2.8.

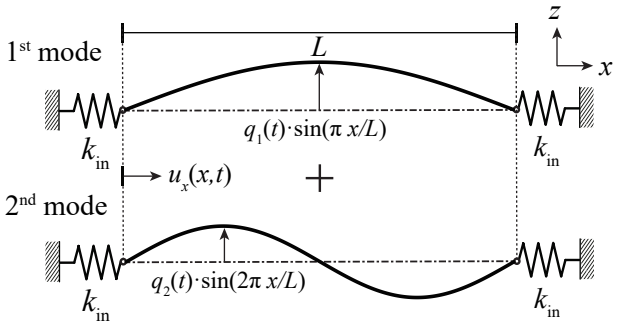

Figure 2.8: **Simplified model for a string resonator with soft-clamping supports.** The influence from soft-clamping supports is equivalent to a pair of in-plane springs k_{in} at both ends of the central string. The mode shapes are approximated as sinusoidal functions, which are the closed form solutions for doubly hinged strings.

With an additional second mode included as compared to Eq. (2.10a), the out-of-plane and the in-plane displacement for a string undergoing two-mode coupling can be written, respectively, as

$$u_z(x,t) = q_1(t)\sin\left(\frac{\pi}{L}x\right) + q_2(t)\sin\left(2\frac{\pi}{L}x\right), \tag{2.23a}$$

$$u_x(x,t) = u_0\left(\frac{2x}{L}-1\right) + \sum_{i=1}^{N} u_i(t)\sin\left(\frac{i\pi x}{L}\right) + u_{\text{a}}(t)\left(1-\frac{2x}{L}\right). \tag{2.23b}$$

Then by substituting Eqs. (2.23a) and (2.23b) to Eq. (2.12) we obtain

$$u_{\text{a}}(t) = \frac{\pi^2\left[q_1^2(t)+4q_2^2(t)\right]}{8L}\left(1+\frac{k_{\text{in}}L}{2EA}\right)^{-1}. \tag{2.24}$$

There is an additional modal coordinate $q_2(t)$ in Eq. (2.17) as compared to the case of a single mode, where $\boldsymbol{q} = [q_1(t), q_2(t), u_1(t), u_2(t), ..., u_i(t)]$, $i = \{3,4,...,N\}$. Consequently, we have a system of nonlinear equations consisting of two differential equations associated with the generalized coordinates $q_1(t)$ and $q_2(t)$, and N algebraic equations in terms of $u_i(t)$. By solving the N algebraic equations we can determine $u_i(t)$ in terms of $q_1(t)$ and $q_2(t)$:

$$
\begin{aligned}
u_1(t) &= -\frac{\pi q_1(t) q_2(t)}{L}, \\
u_2(t) &= -\frac{\pi q_1^2(t)}{8L}, \\
u_3(t) &= -\frac{\pi q_1(t) q_2(t)}{3L}, \\
u_4(t) &= -\frac{\pi q_2^2(t)}{4L}, \\
u_5(t) &= u_6(t) = \ldots = u_N(t) = 0,
\end{aligned}
\tag{2.25}
$$

which will reduce the $N+2$ nonlinear equations to only two coupled equations:

$$m_{\text{eff},1}\ddot{q}_1 + c_1\dot{q}_1 + k_{1,1}q_1 + k_{3,1}q_1^3 + k_{\text{c},1}q_1q_2^2 = 0, \tag{2.26a}$$

$$m_{\text{eff},2}\ddot{q}_2 + c_2\dot{q}_2 + k_{1,2}q_2 + k_{3,2}q_2^3 + k_{\text{c},2}q_1^2q_2 = 0. \tag{2.26b}$$

where $k_{1,1}$ and $k_{1,2}$ are the linear stiffnesses, c_1 and c_2 are the damping factors, $k_{3,1}$ and $k_{3,2}$ are the coefficients of cubic nonlinearity, $k_{c,1}$ and $k_{c,2}$ are the coupling coefficients of these two modes. The mass-normalized linear stiffnesses for both modes are

$$\frac{k_{1,1}}{m_{\text{eff},1}} = \omega_1^2 = \frac{\pi^2(1-\nu)\sigma_0}{\rho L^2}\left(1+\frac{2EA}{k_{\text{in}}L}\right)^{-1}, \tag{2.27a}$$

$$\frac{k_{1,2}}{m_{\text{eff},2}} = \omega_2^2 = \frac{4\pi^2(1-\nu)\sigma_0}{\rho L^2}\left(1+\frac{2EA}{k_{\text{in}}L}\right)^{-1}, \tag{2.27b}$$

where $m_{\text{eff},1} = m_{\text{eff},2} = \rho AL/2$. Accordingly, we can obtain the resonance frequency of the two lowest mode shapes, respectively:

$$f_1 = \frac{1}{2L}\sqrt{\frac{1}{\rho}\frac{(1-\nu)\sigma_0}{1+\frac{2EA}{k_{\text{in}}L}}} = \frac{1}{2L}\sqrt{\frac{\sigma_{\text{b}}}{\rho}}, \tag{2.28a}$$

$$f_2 = \frac{1}{L}\sqrt{\frac{1}{\rho}\frac{(1-\nu)\sigma_0}{1+\frac{2EA}{k_{\text{in}}L}}} = \frac{1}{L}\sqrt{\frac{\sigma_{\text{b}}}{\rho}}, \tag{2.28b}$$

where σ_{b} is the stress of the string in the x direction after the release etching [6], i.e.,

$$\sigma_{\text{b}} = (1-\nu)\sigma_0\left(1+\frac{2EA}{k_{\text{in}}L}\right)^{-1}. \tag{2.29}$$

The mass-normalized nonlinear coefficients β_1, β_2, and γ are

$$\beta_1 = \frac{k_{3,1}}{m_{\text{eff},1}} = \frac{\pi^4 E}{4\rho L^4}\left(1+\frac{2EA}{k_{\text{in}}L}\right)^{-1}, \tag{2.30a}$$

$$\beta_2 = \frac{k_{3,2}}{m_{\text{eff},2}} = \frac{4\pi^4 E}{\rho L^4}\left(1+\frac{2EA}{k_{\text{in}}L}\right)^{-1}, \tag{2.30b}$$

$$\gamma = \frac{k_{\text{c},1}}{m_{\text{eff},1}} = \frac{k_{\text{c},2}}{m_{\text{eff},2}} = \frac{\pi^4 E}{\rho L^4}\left(1+\frac{2EA}{k_{\text{in}}L}\right)^{-1}. \tag{2.30c}$$

Similarly to the case of a single mode, $(1+2EA/k_{\text{in}}L)^{-1}$ serves as a tuning factor for σ_{b}, as well as for the mass-normalized linear stiffness $k_{1,1}/m_{\text{eff},1} = \omega_1^2$, $k_{1,2}/m_{\text{eff},2} = \omega_2^2$, the mass-normalized Duffing constants β_1, β_2, and the mass-normalized coupling strength γ in the same rate.

2.2.3. FINITE ELEMENT-BASED REDUCED ORDER MODELING

In order to carry out the optimization of nanomechanical resonators with arbitrary geometries more accurately, we also develop modeling technique based on FE simulations. However, FE-based simulations face computational problems when nonlinear dynamics is of interest because a large number of equations of motion have to be integrated in small increments in the spectral neighborhood of resonant modes. Therefore, once an FE model is built, the number of degrees of freedom has to be reduced for computational efficiency. In this section, we discuss the methodology we devised for that specific purpose. Fig. 2.9 shows the schematic of the model we use to simulate our fabricated Si_3N_4 devices. The yellow geometry marks the suspended nanomechanical resonators. The surrounding blue lines mark the constraint we implement as fixed boundary conditions.

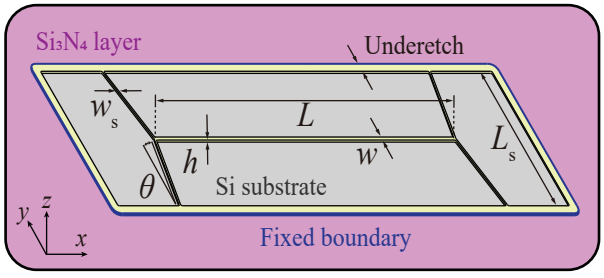

Figure 2.9: **Schematic model of a nanomechanical string resonator with soft-clamping supports.**

In Fig. 2.10, we show the procedure used to build the FE-based ROM. We first perform static analysis of the strained structures to calculate the stress redistribution and corresponding static deformation. For devices with negative support angles θ, we perform an additional buckling analysis to obtain the buckled state. This step of analysis mimics the etching process that the high-stress Si_3N_4 layer releases from the silicon substrate. It is worth noting that the high initial stress of the structure leads to deformation of the device as compared to its unreleased state. In order to calculate nonlinear forces accurately, we first calculate this initial deformed state and only afterwards perform modal

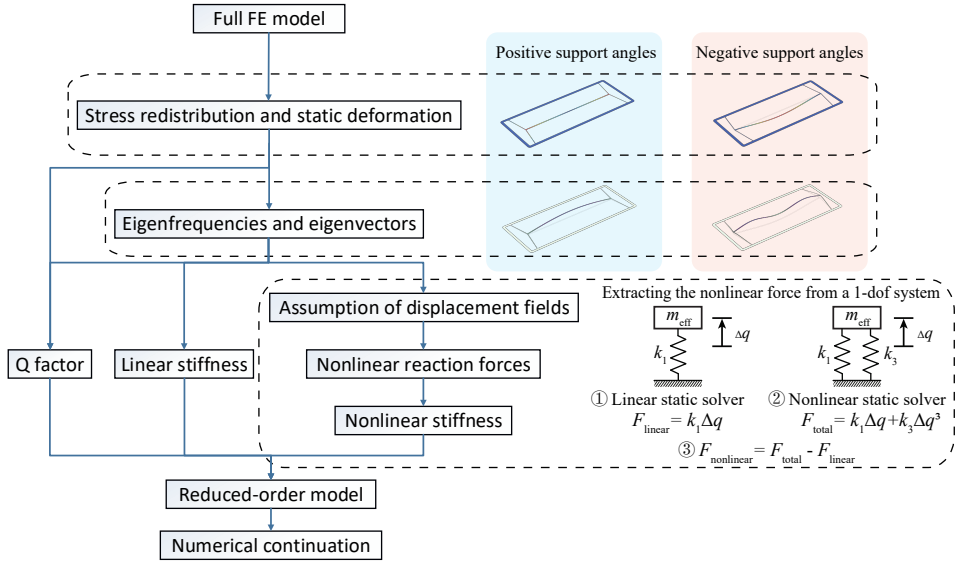

Figure 2.10: **The flowchart of the FE-based ROM procedure.** The static analysis and eigenfrequency analysis of both flat and buckled devices are shown respectively in blue and orange. An example for a one degree-of-freedom (1-dof) system is shown to demonstrate the calculation procedure of the nonlinear reaction force.

analysis. The equations of motions of the full FE model for the deformed configuration are then written as

$$\boldsymbol{M}\ddot{\boldsymbol{X}}(t)+\boldsymbol{C}\dot{\boldsymbol{X}}(t)+\boldsymbol{K}\boldsymbol{X}(t)+\boldsymbol{\Gamma}(\boldsymbol{X}(t))=\boldsymbol{F}(t), \tag{2.31}$$

where $\boldsymbol{M}$, $\boldsymbol{C}$, $\boldsymbol{K}$ are the mass, damping, and linear stiffness matrices (considering the additional stiffness from the redistributed stress field as well), respectively, $\boldsymbol{X}(t)$ is the displacement vector, and $\boldsymbol{F}(t)$ is the force vector. $\boldsymbol{\Gamma}(\boldsymbol{X}(t))$ is the nonlinear force vector due to geometric nonlinearity, which is in this work composed of quadratic and cubic functions of $\boldsymbol{X}(t)$. We use the eigenvectors of Eq. (2.31) to obtain a set of N symmetric out-of-plane modes $\boldsymbol{\Phi}$ as the assumption of displacement fields for the STiffness Evaluation Procedure (STEP) [7–9], which is a reduced order modeling technique we use to capture the geometric nonlinearity. A set of coupled modal equations with reduced degrees of freedom are then obtained by applying the modal coordinate transformation $\boldsymbol{X}(t)=\boldsymbol{\Phi}\boldsymbol{q}(t)$:

$$\widetilde{\boldsymbol{M}}\ddot{\boldsymbol{q}}(t)+\widetilde{\boldsymbol{C}}\dot{\boldsymbol{q}}(t)+\widetilde{\boldsymbol{K}}\boldsymbol{q}(t)+\boldsymbol{\gamma}(\boldsymbol{q}(t))=\widetilde{\boldsymbol{F}}(t), \tag{2.32}$$

where $\widetilde{\boldsymbol{M}}=\boldsymbol{\Phi}^{\top}\boldsymbol{M}\boldsymbol{\Phi}$, $\widetilde{\boldsymbol{C}}=\boldsymbol{\Phi}^{\top}\boldsymbol{C}\boldsymbol{\Phi}$, $\widetilde{\boldsymbol{K}}=\boldsymbol{\Phi}^{\top}\boldsymbol{K}\boldsymbol{\Phi}$, $\boldsymbol{\gamma}(\boldsymbol{q}(t))=\boldsymbol{\Phi}^{\top}\boldsymbol{\Gamma}(\boldsymbol{X}(t))$, $\widetilde{\boldsymbol{F}}=\boldsymbol{\Phi}^{\top}\boldsymbol{F}$. $\boldsymbol{q}(t)$ is the vector of N modal coordinates $\{q_1(t),q_2(t),...,q_N(t)\}$. The nonlinear term $\boldsymbol{\gamma}(\boldsymbol{q}(t))$ can be written as

$$\gamma^{(i)}=\sum_{j=1}^{N}\sum_{k=j}^{N}a_{jk}^{(i)}q_jq_k+\sum_{j=1}^{N}\sum_{k=j}^{N}\sum_{l=k}^{N}b_{jkl}^{(i)}q_jq_kq_l, \tag{2.33}$$

where i represents the ith modal coordinate and j, k, l are mode numbers. Based on the prescribed displacement fields as implemented boundary conditions, we solve for the reaction forces on all nodes with and without considering the geometric nonlinearity in the full FE model, i.e., $\boldsymbol{F}_{\text{total}} = \boldsymbol{F}_{\text{linear}} + \boldsymbol{F}_{\text{nonlinear}}$ and $\boldsymbol{F}_{\text{linear}}$, respectively. Then we can project the obtained reaction force vectors in physical coordinates to the ith modal coordinate, and calculate the nonlinear reaction force $\gamma^{(i)} = F^{(i)}_{\text{nonlinear}} = F^{(i)}_{\text{total}} - F^{(i)}_{\text{linear}}$. Consequently, by applying different combinations of modal coordinates $\{q_1(t), q_2(t), ..., q_N(t)\}$ as the displacement fields, we extract the corresponding modal nonlinear reaction forces. With a set of algebraic equations in the form of Eq. (2.34), we solve for the quadratic coefficient a and the cubic coefficient b for all modal coordinates.

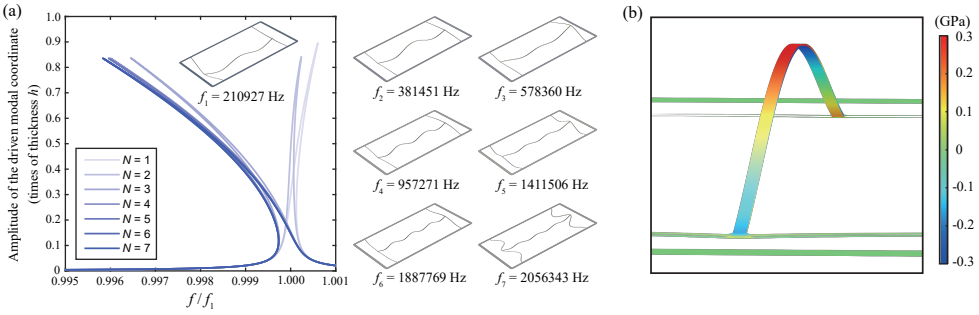

Figure 2.11: (a) Frequency response curves of the first symmetric out-of-plane mode (210927 Hz) of the device with $L = 200\mu$m, $w = 2\mu$m, $w_s = 1\mu$m, $L_s = 150\mu$m, and $\theta = -0.1$rad, which are simulated by numerical continuation (Matcont) with different numbers of symmetric out-of-plane modes included in the mode set. N refers to the number of modes included and modes with lower resonance frequencies are always added with priority. All the modes included in the ROM are listed next to the nonlinear frequency response. (b) The stress field at the top and bottom surface along the length of the string, which is derived after the buckling analysis of the device in (a).

For devices dominated by tensile stress, a single-mode ROM can predicts the experimental results accurately (See Chapter 4 for more details). For buckled devices that have out-of-plane curvatures and more complex stress deformations, as shown in Fig. 2.11b, we use multi-mode ROM to capture the softening nonlinear behavior at large amplitudes. In Fig. 2.11a, we show the convergence analysis performed to capture the softening behavior. This procedure involves the inclusion of higher modes of vibration in the reduced-order model (Eq. (2.32)) until the solution is converged. We note that in-plane modes and asymmetric out-of-plane modes do not have an influential role on the convergence of the obtained nonlinear dynamic responses. We found that a ROM with only the first mode can obtain accurate results for the slightly buckled cases. For other buckled cases, however, we account for the first six symmetric eigenmodes, a number that was determined after a careful convergence analysis.

Meanwhile, according to the static stress field σ_{xx}, σ_{xy}, σ_{yy} and the out-of-plane component of mode shapes ϕ_z obtained in the last section, Q-factors of all modal coordinates can be calculated. The Q-factor of a stressed resonator can be expressed as [6]

$$
\begin{aligned}
Q &= 2\pi \frac{W_{\text{tension}} + W_{\text{bending}} + W_{\text{torsion}}}{\Delta W_{\text{bending}} + \Delta W_{\text{torsion}}} \\
&= \left(\frac{W_{\text{tension}}}{W_{\text{bending}} + W_{\text{torsion}}} + 1 \right) Q_0 \\
&= \left(\frac{\frac{h}{2} \iint \sigma_{xx} \left(\frac{\partial \phi_z}{\partial x} \right)^2 + \sigma_{yy} \left(\frac{\partial \phi_z}{\partial y} \right)^2 + 2\sigma_{xy} \frac{\partial \phi_z}{\partial x} \frac{\partial \phi_z}{\partial y} \mathrm{d}x\mathrm{d}y}{\frac{Eh^3}{24(1-\nu^2)} \iint \left(\frac{\partial^2 \phi_z}{\partial x^2} \right)^2 + \left(\frac{\partial^2 \phi_z}{\partial y^2} \right)^2 + 2\nu \frac{\partial^2 \phi_z}{\partial x^2} \frac{\partial^2 \phi_z}{\partial y^2} + 2(1-\nu) \left(\frac{\partial^2 \phi_z}{\partial x \partial y} \right)^2 \mathrm{d}x\mathrm{d}y} + 1 \right) Q_0,
\end{aligned}
\tag{2.34}
$$

where W_{tension} is the mode shape's stored tension energy, $\Delta W_{\text{bending}}$ and W_{bending} are the bending loss per cycle and the stored bending energy, respectively, $\Delta W_{\text{torsion}}$ and W_{torsion} are the torsional loss per cycle and stored torsion energy, respectively. Q_0 is the intrinsic material quality factor, which can be expressed as $Q_0 = E/E'$. To estimate Q for a supported string resonator in Eq. (2.34), we subdivided the stored energy into tension energy, bending energy, and torsion energy for the string resonator itself and for the supports. When beams bend or undergo torsional deformation, the energy dissipated per cycle is $\Delta W = 2\pi W/Q_0$. In contrast, tension energy, according to the dissipation dilution, does not lead to a linear dissipation contribution. From the mode shapes calculated in the last subsection, we can numerically calculate the stored tension energy, as well as the stored bending and torsion energy in different eigenmodes of the resonator. Finally, with the Q-factor, and with linear and nonlinear stiffnesses obtained from FE simulations, we can compute Eq. (2.32) and calculate the response of the ROM under different drives by numerical continuation (Matcont [10]).

2.3. CONCLUSION

In this chapter, we first introduced our experimental approaches, including the fabrication procedure of Si_3N_4 nanoresonators and the measurement setup. Using a laser Doppler vibrometer, we characterized the linear and nonlinear dynamic properties of the devices by measuring their dynamic responses. In order to establish the relationship between the observed dynamics and the resonators' geometries, we employed a vibrating string with compliant supports to model our fabricated devices. By the Lagrangian method, we examined the influence of these supports on the dynamics of strings with built-in stress. Additionally, FE-based ROMs were developed to provide more accurate predictions of the dynamics in resonators with arbitrary geometries. These experimental, theoretical, and numerical techniques collectively established the foundation for the works presented in following chapters.

BIBLIOGRAPHY

[1] D. Shin, A. Cupertino, M. H. de Jong, P. G. Steeneken, M. A. Bessa, and R. A. Norte, "Spiderweb nanomechanical resonators via bayesian optimization: inspired by nature and guided by machine learning", Advanced Materials **34**, 2106248 (2022).

[2] L. G. Villanueva and S. Schmid, "Evidence of surface loss as ubiquitous limiting damping mechanism in SiN micro-and nanomechanical resonators", Physical Review Letters **113**, 227201 (2014).

[3] A. Cupertino, D. Shin, L. Guo, P. G. Steeneken, M. A. Bessa, and R. A. Norte, "Centimeter-scale nanomechanical resonators with low dissipation", Nature Communications **15**, 4255 (2024).

[4] N. J. Engelsen, A. Beccari, and T. J. Kippenberg, "Ultrahigh-quality-factor micro-and nanomechanical resonators using dissipation dilution", Nature Nanotechnology, 1–13 (2024).

[5] W. C. Young, R. G. Budynas, A. M. Sadegh, et al., *Roark's formulas for stress and strain* (McGraw-hill New York, 1989).

[6] Z. Li, M. Xu, R. A. Norte, A. M. Aragón, F. van Keulen, F. Alijani, and P. G. Steeneken, "Tuning the Q-factor of nanomechanical string resonators by torsion support design", Applied Physics Letters **122**, 013501 (2023).

[7] A. A. Muravyov and S. A. Rizzi, "Determination of nonlinear stiffness with application to random vibration of geometrically nonlinear structures", Computers & Structures **81**, 1513–1523 (2003).

[8] Z. Li, M. Xu, R. A. Norte, A. M. Aragón, P. G. Steeneken, and F. Alijani, "Strain engineering of nonlinear nanoresonators from hardening to softening", Communications Physics **7**, 53 (2024).

[9] A. Keşkekler, V. Bos, A. M. Aragón, P. G. Steeneken, and F. Alijani, "Multimode nonlinear dynamics of graphene resonators", Physical Review Applied **20**, 064020 (2023).

[10] A. Dhooge, W. Govaerts, Y. A. Kuznetsov, H. G. E. Meijer, and B. Sautois, "New features of the software matcont for bifurcation analysis of dynamical systems", Mathematical and Computer Modelling of Dynamical Systems **14**, 147–175 (2008).

3

3

TUNING THE Q-FACTOR OF NANOMECHANICAL STRING RESONATORS BY TORSION SUPPORT DESIGN

In recent years, the Q-factor of Si_3N_4 nanomechanical resonators has been significantly increased by soft-clamping techniques using large and complex support structures. To date, however, obtaining similar performance with smaller supports has remained a challenge. Here, we make use of torsion beam supports to tune the Q-factor of Si_3N_4 string resonators. By design optimization of the supports, we obtain a 50% Q-factor enhancement compared to the standard clamped-clamped string resonators. By performing experimental and numerical studies we show that further improvement of the Q-factor is limited by a trade-off between maximizing stress and minimizing the torsional support stiffness. Thus, our study also provides insights into the dissipation limits of high-stress string resonators and outlines how advanced designs can be realized for reaching ultimate $f_0 \times Q$ product, while maintaining a small footprint.

This chapter has been published in *Applied Physics Letters* **122**, 013501 (2023) by Zichao Li, Minxing Xu, Richard A. Norte, Alejandro M. Aragón, Fred van Keulen, Farbod Alijani, Peter G. Steeneken.

3.1. INTRODUCTION

Nanomechanical resonators are receiving growing interest owing to their high force sensitivity and ultra-low dissipation. They have demonstrated strong potential for mass sensing [1, 2], force sensing [3–6], and transducer applications [7–9]. Moreover, nanomechanical systems are promising platforms to explore fundamental physics in both the classical [10] and quantum [11–14] regimes. During the last decades there has been a tremendous drive towards increasing the mechanical Q-factor of nanomechanical resonators, to maximally benefit from the important performance advantages this offers [15–17]: when dissipation is low, resonant sensors, clocks, and frequency synthesizers can be operated at large oscillation amplitudes with low power. Moreover, low losses diminish the thermomechanical-noise induced motion of the resonator via the fluctuation-dissipation theorem [15, 18]. This low noise results in higher signal-to-noise ratio, and improves the limit of detection in sensor applications. Finally, in the quantum regime, a high-Q isolates the resonant mode from being affected by thermomechanical noise, and thus protects quantum states from decoherence [19, 20].

A main methodology for increasing Q in Si_3N_4 resonators has been the increase of tension [21–24]. This dissipation-dilution mechanism has resulted in large Q enhancements, especially in materials like Si_3N_4 that can be grown with high intrinsic tensile stress [25, 26]. However, the increase of stress in a clamped-clamped string is associated with an increase of the bending curvature near the clamping points, which in turn limits the dissipation-dilution factor [27, 28]. Recent efforts have enabled mitigating these losses by soft-clamping techniques, which involve large support structures that allow high-stress to be preserved while maintaining small curvatures near the edge of the resonant mode [17, 29, 30].

In this chapter, we investigate an alternative approach for reducing dissipation in Si_3N_4 string resonators by suspending the string using torsion beam supports instead of the more conventional direct clamping at the edges [31, 32]. To determine the Q-factor limits of this approach, we study experimentally, analytically, and numerically — by means of the Finite Element Method (FEM) — how the support dimensions can be used to optimize the resonance frequency and Q-factor in string resonators. We show that the supports enable stress engineering over a wide range from 0.10 GPa to 0.80 GPa, while also controlling the torsional and out-of-plane translational stiffness of supports. We also demonstrate a Q enhancement of 50% which is limited due to a support design trade-off between maximizing the string's stress and minimizing supports' torsional stiffness.

3.2. Q-FACTOR OF A STRING RESONATOR WITH NON-IDEAL SUPPORTS

To get an intuitive understanding of this trade-off, before discussing detailed analytical and numerical models, we first analyze a simplified analytical model of the Q-factor of string resonators with non-ideal supports. Theoretically, an ideal string resonator would be free to rotate around its pinned endpoints. In practice however, as we show in Fig. 3.1, the supports always have a finite torsional stiffness k_t and out-of-plane translational stiffness k that will cause the support point to move and rotate along with the resonant

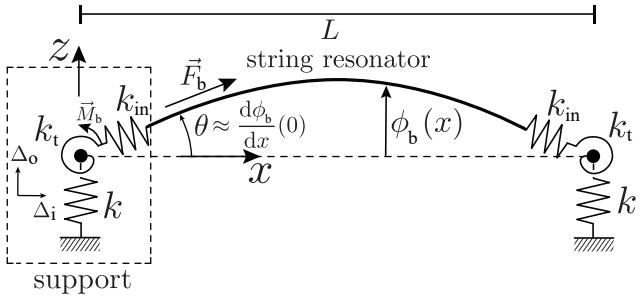

Figure 3.1: **Schematic model for a string resonator with non-ideal supports.** At the clamping points the string exerts a tension $\vec{F}_b$ and a torque $\vec{M}_b$ on the support, which are balanced by the in-plane translational spring k_{in}, the out-of-plane translational spring k and the torsional spring k_t of the support structure.

motion of the string. Although this support motion has little effect on the resonance frequency and mode shape of the string, it can have a significant influence on the dissipation in nanomechanical string resonators [10, 33, 34]. To estimate the effect of supports on the mechanical Q, we consider the string resonator with a known tension F_b and assume that the tension is high enough to neglect effects of the support on the mode shape, such that the fundamental resonant mode can be assumed as $\phi_b(x) = \phi_0 \sin(\pi x/L)$, where x denotes spatial coordinate, ϕ_0 is the amplitude of the mode shape and L is the resonator's length. As a consequence of its motion, the string will exert a force and torque on the support with energy storage $W_k = \frac{1}{2}k\Delta_o^2$ and $W_t = \frac{1}{2}k_t\theta^2$, for small angles $\theta \approx \frac{d\phi_b(x)}{dx}\big|_{x=0}$, associated with the supports' out-of-plane deflection Δ_o and torsional rotation θ respectively. We also note that the force balance in the out-of-plane z-direction is given by $F_{b,z} = F_b \frac{d\phi_b(x)}{dx}\big|_{x=0} = k\Delta_o$, where $F_b = A_b\sigma_b$ and A_b is the cross-sectional area of the string. Using the given mode shape, the strain energy stored in the fundamental mode of the string can be written as $W_\sigma = \pi^2 F_b \phi_0^2/(4L)$.

After having established these equations, we obtain Q of a string resonator [33] with translational and torsional supports:

$$Q = \left(\frac{W_\sigma}{2W_k + 2W_t} + 1\right) Q_0 \approx \frac{Q_0 L}{4}\left(\frac{F_b}{k} + \frac{k_t}{F_b}\right)^{-1}, \tag{3.1}$$

where Q_0 is the intrinsic quality factor due to material damping. The equation shows that, as long as $F_b/k \ll k_t/F_b$, an increase in tension F_b can enlarge the Q-factor of the string resonator via dissipation dilution. The increase in Q continues until around $F_b/k \approx k_t/F_b$, and at $F_{b,max} = \sqrt{k_t k}$ the Q-factor will show a maximum value $Q_{max} = \frac{Q_0 L}{8}\sqrt{k/k_t}$.

This approximate equation tells us that optimization of support structures requires to maximize their out-of-plane translational stiffness k, while minimizing their torsional stiffness k_t, in order to minimize losses due to bending and torsional motion. Furthermore, a third important requirement is that in-plane stiffness k_{in} of the support (see Fig. 3.1 and Section 2.2.1 in Chapter 2) and the material's initial isotropic pre-stress σ_0 are high enough to prevent the string tension F_b from dropping far below $F_{b,max}$ after the

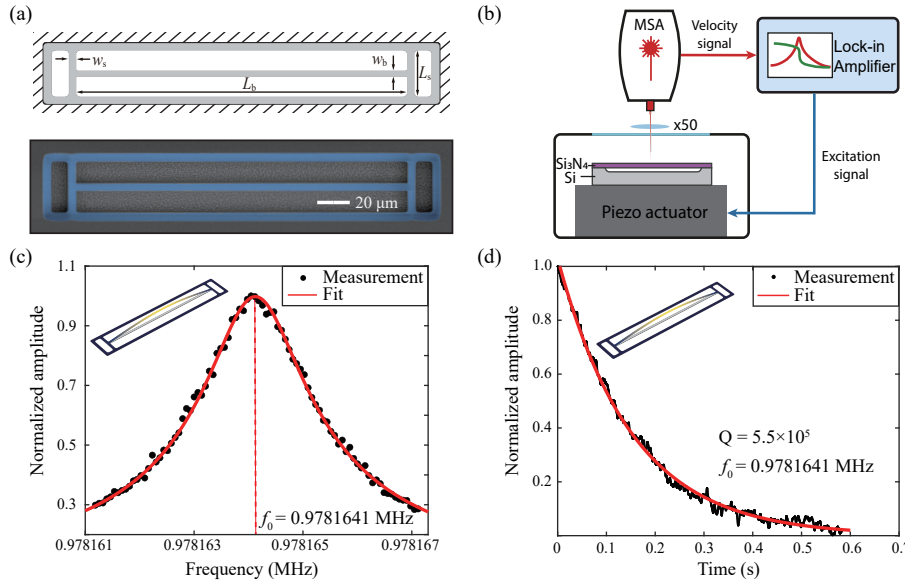

Figure 3.2: **Experimental characterization of the nanomechanical resonators.** (a) False-colored scanning electron microscope (SEM) image of an string resonator with $L = 200\,\mu$m, $w_b = 4\,\mu$m, $L_s = 31\,\mu$m, $w_s = 4.5\,\mu$m and the corresponding numerical model. (b) Schematics of measurement set-up. (c) Harmonic response of the string resonator shown in (a), excited near its fundamental resonance frequency. (d) Ring-down measurement of the string resonator in (a), after stopping the resonant driving of the fundamental mode. The y-axis is normalized to the amplitude at $t = 0$.

release etch. This tension reduction is a consequence of the support's in-plane deflection $\Delta_i = F_b / k_{in}$. To validate these guidelines and explore their potential for enhancing Q, we will now present a more accurate experimental and numerical study of the effect of the support design on the Q-factor of string resonators.

3.3. MEASUREMENT OF RESONANCE FREQUENCY AND Q-FACTOR

All nanomechanical resonators studied in this work are fabricated on the same chip (see Section 2.1.1 in Chapter 2 for the fabrication procedures), which provides identical pre-stress $\sigma_0 = 1.1\,$GPa and thickness $h = 340\,$nm of the Si_3N_4 layer.

To optimize the support design, control is needed over the torsional stiffness k_t, out-of-plane translational stiffness k and string stress σ_b. For this purpose we utilize a rectangular doubly clamped support structure with length L_s and width w_s. The resonator is connected at both ends to the center of such a torsion beam support. The studied Si_3N_4 strings have lengths $L = 100$, 200, 300 and 400 μm. The support length is always kept at $L_s = 31\,\mu$m while the support width varies from $w_s = 1\,\mu$m to $w_s = 8\,\mu$m.

Fig. 3.2a shows a picture of an actual device, whose fundamental resonance frequency is characterized using the measurement set-up shown in Fig. 3.2b. The chip with string resonators is placed on a piezo actuator that shakes the chip to drive the resonators into resonance. To characterize the resonance frequencies and Q-factors, we

use an MSA400 Polytec Laser Doppler Vibrometer connected to a Zurich Instruments HF2LI lock-in amplifier to measure the out-of-plane velocity of the middle of the string, as shown in Fig. 3.2b. The measurements are performed at room temperature in a vacuum chamber at a pressure below 2×10^{-6} mbar to minimize the effect of gas damping.

For each resonator, we perform a frequency sweep in the linear regime to determine the resonance frequency f_0 of the fundamental out-of-plane mode by fitting a Lorentzian to the data points (see Fig. 3.2c). To ensure that the demodulator filter bandwidth does not affect the determination of the Q-factor, we determine Q from the ring-down measurements (see Fig. 3.2d).

Thus, the measured resonance frequencies f_0 and Q-factors of 24 doubly clamped string resonators with varying values of L and w_s are tabulated in Appendix Section 3.6.1. Resonance frequencies range from 0.26 MHz to 2.40 MHz. In addition, we assume that Si_3N_4 is isotropic, with Young's modulus E and loss modulus E' identical in all directions, and characterize a set of singly clamped Si_3N_4 cantilevers to precisely determine the Young's modulus $E = 271$ GPa, and the intrinsic quality factor $Q_0 = 11774$ due to material losses, which is close to literature values [25, 35] (see Section 2.1.2 in Chapter 2).

3.4. STRESS ENGINEERING OF Si_3N_4

A key advantage of the torsion beam support design is that it provides an effective way to control the stress σ_b in the string resonators made from a strained layer with an initial stress σ_0. It thus provides an alternative to the recently presented geometric stress tuning method [32] for obtaining a large number of string resonators, with widely varying σ_b, from 0.15 GPa to 0.74 GPa (see Fig. 3.3b), on the same chip by adjusting the support geometry. After the Si release etch, the high-stress Si_3N_4 string resonators are suspended, and as a consequence of the finite in-plane stiffness k_{in} of the support, the string becomes slightly shorter, which causes the string stress to reduce to σ_b. In Fig. 3.3a we show FE simulations of the effect of the support design on the string stress $\sigma_{b,FEM}$. For small values of w_s, k_{in} reduces, and consequently σ_b in the string is lower after the release etch.

Before analyzing the Q of the resonators, we use their measured f_0 to determine the string stress using the equation for the fundamental resonance frequency $f_0 \approx \sqrt{\sigma_{b,exp}/(4L^2\rho)}$ of a simply supported string:

$$\sigma_{b,exp} \approx 4\rho L^2 f_0^2, \tag{3.2}$$

where the literature value of Si_3N_4 mass density is taken as $\rho = 3100\,kg/m^3$. For the high-stress devices in this work the effect of bending rigidity on σ_b is less than 1% and is therefore neglected [31]. To validate this procedure, we plot in Fig. 3.3b the value of $\sigma_{b,FEM}$ (filled triangles) as obtained from FEM (Fig. 3.3a) against the experimentally determined value $\sigma_{b,exp}$ from Eq. (3.2) for all 24 devices. The correspondence between experiments and simulations gives us confidence in using Eq. (3.2) for extracting the stress in string resonators. The observed stress tuning effect can also be approximated by static analysis (see Section 2.2.1 in Chapter 2) of the string after the release etch:

$$\sigma_{b,an} \approx \frac{\sigma_0(1-\nu)}{1+2EA_b/(k_{in}L)}. \tag{3.3}$$

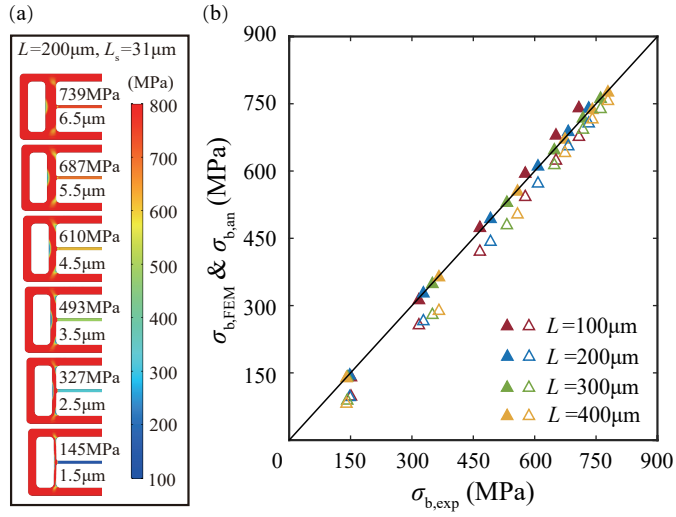

Figure 3.3: **Comparison between experimental and simulated stress.** (a) FE simulations show how the string stress after the release can be varied using the support width design. (b) $\sigma_{b,FEM}$ obtained from FEM (filled triangles) and $\sigma_{b,an}$ calculated from Eq. (3.3) (open triangles, Poisson ratio taken as $\nu = 0.23$ [28, 35]) are plotted against experimentally obtained $\sigma_{b,exp}$ using Eq. (3.2) for resonators of different lengths.

The string stress calculated from this equation is also shown as open triangles in Fig. 3.3b, with the analytical equation providing quite a good approximation of $\sigma_{b,FEM}$ at high stress values, but deviating at lower stresses for the supports with small widths.

Although the resonance frequency mainly depends on the string stress σ_b, which in turn depends on the in-plane stiffness k_{in} of the support, the Q-factor is also sensitive to the torsional and out-of-plane translational stiffness of the support as expected from Eq. (3.1). In Fig. 3.4 we plot the experimentally measured Q-factors for various string lengths L and support widths w_s. Fig. 3.4a shows that a large range of resonance frequencies f_0 and Q-factors can be covered by tuning these two parameters on the same chip. In Fig. 3.4b it can be seen that for each value of L the Q-factor increases with increasing σ_b, as expected from dissipation dilution, with Q increasing approximately proportional to L (as expected from Eq. (3.1)). However, around a stress of 700 MPa, the $Q-\sigma_b$ curve flattens off, showing a maximum value above which a slight reduction in Q is observed.

Although we anticipated such an optimal value of Q in Eq. (3.1), the actual situation is somewhat more complicated. Since in Fig. 3.4b it is not only σ_b ($F_b = A_b\sigma_b$) that is increasing, but actually increasing w_s also causes simultaneous increase of the support's k_t and k. To fully capture this effect we present in Fig. 3.4 simulated values of Q both using FEM (circles), and using an analytical model (solid lines) that solves the Euler-Bernoulli beam equation in the presence of stress [10] for the boundary conditions given in Fig. 3.1 (see Appendix Section 3.6.3 and 3.6.4). The FE simulations capture the experimental Q values closely. The analytical model, which determines the values of k_t and k from the support geometry (see Appendix Section 3.6.2), also captures Q quite well, although it overestimates Q for the longer string lengths by 17%. It is important to note that the

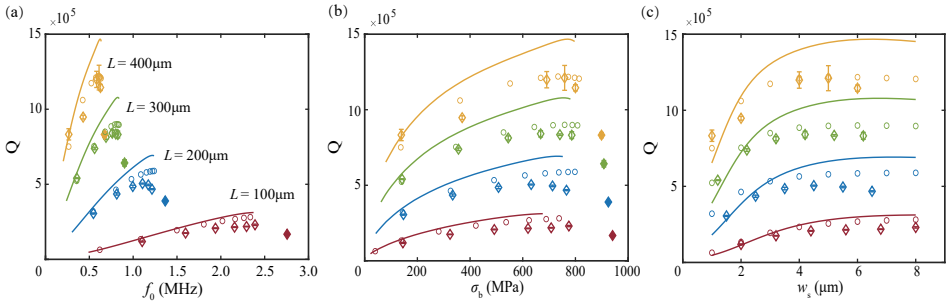

Figure 3.4: **Effect of support design on Q.** The figures show Q as a function of fundamental resonance frequency f_0 (a), stress $\sigma_{b,exp}$ calculated from Eq. (3.2) (b), and support width w_s (c). Experimental results (diamonds) are compared to those obtained by FEM (circles) and analytically (solid lines). The solid diamonds represent the experimental Q-factors of directly clamped strings without torsion supports. All samples have $L_s = 31\mu m$ and $w_b = 2\mu m$, while L and w_s are varied. All data with the same L (labels in 3.4a) has the same color.

maximum values obtained in strings with torsion beam supports (open diamonds), is substantially higher (up to 50%) than the Q obtained in directly clamped strings of the same length (filled diamonds), despite the higher stress σ_b in those directly clamped ones (see Fig. 3.4b). This observation provides evidence that not only high string stress σ_b, but also low torsional stiffness of the support k_t is required for obtaining high Q.

Moreover, we should realize that to reach a high maximum quality factor $Q_{max} \approx \frac{Q_0 L}{8}\sqrt{k/k_t}$ requires not only a low torsional stiffness k_t, but also a large out-of-plane translational stiffness k. However, for the torsion design presented here—and many other compliant support designs—decreasing k_t, *e.g.*, by reducing w_s or increasing L_s, will also decrease k such that their ratio is not easily tuned by the orders of magnitude that are needed to reach record Q values. An extensive study of the Q-factor as function of w_s and L_s is presented in Appendix Section 3.6.4 to assess the influence from supports' geometry over a larger parameter range. The presented models and experiments thus expose a trade-off that has to be made among σ_b, k, and k_t, which limits the ultimate Q that can be obtained using string resonators with compliant supports.

A potential method to overcome this limitation is the use of periodic string resonators that move out of phase, like the one illustrated in Fig. 3.5. By having anti-symmetrically vibrating resonators with respect to a central support, the effect of two opposite forces F_b on the support cancel, and the support displacement is equal to zero. This allows reducing k_t to a very low value without diminishing σ_b. This periodic resonator configuration resolves two issues: Firstly, the spring k is not deflected in the out-of-plane direction (such that W_k is zero in Eq. (3.1)), and secondly, σ_b in the string does not depend on the in-plane stiffness k_{in} of the support anymore, since the in-plane displacement of the support has also become zero. As a consequence, k_t can be minimized without leading to a reduction of k_{in} and σ_b.

However, in a linear configuration this periodicity cannot be continued indefinitely, and non-periodic end-supports are needed. An interesting idea to avoid the necessity of such end-supports is to couple the periodic anti-symmetric resonators at a $180°/n$ (integer $n > 1$) angle via torsion springs with very low k_t in a regular polygon arrangement,

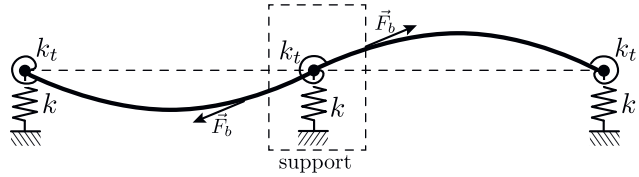

Figure 3.5: **Periodic string resonator configuration.** The anti-symmetric vibration mode stablizes the translational displacement of the central support and preserves the high stress in the string at the same time.

as was recently demonstrated [35, 36], yielding record-high Q values exceeding a billion.

In the presence of periodic boundary conditions, k and k_{in} become infinitely large such that the only relevant parameters in Eq. (3.1) are F_{b} and k_{t}. Thus the ultimate value of the $f_0 Q$ product (for $h^2 \ll w_{\text{s}}^2$ and assuming other loss mechanisms are negligible) approximately becomes (see Appendix Section 3.6.5):

$$\left(f_0 \times Q\right)_{\max} \approx \frac{3Q_0(1-\nu)^{\frac{3}{2}}\sigma_0{}^{\frac{1}{2}}\, w_{\text{b}} L_{\text{s}}}{8\rho^{\frac{1}{2}}\, w_{\text{s}}^3}. \tag{3.4}$$

It is interesting to note that in the ultimate limit, the $f_0 Q$ product in Eq. (3.4) has become independent of the string thickness and string length, such that it mainly depends on the design of the support (w_{s} and L_{s}) and increasing it will require supports with very low torsional stiffness.

3.5. CONCLUSION

In conclusion, we have analyzed the effect of support design on the Q-factor of high-stress Si_3N_4 nanomechanical string resonators. By engineering torsion beam supports, we control the resonator's stress σ_{b} as well as the support's torsional stiffness k_{t} and out-of-plane translational stiffness k without any post-fabrication manipulation [23]. Tuning these parameters over a large range allows us to investigate their role on the dissipation and present validated models for estimating the mechanical Q of string resonators. More importantly, we find that the interplay between these geometric parameters allows us to determine the optimal support geometry that optimizes Q for string resonators of fixed length. The Q cannot be increased indefinitely due to design trade-offs that limit the possibility to design supports that both have low torsional stiffness k_{t} and high in-plane stiffness k_{in}. It is this realisation that explains the success of soft-clamping and periodic clamping methodologies which can further increase Q above the limits of simple string resonators. The challenge remains to find the most effective way to create high-Q resonators with minimal device dimensions. The presented models, methods and insights can help towards achieving higher Q-factors, without requiring ever increasing device areas and provide a route towards realizing arrays of sensor devices with widely varying values of f_0 and Q on the same chip with optimal sensitivity and resolution [37].

3.6. APPENDIX

3.6.1. MEASURED FUNDAMENTAL RESONANCE FREQUENCIES AND Q-FACTORS

In Appendix Table 3.1 to 3.4, we provide all the data we measured on the string resonators with torsion supports. Each value is the average of three measurement values on the same sample under 2×10^{-6} mbar. In order to avoid the sample breakage caused by the stress concentration, all fillets at the clamping point of the string to the support have a radius of curvature of $r_1 = 1\mu m$, and at the edge of the support $r_1 = 2.5\mu m$. The lateral Si_3N_4 underetch distance is $2.5\mu m$. Since the resonators with $w_b = 2\mu m$ have the most mechanical similarity with the analytical model we derived, all the figures and analysis in this work are based on the last column of these tables. The broken devices are marked as "—".

Table 3.1: The experimental resonance frequencies and Q factors for fundamental mode of resonators with $L = 100\mu m$, $L_s = 31\mu m$

w_s (μm)	$w_b = 4\mu m$		$w_b = 3\mu m$		$w_b = 2\mu m$	
	f_0 (Hz)	Q	f_0 (Hz)	Q	f_0 (Hz)	Q
8.0	2153611	237381	2255120	234625	2390175	230119
6.8	2032995	255218	2143855	240938	2293107	218529
5.6	1859545	227908	1986077	207367	2156734	214572
4.4	1630138	210631	1752332	203058	1938560	207397
3.2	1302037	153490	1410034	171461	1597774	175124
2.0	880465	112285	958640	112276	1102779	118605

Table 3.2: The experimental resonance frequencies and Q factors for fundamental mode of resonators with $L = 200\mu m$, $L_s = 31\mu m$

w_s (μm)	$w_b = 4\mu m$		$w_b = 3\mu m$		$w_b = 2\mu m$	
	f_0 (Hz)	Q	f_0 (Hz)	Q	f_0 (Hz)	Q
6.5	1122846	574606	1162975	528073	1214642	467460
5.5	1065002	558631	1111544	545814	1172910	495702
4.5	979679	532453	1033290	525524	1106708	504783
3.5	853871	509587	911307	444745	995847	485443
2.5	672769	427813	725676	405086	812937	435193
1.5	437441	292891	476511	284203	546540	305649

3.6.2. ANALYTICAL MODEL FOR TRANSLATIONAL STIFFNESS k AND TORSIONAL STIFFNESS k_t

The translational stiffness of the support k is derived according to the central deformation of an axially stressed doubly clamped beam under concentrated force [38] (page 158). The in-plane deformation will prevent the out-of-plane bending of a wide beam, so the stiffening effect is taken into account by using $E/(1-\nu^2)$ [38] (page 169).

Table 3.3: The experimental resonance frequencies and Q factors for fundamental mode of resonators with $L = 300\,\mu\text{m}$, $L_s = 31\,\mu\text{m}$

w_s (μm)	$w_b = 4\,\mu\text{m}$		$w_b = 3\,\mu\text{m}$		$w_b = 2\,\mu\text{m}$	
	f_0 (Hz)	Q	f_0 (Hz)	Q	f_0 (Hz)	Q
6.2	777486	921184	799035	901508	825598	831771
5.2	742561	881555	768315	924893	802074	834908
4.2	687768	879462	719496	867821	761951	840643
3.2	559702	791338	637035	565082	690162	813058
2.2	466790	747799	—	—	560101	738445
1.2	286078	520066	312118	541304	357190	540585

Table 3.4: The experimental resonance frequencies and Q factors for fundamental mode of resonators with $L = 400\,\mu\text{m}$, $L_s = 31\,\mu\text{m}$

w_s (μm)	$w_b = 4\,\mu\text{m}$		$w_b = 3\,\mu\text{m}$		$w_b = 2\,\mu\text{m}$	
	f_0 (Hz)	Q	f_0 (Hz)	Q	f_0 (Hz)	Q
6.0	596570	1305145	610251	1246085	626782	1145119
5.0	572598	1269172	589420	1239181	611087	1210778
4.0	533363	906394	554652	1202736	583012	1198681
3.0	466873	1183917	492836	1194633	530482	591766
2.0	360538	1053545	386559	1087169	429390	947508
1.0	212508	854658	231646	792134	265533	832711

$$k = \frac{\mu\sigma_s A_s}{\frac{\mu L_s}{4} - \tanh\left(\frac{\mu L_s}{4}\right)}$$
$$\mu = \sqrt{\frac{\sigma_s A_s}{E/(1-\nu^2) I_{so}}} \tag{3.5}$$

The torsional stiffness k_t of the support beam is derived according to the central rotating angle of an axially stressed doubly clamped beam under concentrated torque:

$$k_t = 4\frac{KG + \sigma_s J}{L_s}, \tag{3.6}$$

where $G = E/(2(1+\nu))$ is the shear modulus and $J = I_{so} + I_{si}$ is the polar moment of inertia [38] (page 397), $I_{si} = h w_s^3/12$ is the in-plane moment of inertia, $I_{so} = h^3 w_s/12$ is its out-of-plane moment of inertia, and K is a function of the rectangular cross section [38]:

$$K = w_s h^3 \left(\frac{1}{3} - 0.21\frac{h}{w_s}\left(1 - \frac{h^4}{12 w_s^4}\right)\right) \tag{3.7}$$

In order to check the accuracy of these analytical expressions, we calculate the stress in the string σ_b, the torsion spring k_t and the translational spring k of the support by FE

simulations in COMSOL. The stress in the central string after release σ_b is simulated by static analysis, same to the way in Fig. 3.3a. For torsion spring k_t and the translational spring k, as shown in Fig. 3.6, an out-of-plane concentrated force $F_z = 1 \times 10^{-6}$ N, which is orders of magnitude smaller than F_b to ensure linear deflection, is added on the different places of the support to induce torsion and bending of it. z_{max} and z_{min} shown in Fig. 3.6a are extracted to calculate the torsion angle $\theta = (z_{max} - z_{min})/w_s$. The moment generated by the out-of-plane force is $M = F_z w_s$, and $k_t = M/\theta$. z_c shown in Fig. 3.6b is the deflection of the center point on the support, which is induced by the concentrated force F_z loaded at the same place. With the force and numerically calculated deflection, we can determine the supports' torsional stiffness $k_{t,FEM}$ and translational stiffness k_{FEM}:

$$k_{t,FEM} = \frac{F_z w_s^2}{z_{max} - z_{min}}$$
$$k_{FEM} = \frac{F_z}{z_c} \tag{3.8}$$

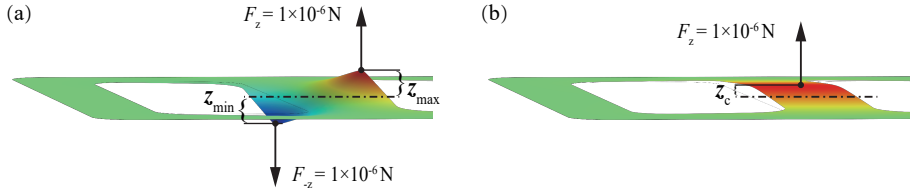

Figure 3.6: The FE simulation used to determine the supports' (a) torsional stiffness $k_{t,FEM}$ and (b) translational stiffness k_{FEM}.

With the analytical expressions for σ_b (see Eq.(2.5) in Chapter 2), k, k_t and their simulated values σ_b, $k_{t,FEM}$ and k_{FEM}, we can plot their values as functions of support width w_s while keeping other geometric parameters the same, similar to the experimental devices in Appendix Tables 3.1-3.4. We can see from Fig. 3.7 that as w_s increasing, σ_b, k_t and k are all becoming larger as expected. The agreement between FEM results and analytical model is quite good, although not perfect. These differences might be due to the approximations in the analytical equations and also due to the absence of fillets and the assumption $\sigma_s = \sigma_0$ in the analytical model. The imperfections in the analytical model can also account for the differences between the analytical and FE-simulated Q-factor in Fig. 3.4.

3.6.3. SOLVING THE MODE SHAPE OF THE CENTRAL STRING

For clamped-clamped strings, most of the dissipation is caused by bending near the clamping boundary. Therefore, an accurate calculation of the mode shape near that point is of importance for predicting the Q factor. Here we approximate the support by a combination of a torsion spring k_t and a translational spring k just like in Fig. 3.1 of the main text. With these boundary conditions, we derive the mode shapes $\phi_b(x)$ of a pre-stressed string, with out-of-plane deflection. The undamped bending vibration of a pre-stressed Euler–Bernoulli beam can be described [10] by the differential equation:

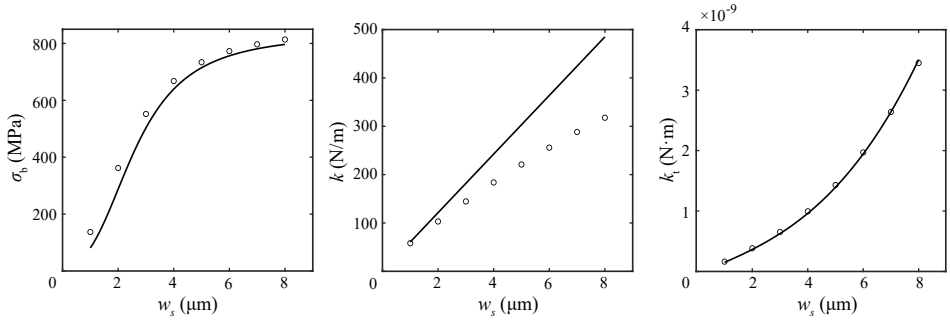

Figure 3.7: FE simulations and analytical calculations of the influence of support width w_s on left: pre-stress in the central beam σ_b, middle: stiffness of the torsional spring k_t and right: stiffness of the translational spring k. The graphs show simulations for devices with the same beam length $L = 400\,\mu$m, beam width $w_b = 2\,\mu$m and support length $L_s = 31\,\mu$m. The solid lines stand for the analytical results while the solid circles are the FE-simulated values using the method shown in Fig. 3.6.

$$\rho A_b \frac{\partial^2 w(x,t)}{\partial t^2} + EI_b \frac{\partial^4 w(x,t)}{\partial x^4} - \sigma_b A_b \frac{\partial^2 w(x,t)}{\partial x^2} = 0 \tag{3.9}$$

By using the method of separation of variables, namely $w(x,t) = \phi_b(x)\cos(\omega t)$, we have:

$$\frac{d^4\phi_b(x)}{dx^4} - \frac{\sigma_b A_b}{EI_b}\frac{d^2\phi_b(x)}{dx^2} - \frac{\omega^2 \rho A_b}{EI_b}\phi_b(x) = 0 \tag{3.10}$$

where ρ is the density of high-stress Si_3N_4, ω is the eigenvalue of the beam. Then its general solutions can be written in the form [39]:

$$\phi_b(x) = c_1\cos(\gamma x) + c_2\sin(\gamma x) + c_3\cosh(\delta x) + c_4\sinh(\delta x) \tag{3.11}$$

where it is found by substituting a trial function $\phi_{b,t}(x,t) = \phi_b(x)\cos(\omega t)$ into the differential equation that:

$$\begin{aligned} \gamma^2 &= \delta^2 - \alpha^2 \\ \alpha^2 &= \frac{\sigma_b A_b}{EI_b} \end{aligned} \tag{3.12}$$

Furthermore, it follows that $\delta^2 = \frac{1}{2}\left(\alpha^2 + \sqrt{\alpha^4 + 4\frac{\omega^2\rho A_b}{EI_b}}\right)$, which allows determining the resonance frequency ω from δ. For our equivalent model of a central string with torsional springs k_t and translational springs k, the sum of the moments and sum of forces at each end of the string need to be zero, which results in these four boundary conditions:

$$
\begin{aligned}
EI_{\mathrm{b}}\frac{\mathrm{d}^3\phi_b(x)}{\mathrm{d}x^3}+k\phi_{\mathrm{b}}(x)-\sigma_{\mathrm{b}}A_{\mathrm{b}}\frac{\mathrm{d}\phi_{\mathrm{b}}(x)}{\mathrm{d}x}\bigg|_{x=-\frac{L}{2}}&=0\\
-EI_{\mathrm{b}}\frac{\mathrm{d}^2\phi_{\mathrm{b}}(x)}{\mathrm{d}x^2}+k_{\mathrm{t}}\frac{\mathrm{d}\phi_{\mathrm{b}}(x)}{\mathrm{d}x}\bigg|_{x=-\frac{L}{2}}&=0\\
-EI_{\mathrm{b}}\frac{\mathrm{d}^3\phi_{\mathrm{b}}(x)}{\mathrm{d}x^3}+k\phi_{\mathrm{b}}(x)+\sigma_{\mathrm{b}}A_{\mathrm{b}}\frac{\mathrm{d}\phi_{\mathrm{b}}(x)}{\mathrm{d}x}\bigg|_{x=\frac{L}{2}}&=0\\
EI_{\mathrm{b}}\frac{\mathrm{d}^2\phi_{\mathrm{b}}(x)}{\mathrm{d}x^2}+k_{\mathrm{t}}\frac{\mathrm{d}\phi_{\mathrm{b}}(x)}{\mathrm{d}x}\bigg|_{x=\frac{L}{2}}&=0
\end{aligned}
\tag{3.13}
$$

By substituting the assumed mode shape Eq. (3.11) into the boundary conditions above, we have:

$$
\begin{bmatrix}
(-\gamma^3 EI_{\mathrm{b}}-\gamma\sigma_{\mathrm{b}}A_{\mathrm{b}})\sin(\gamma\frac{L}{2})+k\cos(\gamma\frac{L}{2}) & (-\gamma^3 EI_{\mathrm{b}}-\gamma\sigma_{\mathrm{b}}A_{\mathrm{b}})\cos(\gamma\frac{L}{2})-k\sin(\gamma\frac{L}{2})\\
\gamma^2 EI_{\mathrm{b}}\cos(\gamma\frac{L}{2})+\gamma k_{\mathrm{t}}\sin(\gamma\frac{L}{2}) & -\gamma^2 EI_{\mathrm{b}}\sin(\gamma\frac{L}{2})+\gamma k_{\mathrm{t}}\cos(\gamma\frac{L}{2})\\
(-\gamma^3 EI_{\mathrm{b}}-\gamma\sigma_{\mathrm{b}}A_{\mathrm{b}})\sin(\gamma\frac{L}{2})+k\cos(\gamma\frac{L}{2}) & (\gamma^3 EI_{\mathrm{b}}+\gamma\sigma_{\mathrm{b}}A_{\mathrm{b}})\cos(\gamma\frac{L}{2})+k\sin(\gamma\frac{L}{2})\\
-\gamma^2 EI_{\mathrm{b}}\cos(\gamma\frac{L}{2})-\gamma k_{\mathrm{t}}\sin(\gamma\frac{L}{2}) & -\gamma^2 EI_{\mathrm{b}}\sin(\gamma\frac{L}{2})+\gamma k_{\mathrm{t}}\cos(\gamma\frac{L}{2})
\end{bmatrix}
$$

$$
\begin{bmatrix}
(-\delta^3 EI_{\mathrm{b}}+\delta\sigma_{\mathrm{b}}A_{\mathrm{b}})\sinh(\delta\frac{L}{2})+k\cosh(\delta\frac{L}{2}) & (\delta^3 EI_{\mathrm{b}}-\delta\sigma_{\mathrm{b}}A_{\mathrm{b}})\cosh(\delta\frac{L}{2})-k\sinh(\delta\frac{L}{2})\\
-\delta^2 EI_{\mathrm{b}}\cosh(\delta\frac{L}{2})-\delta k_{\mathrm{t}}\sinh(\delta\frac{L}{2}) & \delta^2 EI_{\mathrm{b}}\sinh(\delta\frac{L}{2})+\delta k_{\mathrm{t}}\cosh(\delta\frac{L}{2})\\
(-\delta^3 EI_{\mathrm{b}}+\delta\sigma_{\mathrm{b}}A_{\mathrm{b}})\sinh(\delta\frac{L}{2})+k\cosh(\delta\frac{L}{2}) & (-\delta^3 EI_{\mathrm{b}}+\delta\sigma_{\mathrm{b}}A_{\mathrm{b}})\cosh(\delta\frac{L}{2})+k\sinh(\delta\frac{L}{2})\\
\delta^2 EI_{\mathrm{b}}\cosh(\delta\frac{L}{2})+\delta k_{\mathrm{t}}\sinh(\delta\frac{L}{2}) & \delta^2 EI_{\mathrm{b}}\sinh(\delta\frac{L}{2})+\delta k_{\mathrm{t}}\cosh(\delta\frac{L}{2})
\end{bmatrix}
\begin{Bmatrix} c_1\\ c_2\\ c_3\\ c_4 \end{Bmatrix}
=
\begin{Bmatrix} 0\\ 0\\ 0\\ 0 \end{Bmatrix}
\tag{3.14}
$$

A non-trivial solution exists for this homogeneous system if the determinant equals to zero, which is also known as the frequency equation. After substituting Eq. (3.12) into the frequency equation, we can solve for δ, and determine γ and ω from it. Then we can solve for the c_2, c_3, c_4 as functions of c_1 and obtain the mode shape ϕ_{b} of a pre-stressed beam with torsional springs k_{t} and translational springs k on both of its ends. Note that when the boundary conditions on both ends $x=\pm L/2$ are identical, the symmetry of the system will cause the mode shapes to be either even upon reflection in $x=0$, such that $c_2=c_4=0$, or is purely odd, such that $c_1=c_3=0$. Using this property can significantly speed up the analysis, reducing the 4×4 matrix to a 2×2 matrix.

3.6.4. ANALYTICAL CALCULATION OF Q-FACTOR

The Q-factor of a pre-stressed resonator can be expressed as [33]:

$$
\begin{aligned}
Q&=2\pi\frac{W_{\text{tension}}+W_{\text{bending}}+W_{\text{torsion}}}{\Delta W_{\text{bending}}+\Delta W_{\text{torsion}}}\\
&=\left(\frac{W_{\text{tension}}}{W_{\text{bending}}+W_{\text{torsion}}}+1\right)Q_0\\
&=\left(\frac{W_{\text{tension,b}}+W_{\text{tension,s}}}{W_{\text{bending,b}}+W_{\text{bending,s}}+W_{\text{torsion,s}}}+1\right)Q_0,
\end{aligned}
\tag{3.15}
$$

where W_{tension} is the mode-shape's stored tension energy, $\Delta W_{\text{bending}}$ and W_{bending} are the bending loss per cycle and the stored bending energy respectively, $\Delta\ W_{\text{torsion}}$ and W_{torsion} are the torsional loss per cycle and stored torsion energy respectively. Subscripts

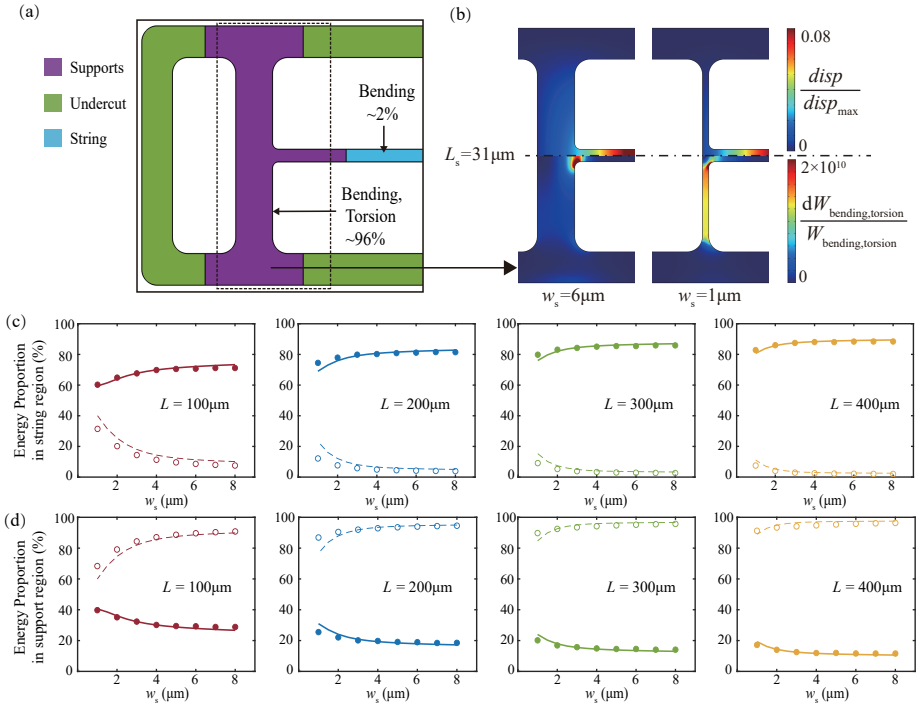

Figure 3.8: Comparison of energy distribution of different string resonators. (a) The illustration of energy distribution for the out-of-plane fundamental mode of a string resonator with $L = 400\mu m$, $w_b = 2\mu m$, $L_s = 31\mu m$, $w_s = 6\mu m$. (b) The comparison of the normalized total displacement (up) and the loss density (down) of the string resonator in (a) with different w_s. (c) and (d) The comparison of energy distribution in central string and supports, as the regions shown in blue and purple in (a). The solid lines and filled circles represent the tension energy $(W_{tension}/W_{tension,total}) \times 100\%$ from analytical results and FE simulations, respectively. The dashed lines and hollow circles represent the bending and torsion energy $(W_{bending} + W_{torsion})/(W_{bending,total} + W_{torsion,total}) \times 100\%$ from analytical results and FE simulations, respectively.

"b" and "s" refer to the central string and support beams respectively. Q_0 is the intrinsic material quality factor, which can be expressed as $Q_0 = E/E'$. To estimate Q for a supported string resonator in Eq. (3.15), we subdivided its stored energy into tension energy, bending energy and torsion energy of the string resonator itself and of the supports. When beams bend or undergo torsional deformation, the energy dissipated per cycle is $\Delta W = 2\pi W/Q_0$, whereas tension energy, according to the dissipation dilution effect, does not lead to a linear dissipation contribution.

From the mode shape calculated in the last section, we can analytically calculate the stored tension and bending energy in the string from the mode shape $\phi_b(x)$ as follows:

$$W_{\text{tension,b}} = \frac{1}{2}\sigma_{\text{b}} A \int_{-\frac{L}{2}}^{\frac{L}{2}} \left(\frac{\partial \phi_{\text{b}}}{\partial x}\right)^2 \mathrm{d}x$$
$$W_{\text{bending,b}} = \frac{1}{2} E I_{\text{b}} \int_{-\frac{L}{2}}^{\frac{L}{2}} \left(\frac{\partial^2 \phi_{\text{b}}}{\partial x^2}\right)^2 \mathrm{d}x \tag{3.16}$$

Then we can derive the energy stored in support beams with the boundary displacement $\Delta_{\text{o}} = \phi_{\text{b}}(-\frac{L}{2})$ and the rotating angle $\tau_{\text{s}} = \phi_{\text{b}}^{'}(-\frac{L}{2})$. For k, we have $k_{\text{E}} = \frac{192 E I_{\text{si}}}{(1-\nu^2) L_{\text{s}}^3}$ contributed by the bending rigidity, which also takes the stiffening effect into account, and $k_{\sigma_{\text{b}}} = k - k_{\text{E}}$ by the stress σ_{s} along the support beams. For k_{t}, we have $k_{\text{t}} = \frac{4KG}{L_{\text{s}}}$ contributed by the torsion rigidity and $k_{\text{t}\sigma_{\text{b}}} = \frac{4\sigma_{\text{s}} J}{L_{\text{s}}}$ by the stress σ_{s} along the support beams together with the stress σ_{b} in central beam.

$$W_{\text{tension,s}} = \frac{1}{2} k_{\sigma_{\text{b}}} {\Delta_{\text{o}}}^2 + \frac{1}{2} k_{\text{t}\sigma_{\text{b}}} {\tau_{\text{s}}}^2$$
$$W_{\text{bending,s}} = 2 \times \frac{1}{2} k_{\text{E}} {\Delta_{\text{o}}}^2 \tag{3.17}$$
$$W_{\text{torsion,s}} = 2 \times \frac{1}{2} k_{\text{t}} {\tau_{\text{s}}}^2$$

As shown in Fig. 3.8, the energy distribution calculated by the analytical model matches well to the FE simulation. Differences can be attributed to inaccuracies in the analytical model, not including the effects of fillets and the approximation $\sigma_{\text{s}} = \sigma_0$. It can be seen that the percentage of energy stored in the central string of the resonator increases with increasing support width w_{s}, which is mainly attributed to the higher stress σ_{b} that is maintained by the stiffer supports.

The Q-factor analytically calculated according to the above mentioned procedure is plotted against L_{s} and w_{s} for four values of the central string length L in Fig. 3.9a-d. A numerically calculated result by FE simulation is also shown to provide the comparison to the analytical results in Fig. 3.9e. With both calculation procedure, we can see that an optimal region of Q exists for all L studied in our work.

3.6.5. DERIVING THE ULTIMATE VALUE OF $f_0 \times Q$

For the periodic boundary conditions where the effective translational stiffness k and in-plane stiffness k_{in} are infinitely large, Eq. 3.1 could be simplified as:

$$Q = \left(\frac{W_\sigma}{2W_{\text{k}} + 2W_{\text{t}}} + 1\right) Q_0 \approx \frac{Q_0 L}{4} \left(\frac{F_{\text{b}}}{k} + \frac{k_{\text{t}}}{F_{\text{b}}}\right)^{-1} \approx \frac{Q_0 L}{4} \frac{F_{\text{b}}}{k_{\text{t}}}, \tag{3.18}$$

where k_{t} is mentioned in Eq. (3.6) and $F_{\text{b}} = \sigma_{\text{b}} A_{\text{b}} = (1-\nu)\sigma_0 A_{\text{b}}$ according to the stress redistribution of a doubly clamped beam with isotropic initial stress σ_0. By substituting the expression of k_{t}, F_{b} and $f_0 = \sqrt{\sigma_{\text{b}}/(4L^2\rho)}$ into the $f_0 Q$ product, we have:

$$f_0 \times Q = \frac{3 Q_0 (1-\nu)^{\frac{3}{2}} \sigma_0^{\frac{3}{2}} w_{\text{b}} L_{\text{s}}}{8\rho^{\frac{1}{2}} w_{\text{s}}} \frac{1}{\frac{2Eh^2}{(1+\nu)} + \sigma_0 (h^2 + w_{\text{s}}^2)}. \tag{3.19}$$

For the case that $h^2 \ll w_{\text{s}}^2$, Eq. (3.19) can be approximated as:

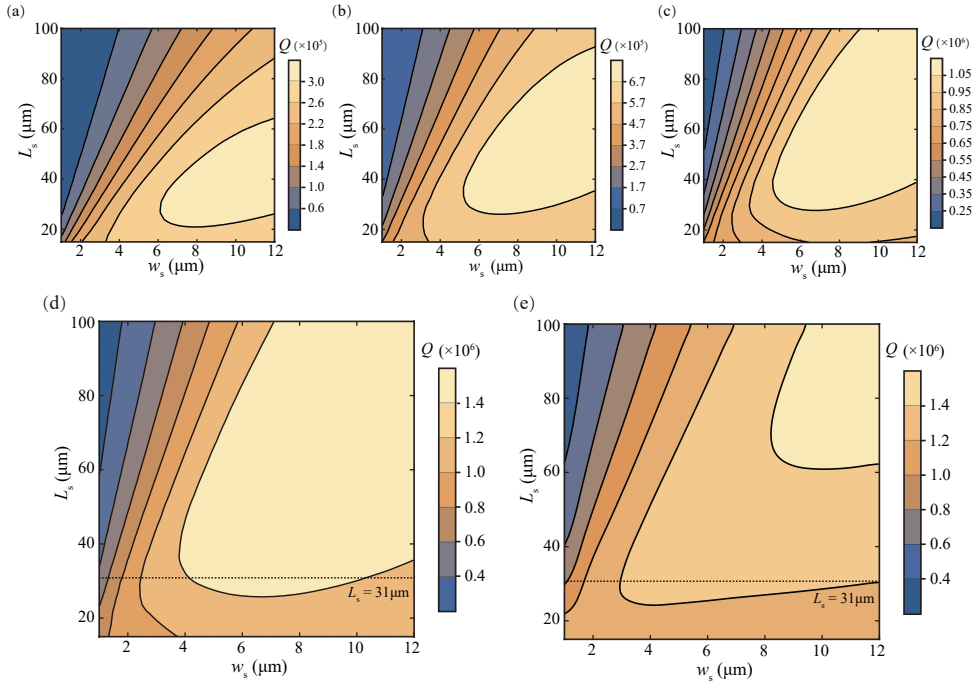

Figure 3.9: Contour plot of Q-factor of the resonators as a function of support width w_s and support length L_s. Analytically calculated Q-factor for (a) $L = 300\mu$m, (b) $L = 200\mu$m, (c) $L = 100\mu$m and (d) $L = 400\mu$m. (e) Numerically calculated Q-factor for $L = 400\mu$m by FE simulation as a comparison of (d).

$$f_0 \times Q \approx \frac{3Q_0(1-\nu)^{\frac{3}{2}}\sigma_0{}^{\frac{1}{2}}w_b L_s}{8\rho^{\frac{1}{2}}w_s^3}. \tag{3.20}$$

BIBLIOGRAPHY

[1] A. K. Naik, M. Hanay, W. Hiebert, X. Feng, and M. L. Roukes, "Towards single-molecule nanomechanical mass spectrometry", Nature Nanotechnology **4**, 445–450 (2009).

[2] J. Chaste, A. Eichler, J. Moser, G. Ceballos, R. Rurali, and A. Bachtold, "A nanomechanical mass sensor with yoctogram resolution", Nature Nanotechnology **7**, 301–304 (2012).

[3] H. Mamin and D. Rugar, "Sub-attonewton force detection at millikelvin temperatures", Applied Physics Letters **79**, 3358–3360 (2001).

[4] D. Rugar, R. Budakian, H. Mamin, and B. Chui, "Single spin detection by magnetic resonance force microscopy", Nature **430**, 329–332 (2004).

[5] M. Wang, R. Zhang, R. Ilic, V. Aksyuk, and Y. Liu, "Frequency stabilization of nanomechanical resonators using thermally invariant strain engineering", Nano Letters **20**, 3050–3057 (2020).

[6] F. J. Giessibl and H. Bielefeldt, "Physical interpretation of frequency-modulation atomic force microscopy", Physical Review B **61**, 9968 (2000).

[7] M. Suter, O. Ergeneman, J. Zürcher, S. Schmid, A. Camenzind, B. J. Nelson, and C. Hierold, "Superparamagnetic photocurable nanocomposite for the fabrication of microcantilevers", Journal of Micromechanics and Microengineering **21**, 025023 (2011).

[8] J. D. Teufel, D. Li, M. Allman, K. Cicak, A. Sirois, J. Whittaker, and R. Simmonds, "Circuit cavity electromechanics in the strong-coupling regime", Nature **471**, 204–208 (2011).

[9] T. J. Kippenberg and K. J. Vahala, "Cavity optomechanics: back-action at the mesoscale", Science **321**, 1172–1176 (2008).

[10] S. Schmid, L. G. Villanueva, and M. L. Roukes, *Fundamentals of nanomechanical resonators*, Vol. 49 (Springer, 2016).

[11] A. D. O'Connell, M. Hofheinz, M. Ansmann, R. C. Bialczak, M. Lenander, E. Lucero, M. Neeley, D. Sank, H. Wang, M. Weides, et al., "Quantum ground state and single-phonon control of a mechanical resonator", Nature **464**, 697–703 (2010).

[12] R. A. Norte, J. P. Moura, and S. Gröblacher, "Mechanical resonators for quantum optomechanics experiments at room temperature", Physical Review Letters **116**, 147202 (2016).

[13] M. Rossi, D. Mason, J. Chen, Y. Tsaturyan, and A. Schliesser, "Measurement-based quantum control of mechanical motion", Nature **563**, 53–58 (2018).

[14] T. Purdy, K. Grutter, K. Srinivasan, and J. Taylor, "Quantum correlations from a room-temperature optomechanical cavity", Science **356**, 1265–1268 (2017).

[15] J. M. L. Miller, A. Ansari, D. B. Heinz, Y. Chen, I. B. Flader, D. D. Shin, L. G. Villanueva, and T. W. Kenny, "Effective quality factor tuning mechanisms in micromechanical resonators", Applied Physics Reviews **5**, 041307 (2018).

[16] E. Kenig and M. Cross, "Frequency precision of oscillators based on high-Q resonators", arXiv preprint arXiv:1510.07331 (2015).

[17] A. H. Ghadimi, D. J. Wilson, and T. J. Kippenberg, "Radiation and internal loss engineering of high-stress silicon nitride nanobeams", Nano Letters **17**, 3501–3505 (2017).

[18] H. B. Callen and T. A. Welton, "Irreversibility and generalized noise", Physical Review **83**, 34 (1951).

[19] U. Delić, M. Reisenbauer, K. Dare, D. Grass, V. Vuletić, N. Kiesel, and M. Aspelmeyer, "Cooling of a levitated nanoparticle to the motional quantum ground state", Science **367**, 892–895 (2020).

[20] J. Guo, R. Norte, and S. Gröblacher, "Feedback cooling of a room temperature mechanical oscillator close to its motional ground state", Physical Review Letters **123**, 223602 (2019).

[21] Q. P. Unterreithmeier, T. Faust, and J. P. Kotthaus, "Damping of nanomechanical resonators", Physical Review Letters **105**, 027205 (2010).

[22] D. R. Southworth, R. A. Barton, S. S. Verbridge, B. Ilic, A. D. Fefferman, H. G. Craighead, and J. M. Parpia, "Stress and silicon nitride: a crack in the universal dissipation of glasses", Physical Review Letters. **102**, 225503 (2009).

[23] S. S. Verbridge, D. F. Shapiro, H. G. Craighead, and J. M. Parpia, "Macroscopic tuning of nanomechanics: substrate bending for reversible control of frequency and quality factor of nanostring resonators", Nano Letters **7**, 1728–1735 (2007).

[24] P.-L. Yu, T. Purdy, and C. Regal, "Control of material damping in high-Q membrane microresonators", Physical Review Letters **108**, 083603 (2012).

[25] L. G. Villanueva and S. Schmid, "Evidence of surface loss as ubiquitous limiting damping mechanism in sin micro-and nanomechanical resonators", Physical Review Letters **113**, 227201 (2014).

3

[26] S. A. Fedorov, N. J. Engelsen, A. H. Ghadimi, M. J. Bereyhi, R. Schilling, D. J. Wilson, and T. J. Kippenberg, "Generalized dissipation dilution in strained mechanical resonators", Physical Review B **99**, 054107 (2019).

[27] P. Sadeghi, M. Tanzer, S. L. Christensen, and S. Schmid, "Influence of clamp-widening on the quality factor of nanomechanical silicon nitride resonators", Journal of Applied Physics **126**, 165108 (2019).

[28] S. A. Fedorov, A. Beccari, N. J. Engelsen, and T. J. Kippenberg, "Fractal-like mechanical resonators with a soft-clamped fundamental mode", Physical Review Letters **124**, 025502 (2020).

[29] Y. Tsaturyan, A. Barg, E. S. Polzik, and A. Schliesser, "Ultracoherent nanomechanical resonators via soft clamping and dissipation dilution", Nature Nanotechnology **12**, 776–783 (2017).

[30] C. Reetz, R. Fischer, G. G. Assumpcao, D. P. McNally, P. S. Burns, J. C. Sankey, and C. A. Regal, "Analysis of membrane phononic crystals with wide band gaps and low-mass defects", Physical Review Applied **12**, 044027 (2019).

[31] M. Bückle, Y. S. Klaß, F. B. Nägele, R. Braive, and E. M. Weig, "Universal length dependence of tensile stress in nanomechanical string resonators", Physical Review Applied **15**, 034063 (2021).

[32] D. Hoch, X. Yao, and M. Poot, "Geometric tuning of stress in predisplaced silicon nitride resonators", Nano Letters **22**, 4013–4019 (2022).

[33] S. Schmid, K. Jensen, K. Nielsen, and A. Boisen, "Damping mechanisms in high-Q micro and nanomechanical string resonators", Physical Review B **84**, 165307 (2011).

[34] M. H. J. de Jong, M. A. ten Wolde, A. Cupertino, S. Gröblacher, P. G. Steeneken, and R. A. Norte, "Mechanical dissipation by substrate–mode coupling in sin resonators", Applied Physics Letters **121**, 032201 (2022).

[35] D. Shin, A. Cupertino, M. H. de Jong, P. G. Steeneken, M. A. Bessa, and R. A. Norte, "Spiderweb nanomechanical resonators via bayesian optimization: inspired by nature and guided by machine learning", Advanced Materials, 2106248.

[36] M. J. Bereyhi, A. Arabmoheghi, A. Beccari, S. A. Fedorov, G. Huang, T. J. Kippenberg, and N. J. Engelsen, "Perimeter modes of nanomechanical resonators exhibit quality factors exceeding 10^9 at room temperature", Physical Review X **12**, 021036 (2022).

[37] T. Manzaneque, M. K. Ghatkesar, F. Alijani, M. Xu, R. A. Norte, and P. G. Steeneken, "Resolution limits of resonant sensors with duffing non-linearity", arXiv preprint arXiv:2205.11903 (2022).

[38] W. C. Young, R. G. Budynas, A. M. Sadegh, et al., *Roark's formulas for stress and strain* (McGraw-hill New York, 1989).

[39] S. S. Rao, *Vibration of continuous systems* (John Wiley & Sons, 2019).

4

4

Strain Engineering of Nonlinear Nanoresonators from Hardening to Softening

Although strain engineering and soft-clamping techniques for attaining high Q-factors in nanoresonators have received much attention, their impact on nonlinear dynamics is not fully understood. In this study, we show that nonlinearity of high-Q Si_3N_4 nanomechanical string resonators can be substantially tuned by support design. Through careful engineering of support geometries, we control both stress and mechanical nonlinearities, effectively tuning nonlinear stiffness of two orders of magnitude. Our approach also allows control over the sign of the Duffing constant resulting in nonlinear softening of the mechanical mode that conventionally exhibits hardening behavior. We elucidate the influence of support design on the magnitude and trend of the nonlinearity using both analytical and finite element-based reduced-order models that validate our experimental findings. Our work provides evidence of the role of soft clamping on the nonlinear dynamic response of nanoresonators, offering an alternative pathway for nullifying or enhancing nonlinearity in a reproducible and passive manner.

Parts of this chapter have been published in *Communications Physics* **7**, 53 (2024) by Zichao Li, Minxing Xu, Richard A. Norte, Alejandro M. Aragón, Peter G. Steeneken, Farbod Alijani.

4.1. INTRODUCTION

High-Q nanomechanical resonators play a central role in sensing and enable ultra-small mass, acceleration, and force detection. Nonetheless, due to their nanoscale size and exceptional isolation from the surrounding environment, even minute forces, as small as a few piconewtons, can induce large-amplitude oscillations in them and result in a plethora of nonlinear phenomena that include bi-stability [1–4], parametric resonance [5–7], self-oscillations [8–10], and mode-coupling [11–14]. Many of these nonlinear phenomena can provide new information that is absent in the linear regime of operation. For instance, nonlinear resonances can be used to characterize nanomaterial properties [15, 16], enhance frequency stability [12, 17], or generate mechanical frequency combs [18, 19]. Some of these nonlinear phenomena have been engineered by leveraging the interplay between geometric and electrostatic nonlinearities [6, 20]. However, the introduction of external competing nonlinear forces may give rise to a series of unwanted side-effects, including noise [21, 22] or back-action effects [23] that can further complicate the nonlinear dynamic behavior, device fabrication and operation. Therefore, methodologies that can tailor the dynamic characteristics of nanomechanical devices solely through geometric design in the fabrication stage, are highly desirable.

Although numerous studies have already demonstrated the design optimization of resonance frequencies and Q-factor of nanomechanical resonators [24–29], the influence of geometric design on the nonlinear dynamics has been rarely investigated [11, 30, 31]. In this chapter, we show that soft-clamping techniques that are utilized to realize high-Q nanomechanical resonators, can also be engineered to tune nonlinear dynamics. By manipulating the support boundary in high-stress Si_3N_4 string resonators, we can tune the stress field and induce strong in-plane to out-of-plane coupling to simultaneously increase the Q-factor and the onset of nonlinearity over three times that of a doubly clamped string. Furthermore, by changing the support angle, we show that it is possible to engineer compressive forces in the softly clamped resonators and achieve buckled configurations in a controllable manner. These buckled states allow us to maximize geometric nonlinearity and change the response from hardening to softening. To understand the conditions required for strain engineering and buckling, we develop reduced-order models from finite element (FE) simulations, which highlight the role of the support angle in tuning the nonlinear dynamic response. Our results thus provide experimental evidence of controllable nonlinear dynamic engineering of nanomechanical resonators solely by geometric design, and paves the way for integrating arrays of highly tunable nonlinear nanodevices on a single chip [32–36].

4.2. NONLINEAR DYNAMIC CHARACTERIZATION

Fig. 4.1a shows a Scanning Electron Microscope (SEM) image of a nanomechanical resonator we fabricated with high-stress Si_3N_4 (see Section 2.1.1 in Chapter 2). The central string resonator of all studied devices had the same length ($L = 200\,\mu$m) and width ($w = 2\,\mu$m). However, the geometric parameters of the support beams, namely the support length L_s, the width w_s and the angle θ (see Fig. 4.1b), are varied to investigate their effect on the nonlinear response. The characterization of nonlinear dynamics in the nanomechanical string resonators can be found in Section 2.1.2 in Chapter 2.

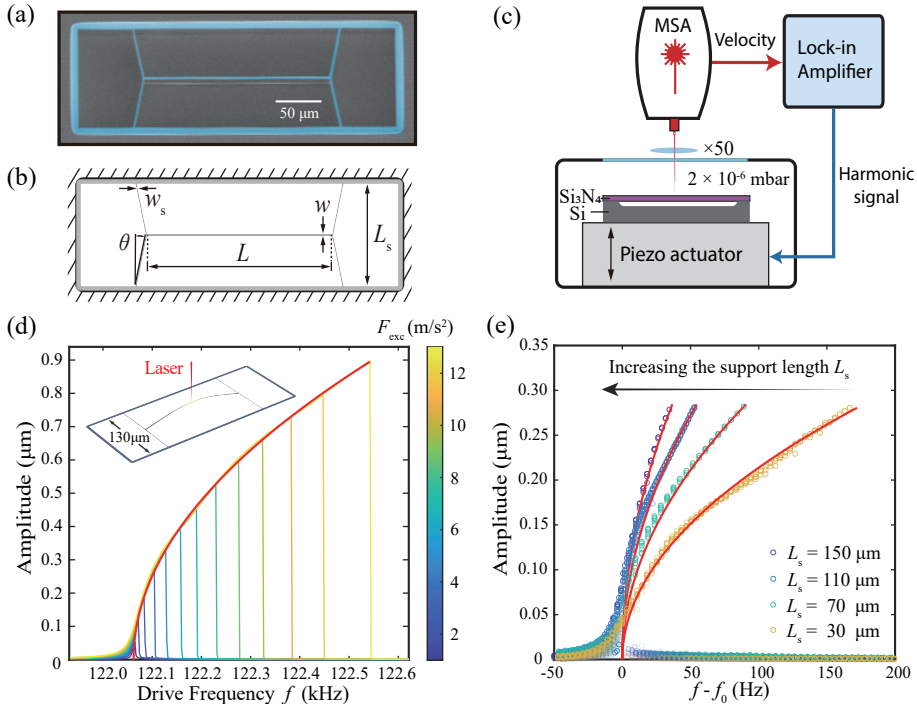

Figure 4.1: **Nonlinear dynamic characterization of string nanoresonators.** (a) Scanning electron microscope (SEM) image, colored in blue, of a string resonator with $L_s = 110\,\mu$m, $\theta = 0.2$ rad. (b) Illustration of design parameters. (c) Schematic of the measurement set-up comprising a Micro System Analyzer (MSA) Laser Doppler Vibrometer (LDV) for reading-out the motion and a piezo-actuator for generating the excitation force. (d) Duffing nonlinear response of the string resonator with $w_s = 1\,\mu$m, $L_s = 130\,\mu$m, and $\theta = 0$ as a function of the drive level. (e) Sensitivity of the Duffing response to the support length L_s for string resonators with $w_s = 1\,\mu$m and $\theta = 0$. The measurements are conducted on four string resonators with different L_s marked with different colors. The fitted backbone curves are shown in red and the fitted β values for $L_s = (30, 70, 110, 150)\,\mu$m are $\beta = (8.28, 2.12, 0.96, 0.62) \times 10^{22}\,\mathrm{m}^{-2}\mathrm{s}^{-2}$ respectively. The mass normalized excitation levels F_{exc} in (c) and (d) are indicated by the color scale.

To probe the geometric nonlinearity of our devices, we conduct frequency sweeps at different drive levels and measure the vibrations of the central string. Fig. 4.1d shows the frequency response at various drive levels for a device with $\theta = 0$. We note the presence of a hardening type nonlinearity at large amplitudes that arises from the elongation of the string during vibrations. To quantify the observed nonlinearity, we use the Duffing equation:

$$\ddot{q} + \mu\dot{q} + \alpha q + \beta q^3 = F_{\mathrm{exc}} \sin(2\pi f t). \tag{4.1}$$

where q is the displacement of the center of the string, $F_{\mathrm{exc}} \sin(2\pi f t)$ is the mass normalized harmonic drive force, $\alpha = (2\pi f_0)^2$, $\mu = 2\pi f_0/Q$ are the mass-normalized linear stiffness, damping coefficient, respectively. Furthermore, β is the Duffing constant that we extract by fitting the backbone of the experimental frequency response curves using

the expression: $f_{\max}^2 = f_0^2 + \frac{3}{16\pi^2}\beta A_{\max}^2$, where $f_{\max}$ is the drive frequency corresponding to the maximum amplitude $A_{\max}$ [37, 38] (see Section 2.1.2 in Chapter 2). In Fig. 4.1e we quantify the change in the Duffing constant β when varying the support length L_s with $\theta = 0$. We observe a factor 13 reduction in the extracted β when increasing the support length L_s from 30 µm to 150 µm. This is because long supports offer less rigidity to the in-plane motion, thus allowing the central string to relax when vibrating at large amplitudes, and consequently reducing the overall geometric nonlinearity.

4.3. THE INFLUENCE FROM SOFT CLAMPING

The reduction in the Duffing constant observed in Fig. 4.1e highlights the role of the in-plane stiffness on the geometric nonlinearity. Hence, to better understand the influence of support stiffness, we perform additional experiments on a large number of string resonators with different support length L_s and width w_s, and extract their Duffing constant β. Moreover, we develop a simplified model consisting of a string connected to in-plane springs at both ends, denoted as k_{in} (see Fig. 4.2a), to quantitatively capture the influence of L_s and w_s on k_{in} and thus on β when $\theta = 0$. We particularly model the boundary springs as doubly clamped beams with pre-tension $\sigma_0 = 1.06$GPa and use their central deflection to analytically estimate k_{in} as follows (see Section 2.2.1 in Chapter 2 for details):

$$\begin{aligned} k_{in} &= \left(k_{Ei}^{-1} + k_{si}^{-1}\right)^{-1} + k_{\sigma i} \\ &= \left[\left(\frac{16Ehw_s^3}{L_s^3}\right)^{-1} + \left(\frac{2Ehw_s}{(1+\nu)\eta L_s}\right)^{-1}\right]^{-1} + \frac{4\sigma_0 hw_s}{L_s}, \end{aligned} \tag{4.2}$$

where k_{Ei} is the bending stiffness, k_{si} is the shear stiffness, $k_{\sigma i}$ is the additional contribution from the pre-tension. Moreover, η is a geometric factor related to shear effects in deep beams with a high depth-to-span ratio. For a rectangular cross section, its value is $\eta = 1.2$ [39]. In contrast to the central part that is assumed to be a vibrating string, the support beam is modeled as a moderately deep beam ($w_s/h \geq 2.94$), for estimating k_{in}. To validate our analytical estimation of the in-plane stiffness k_{in}, we also obtained it numerically using FE simulations. The analytical (lines) and the FE (circles) results in Fig. 4.2b closely match one another and confirm our earlier prediction that wider and shorter support beams offer more rigidity against the deflection, particularly in the in-plane direction. Next, to capture the effect of in-plane springs on the in-plane to out-of-place coupling and thus nonlinear dynamics, we obtain the Lagrangian $\mathscr{L} = T - U_s - U_k$, where T is the kinetic energy of the string, U_s and U_k are the potential energy of the string and the two springs k_{in}, respectively, and use Lagrange equations to obtain the updated α and β as follows (see Section 2.2.2 in Chapter 2 for details):

$$\alpha = \frac{k_1}{m_{eff}} = \frac{\pi^2(1-\nu)\sigma_0}{\rho L^2}\left(1 + \frac{2EA}{k_{in}L}\right)^{-1}, \tag{4.3}$$

$$\beta = \frac{k_3}{m_{eff}} = \frac{\pi^4 E}{4\rho L^4}\left(1 + \frac{2EA}{k_{in}L}\right)^{-1}, \tag{4.4}$$

where k_1 and k_3 are the linear stiffness and the Duffing constant before mass normalization respectively, $m_{\text{eff}} = \rho AL/2$ is the effective mass and $A = hw$ is the area of the string's cross section. It is worth noting that $(1+2EA/k_{\text{in}}L)^{-1}$ serves as a tuning factor introduced by the finite in-plane stiffness k_{in}, which changes both α and β of a doubly clamped string with stress in the same rate. The effect of k_{in} on the nonlinear stiffness can intuitively be understood by realizing that the geometric nonlinear stiffness of a string resonator is due to the increase of average string length and the resulting tension proportional to q^2. If the clamping at the ends of the string is weakened by reducing the value of springs k_{in}, then the tension increase for the same length increase will be less, such that the nonlinear stiffness β will reduce, as shown by Eq. (4.4).

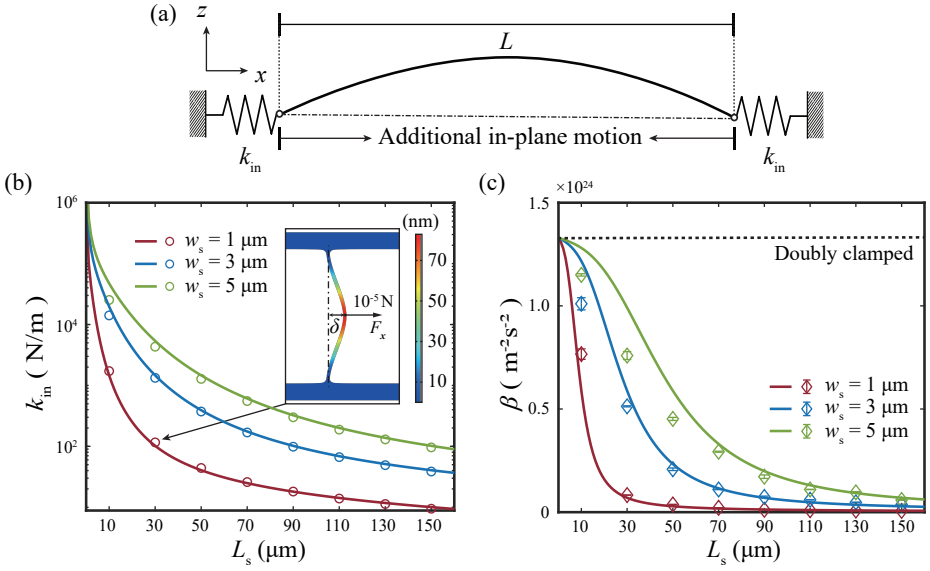

Figure 4.2: **Influence of in-plane stiffness on the geometric nonlinearity of string resonators.** (a) Simplified model of a string vibrating in the out-of-plane direction, denoted as z, with finite in-plane stiffness k_{in}. (b) Analytical (solid lines) and Finite element (FE) based (circles and inset) results of the in-plane stiffness k_{in} for a support beam with varying L_{s} and w_{s}. (c) Analytical (solid lines) and measured (diamonds) β of a string resonator with varying L_{s} and w_{s} corresponding to (b). The dashed line shows the analytical estimation of β for a doubly clamped string resonator.

In Fig. 4.2c we show the extracted Duffing constant β from experiments via fitting the backbone curves of the frequency responses and compare those to the analytical model predictions from Eq. (4.4). From Fig. 4.2b and c, it is apparent that the variation in β matches the model quite well. We shall note that for the tested device with the slenderest support ($L_{\text{s}} = 150\,\mu\text{m}$, $w_{\text{s}} = 1\,\mu\text{m}$) and the central string stress of 5.08 MPa, the analytically derived $f_0 = 94\,\text{kHz}$ and $\beta = 7.21\times10^{21}\,\text{m}^{-2}\text{s}^{-2}$ compare well with the measured counterparts $f_0 = 103\,\text{kHz}$ and $\beta = 6.20\times10^{21}\,\text{m}^{-2}\text{s}^{-2}$. Therefore, the assumptions of having high-stress strings with sinusoidal eigenmode are valid for obtaining the analytical expressions in case of $\theta = 0$. By comparing the dashed line to the experimental values in Fig. 4.2c, it can be seen that the geometric nonlinearity β can be reduced by up

to two orders of magnitude using the presented support design. This substantial reduction in geometric nonlinearity highlights the role of support design in tailoring nonlinear dynamic behaviors in nanomechanical resonators with soft-clamping. It is also noteworthy that the β calculated by using the simplified model converges to the value of a doubly clamped string ($1.33\times10^{24}\,\mathrm{m^{-2}s^{-2}}$) when the support length L_s tends to zero (k_{in} approaches infinity in Eq. (4.4)), thus further confirming our model. However, in case of wider and shorter supports, we notice that the simplified model deviates from the measurements. We attribute this to the fact that the dimensions of the supports become comparable to the underetch distance of the Si_3N_4 ($\sim 5\,\mu m$) such that the assumptions used for the derivation of Eq. (4.2) might not be valid anymore.

4.4. ENGINEERING THE NONLINEARITY FROM HARDENING TO BUCKLING-INDUCED SOFTENING

To gain deeper understanding of the full potential of support design on nonlinear dynamics, we also look into the influence of the support angle θ on the nonlinear frequency response curves. By changing θ from positive to negative, we are able to tune the tilting direction of the backbone curves around the resonance, from the common hardening nonlinearity to softening (see Fig. 4.3a). To understand the physical mechanism behind this observation, we use Keyence Digital Microscope VHX-6000 to focus at the middle of central string and the unreleased Si_3N_4 layer to measure the difference H of their focal heights, as shown in Fig. 4.3b. We note a maximum deviation of $H = 22.17\,\mu m$ for the device with $L_s = 150\,\mu m$ and $\theta = -0.1$ rad, which suggests the presence of broken-symmetry in nanomechanical resonators with $\theta < 0$. We attribute this to a change of built-in stress in the Si_3N_4 resonator from tension to compression, which upon surpassing the buckling bifurcation point, breaks the out-of-plane symmetry and yields a buckled configuration (see SEM image in Fig. 4.3b). To verify these observations, we simulate the buckled resonator response by nonlinear reduced-order modeling of full FE models [40] and numerical continuation [41] (see Section 2.2.3 in Chapter 2), which had been successfully applied to model the nonlinear dynamics of graphene drums [40]. It is worth mentioning that for a buckled string, the maximum amplitude does not always occur at the center of its first out-of-plane symmetric mode. Accordingly, we use FE simulations to obtain the amplitude ratio between the center of the mode and where it has the maximum amplitude, thus scaling the measured amplitudes at the center. The simulated results are shown as solid curves in Fig. 4.3a and demonstrate that the buckled configurations can account for the experimentally observed softening response (see Section 2.2.3 in Chapter 2) [42].

To further investigate the role of the support angle θ on the tunability of the dynamical properties, we perform additional measurements on string resonators with values of θ ranging from -0.5 rad to 0.5 rad, while keeping $L_s = 150\,\mu m$ and $w_s = 1\,\mu m$ constant. In Fig. 4.4 we show the variation of the resonance frequency f_0, Q-factor, and Duffing constant β of the first symmetric out-of-plane mode as a function of θ. We note that supports with positive θ significantly increase the values of the dynamical parameters shown in Fig. 4.4. This is attributed to a higher k_{in} that results in a higher tension, and thus translates into higher values of f_0, Q-factor and the Duffing constant β (see

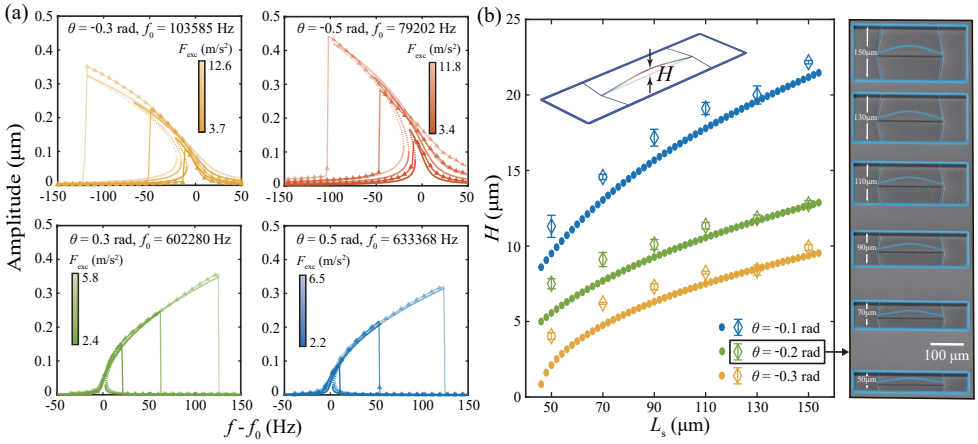

Figure 4.3: **Influence of support angle θ on the geometric nonlinearity.** (a) Finite element (FE) based (bold lines) and experimentally measured (triangles) frequency response curves of resonators with $w_s = 1\,\mu m$ and $L_s = 150\,\mu m$, showcasing the shifting between hardening and softening induced by the support angle θ. The solid parts of bold lines represent the stable branch of the simulated response while the dotted parts are unstable. The legends show the mass-normalized drive level. The fitted β values for $\theta = (-0.3, -0.5)$rad are $\beta = (-0.56,\ -0.27)\times 10^{22}\,m^{-2}s^{-2}$. For $\theta = (0.3, 0.5)$rad the Duffing constant $\beta = (7.00,\ 9.01)\times 10^{22}\,m^{-2}s^{-2}$. (b) Finite element (FE) based results (dots) and measurements (diamonds) of the buckling induced static displacement height H of the string at its center with $w_s = 1\,\mu m$ for different support angles θ and lengths L_s. The inset shows the SEM image, colored in blue, of an array of buckled string resonator with $w_s = 1\,\mu m$, $\theta = -0.2$ rad and different L_s from $150\,\mu m$ to $50\,\mu m$.

Eq. (4.4)). The most intriguing observation, however, lies in the region where the devices transition near $\theta = 0$ from a flat configuration to the buckled state. Here, we notice a sudden increase in the resonance frequency and the maximum $|\beta|$ of our devices which is due to the large offset from the flat state (See Fig. 4.4a, c). By reducing θ towards -0.5 rad, however, the post-buckling offset is found to decrease again, and subsequently both f_0 and $|\beta|$ decrease monotonically. We noticed that near $\theta = 0$, the Q-factor of our devices drops to a similar level to that of stress-free string resonators [43], whose dissipation dilution disappears with the relaxation of high tension (see Fig. 4.4b) [27, 29]. We however note that the FE-simulated Q-factor of devices close to the onset of buckling are lower than the intrinsic Q-factor $Q_0 = 9864$. This could be attributed to the anti-spring behavior of the buckled strings that can result in $U_{total}/U_{bending} < 1$ and thus $Q < Q_0$ [29, 44]. Included in Fig. 4.4c, we compare experimental data to numerical results from reduced-order modeling of FE simulations that offer a higher θ resolution than experiments. The simulations (dots) are in good agreement with our experiments, except around $\theta = -0.1$ rad, where we faced numerical instability. We shall note that the simulations were conducted after a careful convergence study of the corresponding multi-mode reduced-order model, that also accounted for the broken-symmetry induced by buckling. Furthermore, all the simulated results in Fig. 4.4 were obtained using the same material and geometric properties, and θ is the only parameter that is changed. The agreement between experiments and simulations is evident for the reliability of the modelling approach.

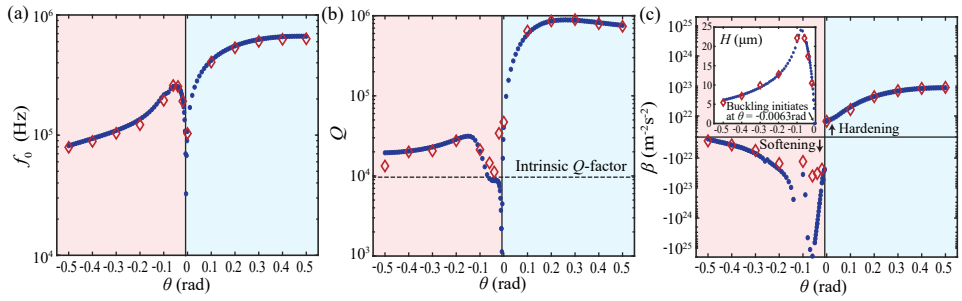

Figure 4.4: **Tuning of the resonance frequency, Q-factor and the effective geometric nonlinearity by varying support angles.** Finite element (FE)-based (dots) and measured (diamonds) (a) resonance frequencies f_0, (b) Q-factors, and (c) geometric nonlinearity β of the first symmetric out-of-plane mode; note that the error bars are smaller than the data marker size. The presented resonators share $L = 200\,\mu$m, $w = 2\,\mu$m, $w_s = 1\,\mu$m, and $L_s = 150\,\mu$m but different support angles θ, which vary from -0.5 rad to 0.5 rad. The height of string center H is shown in (c) for negative θ.

4

4.5. CONCLUSION

The large tunability of the dynamical properties provided by geometric design offers new possibilities for engineering devices that are linear over a large range. For instance, as shown in Fig. 4.4, for devices with $\theta > 0$, it is possible to substantially decrease the geometric nonlinearity while maintaining a high Q-factor and thus expand the linear dynamic range of the resonator by increasing the onset of nonlinearity $a_{1\mathrm{dB}} \propto Q^{-\frac{1}{2}} \alpha^{\frac{1}{2}} \beta^{-\frac{1}{2}}$ [45, 46]. As an example, in devices with support angle θ around 0.1 rad, we note that both $a_{1\mathrm{dB}}$ and Q-factor are three times higher than in conventional doubly clamped strings (see Appendix Section 4.6.1). The methodology also provides the possibility to minimize β, such that it is infinitely small. We expect this condition to occur around $\theta = -0.0063$ rad according to FE simulations, where a transition from hardening to softening is observed. This condition is associated with the onset of buckling bifurcation when θ is varied, which is unstable and challenging to control, yet potentially possible to be stabilized by using external forces [1]. On the other hand, it is desirable to operate devices in the nonlinear regime by squeezing the dynamic range (DR) of nanomechanical resonators (defined as the ratio $\mathrm{DR} = 20\lg(a_{1\mathrm{dB}}/a_{\mathrm{th}})$, where a_{th} is the thermomechanical noise floor). Notably, in our current designs we observe a reduction of DR from 64dB in a double clamped string, to 51dB in devices with slender supports. We foresee that by reducing the thickness $h = 340$ nm of our devices, DR can be further minimized (see Appendix Section 4.6.2), enabling the study of nonlinear dynamics in the Brownian limit [47]. Moreover, recent studies have shown that by enhancing the ratio β/α, it is possible to realize nonlinear nanomechanical resonators that approach the quantum ground state in doubly clamped carbon nanotubes [48]. Our simulations suggest that the absolute ratio of β/α in buckled resonators can be increased to an order of magnitude higher than that of double clamped ones, suggesting that buckling can be used as an effective tool for increasing nonlinearities in modes that operate close to the quantum ground state [49].

4.6. APPENDIX

4.6.1. TUNABILITY OF a_{1dB}, a_{th} AND DR

Using FE simulations and the reduced-order modeling, we perform a parametric study on resonance frequency, Q-factor [29] and the Duffing constant and show the results in Figs. 4.5a, b and c. It is obvious that all these three parameters could be tuned in a wide range by changing L_s and θ of support beams, which work effectively as knobs to tune the dynamics of the resonator with relatively small space occupation and high robustness. It is worth noting that Q-factor doesn't change monotonically with either L_s or θ. For relatively small L_s and θ, Q-factor will drop with increasing L_s. While for longer support beams, there is always a maximum region of Q-factor, which corresponds to a moderately tilted support angle θ. Here we only focus on devices with $\theta \geq 0$ because of their high Q-factor and similarity to string resonators.

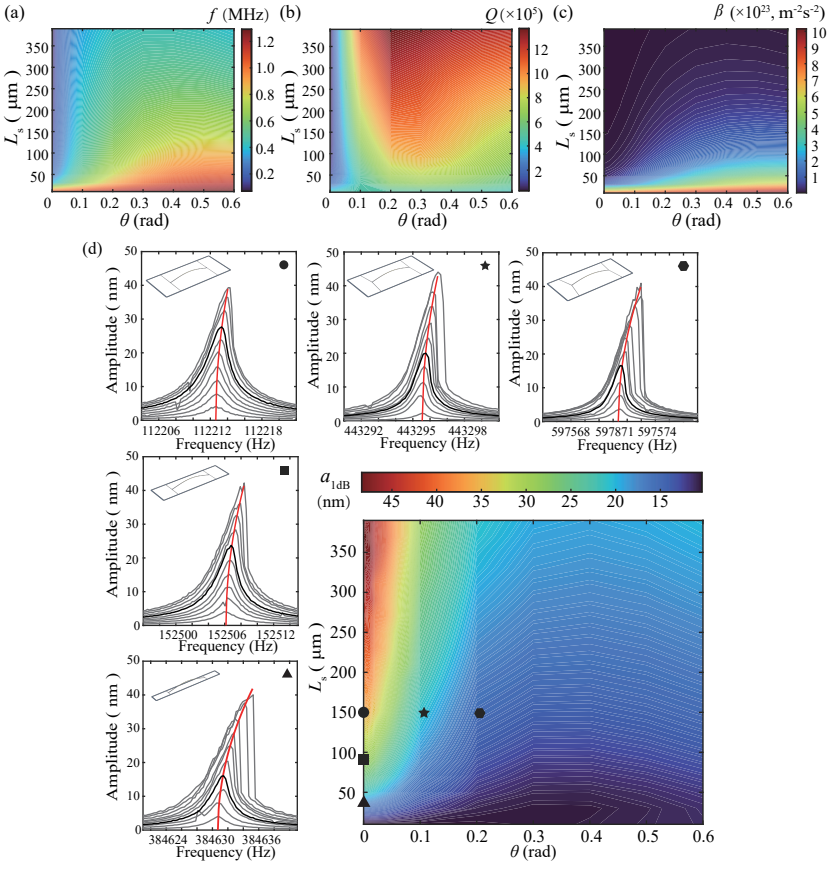

Figure 4.5: **Tuning dynamical parameters by engineering the supports of string resonators.** FE simulation of (a) fundamental resonance frequency, (b) Q-factor, (c) the Duffing constant β and (d) the onset of nonlinearity a_{1dB} by varying support design of string resonators with $L = 200\,\mu m$, $w = 2\,\mu m$. Five cases are selected to show the measurement of a_{1dB}, where the response curve with closest maximum amplitude compared to a_{1dB} of each case is bolded.

Based on dynamical parameters shown in Figs. 4.5a, b and c, we look further into the onset of nonlinearity $a_{1\mathrm{dB}}$ in our resonators, which can be expressed in terms of the Q-factor and the ratio between the linear stiffness α and the Duffing constant (nonlinear stiffness) β [45]:

$$a_{1\mathrm{dB}} = 0.9244\sqrt{\frac{\alpha}{Q\beta}}. \tag{4.5}$$

We find that support design offers a wide range of tunability along with high fidelity compared to the measurement (see for instance Fig. 4.5d).

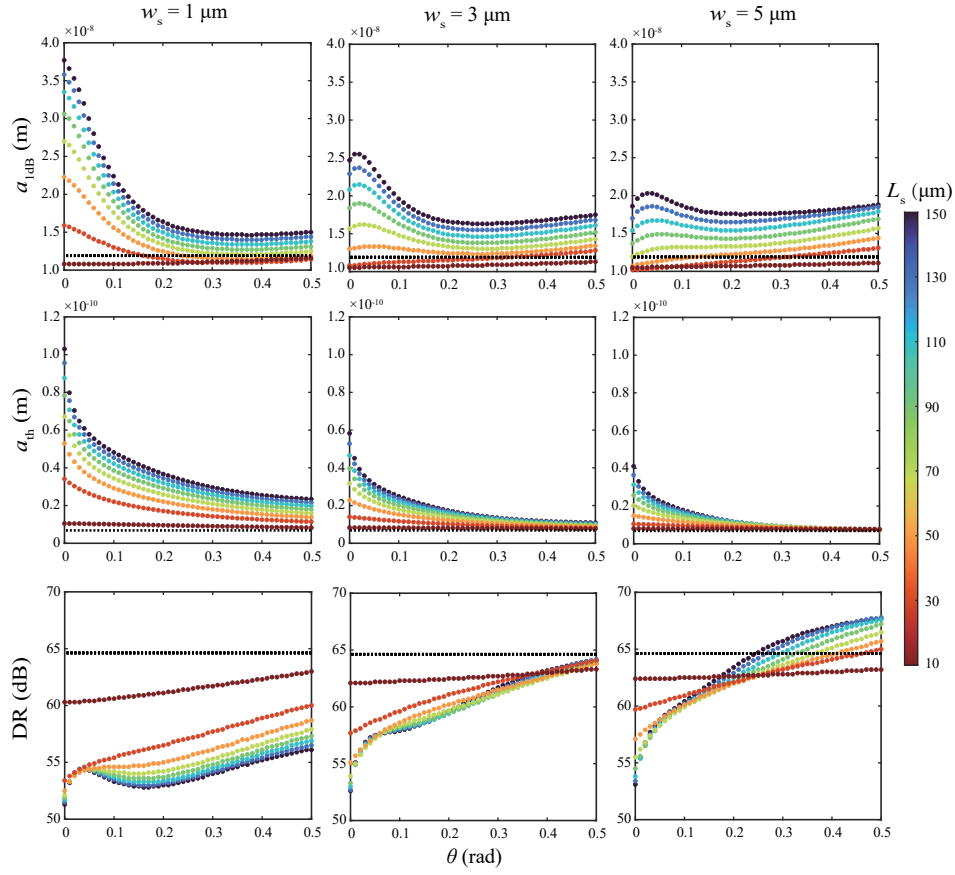

Figure 4.6: The FE-simulated results (colored dots) of the onset of nonlinearity $a_{1\mathrm{dB}}$, thermomechanical noise a_{th} and dynamic range DR of strings with $L = 200\,\mu\mathrm{m}$, $w = 2\,\mu\mathrm{m}$ and three different w_s values while varying L_s and θ. The corresponding values of a doubly clamped string with $L = 200\,\mu\mathrm{m}$ and $w = 2\,\mu\mathrm{m}$ are plotted as black dotted lines for benchmark, respectively.

We also investigate the influence of geometric design on the dynamic range DR, which is defined as the ratio between the onset of nonlinearity $a_{1\mathrm{dB}}$ and the thermomechanical noise a_{th} [45]:

$$\begin{aligned} \mathrm{DR} &= 20\lg\frac{a_{1\mathrm{dB}}}{a_{\mathrm{th}}} \\ &= 20\lg\frac{0.9244\sqrt{\dfrac{\alpha}{Q\beta}}}{\sqrt{\dfrac{4k_{\mathrm{B}}TQ\Delta f}{m_{\mathrm{eff}}\alpha^{\frac{3}{2}}}}} \\ &= 20\lg\left[0.4622\left(k_{\mathrm{B}}T\Delta f\right)^{-\frac{1}{2}} m_{\mathrm{eff}}^{\frac{1}{2}} Q^{-1}\alpha^{\frac{5}{4}}\beta^{-\frac{1}{2}}\right], \end{aligned} \tag{4.6}$$

where k_{B} is the Boltzmann's constant, T (298K) is the room temperature, Δf (1Hz) is the measurement bandwidth and m_{eff} is the effective mass of the driven mode. In Fig. 4.6, we demonstrate the FE-simulated $a_{1\mathrm{dB}}$, a_{th} and DR of a string resonator with $L = 200\,\mu\mathrm{m}$ and $w = 2\,\mu\mathrm{m}$ against varying support angles θ as well as different support length L_{s} and width w_{s}. The corresponding values of the doubly clamped string without soft-clamping supports are shown as black dotted lines in Fig. 4.6. In most of the situations, the soft-clamping supports increase the onset of nonlinearity $a_{1\mathrm{dB}}$ and the thermomechanical noise a_{th} at the same time, as a combined result of the increased Q-factor and decreased Duffing constant β.

As demonstrated by the FE simulations in Fig. 4.6 and Fig. 4.7, by reducing the thickness h of our resonators from 340 nm to 20 nm, we can observe a squeezing of DR by 5.5 times, i.e., a reduction of $a_{1\mathrm{dB}}/a_{\mathrm{th}}$ ratio by 450 times. We find an obvious drop in DR of string resonators with supports compared to doubly clamped ones (dotted lines). The squeezing effect for different L_{s} is distinct close to $\theta = 0$ while it saturates as θ and L_{s} become larger. In conclusion, both the small thickness and soft-clamping supports contribute to the realization of thermally driven nonlinear nanomechanical resonators at room temperature.

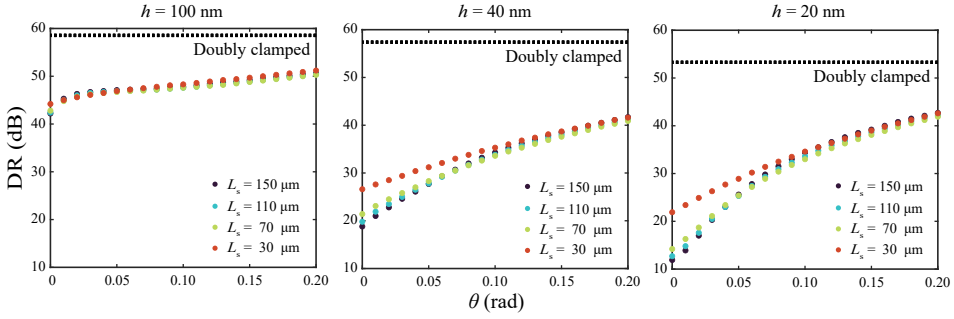

Figure 4.7: The FE-simulated results (colored dots) of the dynamic range DR of strings with $L = 200\,\mu\mathrm{m}$, $w = 2\,\mu\mathrm{m}$, $w_{\mathrm{s}} = 1\,\mu\mathrm{m}$ and three different thickness h values while varying L_{s} and θ. The values of a doubly clamped string with $L = 200\,\mu\mathrm{m}$, $w = 2\,\mu\mathrm{m}$ and corresponding h values are plotted as black dotted lines for benchmark, respectively.

BIBLIOGRAPHY

[1] S. O. Erbil, U. Hatipoglu, C. Yanik, M. Ghavami, A. B. Ari, M. Yuksel, and M. S. Hanay, "Full electrostatic control of nanomechanical buckling", Physical Review Letters **124**, 046101 (2020).

[2] M. Yuksel, E. Orhan, C. Yanik, A. B. Ari, A. Demir, and M. S. Hanay, "Nonlinear nanomechanical mass spectrometry at the single-nanoparticle level", Nano Letters **19**, 3583–3589 (2019).

[3] H. Okamoto, I. Mahboob, K. Onomitsu, and H. Yamaguchi, "Rapid switching in high-Q mechanical resonators", Applied Physics Letters **105**, 083114 (2014).

[4] F. Bayram, D. Gajula, D. Khan, and G. Koley, "Mechanical memory operations in piezotransistive GaN microcantilevers using au nanoparticle-enhanced photoacoustic excitation", Microsystems & Nanoengineering **8**, 1–14 (2022).

[5] H. Okamoto, I. Mahboob, K. Onomitsu, and H. Yamaguchi, "Rapid switching in high-q mechanical resonators", Applied Physics Letters **105**, 083114 (2014).

[6] A. Keşkekler, O. Shoshani, M. Lee, H. S. van der Zant, P. G. Steeneken, and F. Alijani, "Tuning nonlinear damping in graphene nanoresonators by parametric–direct internal resonance", Nature communications **12**, 1–7 (2021).

[7] J. S. Huber, G. Rastelli, M. J. Seitner, J. Kölbl, W. Belzig, M. I. Dykman, and E. M. Weig, "Spectral evidence of squeezing of a weakly damped driven nanomechanical mode", Physical Review X **10**, 021066 (2020).

[8] L. Villanueva, E. Kenig, R. Karabalin, M. Matheny, R. Lifshitz, M. Cross, and M. Roukes, "Surpassing fundamental limits of oscillators using nonlinear resonators", Physical Review Letters **110**, 177208 (2013).

[9] C. Chen, D. H. Zanette, J. R. Guest, D. A. Czaplewski, and D. López, "Self-sustained micromechanical oscillator with linear feedback", Physical Review Letters **117**, 017203 (2016).

[10] J. M. Miller, A. Gomez-Franco, D. D. Shin, H.-K. Kwon, and T. W. Kenny, "Amplitude stabilization of micromechanical oscillators using engineered nonlinearity", Physical Review Research **3**, 033268 (2021).

[11] S. Dou, B. S. Strachan, S. W. Shaw, and J. S. Jensen, "Structural optimization for nonlinear dynamic response", Philosophical Transactions of the Royal Society A: Mathematical, Physical and Engineering Sciences **373**, 20140408 (2015).

[12] D. Antonio, D. H. Zanette, and D. López, "Frequency stabilization in nonlinear micromechanical oscillators", Nature Communications **3**, 1–6 (2012).

[13] C. Chen, D. H. Zanette, D. A. Czaplewski, S. Shaw, and D. López, "Direct observation of coherent energy transfer in nonlinear micromechanical oscillators", Nature Communications **8**, 1–7 (2017).

[14] J. Güttinger, A. Noury, P. Weber, A. M. Eriksson, C. Lagoin, J. Moser, C. Eichler, A. Wallraff, A. Isacsson, and A. Bachtold, "Energy-dependent path of dissipation in nanomechanical resonators", Nature Nanotechnology **12**, 631–636 (2017).

[15] D. Davidovikj, F. Alijani, S. J. Cartamil-Bueno, H. S. van der Zant, M. Amabili, and P. G. Steeneken, "Nonlinear dynamic characterization of two-dimensional materials", Nature Communications **8**, 1253 (2017).

[16] P. G. Steeneken, R. J. Dolleman, D. Davidovikj, F. Alijani, and H. S. van der Zant, "Dynamics of 2d material membranes", 2D Materials **8**, 042001 (2021).

[17] L. Huang, S. Soskin, I. Khovanov, R. Mannella, K. Ninios, and H. B. Chan, "Frequency stabilization and noise-induced spectral narrowing in resonators with zero dispersion", Nature Communications **10**, 1–10 (2019).

[18] A. Keskekler, H. Arjmandi-Tash, P. G. Steeneken, and F. Alijani, "Symmetry-breaking-induced frequency combs in graphene resonators", Nano Letters **22**, 6048–6054 (2022).

[19] D. A. Czaplewski, C. Chen, D. Lopez, O. Shoshani, A. M. Eriksson, S. Strachan, and S. W. Shaw, "Bifurcation generated mechanical frequency comb", Physical Review Letters **121**, 244302 (2018).

[20] C. Samanta, N. Arora, and A. Naik, "Tuning of geometric nonlinearity in ultrathin nanoelectromechanical systems", Applied Physics Letters **113**, 113101 (2018).

[21] M. Sansa, E. Sage, E. C. Bullard, M. Gély, T. Alava, E. Colinet, A. K. Naik, L. G. Villanueva, L. Duraffourg, M. L. Roukes, et al., "Frequency fluctuations in silicon nanoresonators", Nature Nanotechnology **11**, 552–558 (2016).

[22] L. G. Villanueva, R. B. Karabalin, M. H. Matheny, E. Kenig, M. C. Cross, and M. L. Roukes, "A nanoscale parametric feedback oscillator", Nano Letters **11**, 5054–5059 (2011).

[23] C. Urgell, W. Yang, S. L. De Bonis, C. Samanta, M. J. Esplandiu, Q. Dong, Y. Jin, and A. Bachtold, "Cooling and self-oscillation in a nanotube electromechanical resonator", Nature Physics **16**, 32–37 (2020).

[24] Y. Seis, T. Capelle, E. Langman, S. Saarinen, E. Planz, and A. Schliesser, "Ground state cooling of an ultracoherent electromechanical system", Nature Communications **13**, 1507 (2022).

[25] P. Sadeghi, M. Tanzer, S. L. Christensen, and S. Schmid, "Influence of clamp-widening on the quality factor of nanomechanical silicon nitride resonators", Journal of Applied Physics **126**, 165108 (2019).

[26] S. A. Fedorov, A. Beccari, N. J. Engelsen, and T. J. Kippenberg, "Fractal-like mechanical resonators with a soft-clamped fundamental mode", Physical Review Letters **124**, 025502 (2020).

[27] D. Shin, A. Cupertino, M. H. de Jong, P. G. Steeneken, M. A. Bessa, and R. A. Norte, "Spiderweb nanomechanical resonators via bayesian optimization: inspired by nature and guided by machine learning", Advanced Materials, 2106248.

[28] D. Hoch, X. Yao, and M. Poot, "Geometric tuning of stress in predisplaced silicon nitride resonators", Nano Letters **22**, 4013–4019 (2022).

[29] Z. Li, M. Xu, R. A. Norte, A. M. Aragón, F. van Keulen, F. Alijani, and P. G. Steeneken, "Tuning the Q-factor of nanomechanical string resonators by torsion support design", Applied Physics Letters **122**, 013501 (2023).

[30] L. L. Li, P. M. Polunin, S. Dou, O. Shoshani, B. Scott Strachan, J. S. Jensen, S. W. Shaw, and K. L. Turner, "Tailoring the nonlinear response of mems resonators using shape optimization", Applied Physics Letters **110**, 081902 (2017).

[31] H. Cho, B. Jeong, M.-F. Yu, A. F. Vakakis, D. M. McFarland, and L. A. Bergman, "Nonlinear hardening and softening resonances in micromechanical cantilever-nanotube systems originated from nanoscale geometric nonlinearities", International Journal of Solids and Structures **49**, 2059–2065 (2012).

[32] J. Doster, T. Shah, T. Fösel, P. Paulitschke, F. Marquardt, and E. M. Weig, "Observing polarization patterns in the collective motion of nanomechanical arrays", Nature Communications **13**, 2478 (2022).

[33] D. Hatanaka, I. Mahboob, K. Onomitsu, and H. Yamaguchi, "Phonon waveguides for electromechanical circuits", Nature Nanotechnology **9**, 520–524 (2014).

[34] M. Bagheri, M. Poot, L. Fan, F. Marquardt, and H. X. Tang, "Photonic cavity synchronization of nanomechanical oscillators", Physical Review Letters **111**, 213902 (2013).

[35] M. H. Matheny, M. Grau, L. G. Villanueva, R. B. Karabalin, M. Cross, and M. L. Roukes, "Phase synchronization of two anharmonic nanomechanical oscillators", Physical Review Letters **112**, 014101 (2014).

[36] J. Liu, G. Huang, R. N. Wang, J. He, A. S. Raja, T. Liu, N. J. Engelsen, and T. J. Kippenberg, "High-yield, wafer-scale fabrication of ultralow-loss, dispersion-engineered silicon nitride photonic circuits", Nature Communications **12**, 2236 (2021).

[37] A. H. Nayfeh and D. T. Mook, *Nonlinear oscillations* (John Wiley & Sons, 2008).

[38] S. Schmid, L. G. Villanueva, and M. L. Roukes, *Fundamentals of nanomechanical resonators*, Vol. 49 (Springer, 2016).

[39] W. C. Young, R. G. Budynas, A. M. Sadegh, et al., *Roark's formulas for stress and strain* (McGraw-hill New York, 1989).

[40] A. Keşkekler, V. Bos, A. M. Aragón, P. G. Steeneken, and F. Alijani, *Characterizing multimode nonlinear dynamics of nanomechanical resonators*, 2023.

[41] A. Dhooge, W. Govaerts, Y. A. Kuznetsov, H. G. E. Meijer, and B. Sautois, "New features of the software matcont for bifurcation analysis of dynamical systems", Mathematical and Computer Modelling of Dynamical Systems **14**, 147–175 (2008).

[42] W. Lacarbonara, A. H. Nayfeh, and W. Kreider, "Experimental validation of reduction methods for nonlinear vibrations of distributed-parameter systems: analysis of a buckled beam", Nonlinear Dynamics **17**, 95–117 (1998).

[43] L. G. Villanueva and S. Schmid, "Evidence of surface loss as ubiquitous limiting damping mechanism in SiN micro-and nanomechanical resonators", Physical Review Letters **113**, 227201 (2014).

[44] D. M. Dykstra, C. Lenting, A. Masurier, and C. Coulais, "Buckling metamaterials for extreme vibration damping", Advanced Materials **35**, 2301747 (2023).

[45] H. C. Postma, I. Kozinsky, A. Husain, and M. Roukes, "Dynamic range of nanotube- and nanowire-based electromechanical systems", Applied Physics Letters **86**, 223105 (2005).

[46] J. Molina, J. E. Escobar, D. Ramos, E. Gil-Santos, J. J. Ruz, J. Tamayo, Á. San Paulo, and M. Calleja, "High dynamic range nanowire resonators", Nano Letters **21**, 6617–6624 (2021).

[47] A. W. Barnard, M. Zhang, G. S. Wiederhecker, M. Lipson, and P. L. McEuen, "Real-time vibrations of a carbon nanotube", Nature **566**, 89–93 (2019).

[48] C. Samanta, S. De Bonis, C. Møller, R. Tormo-Queralt, W. Yang, C. Urgell, B. Stamenic, B. Thibeault, Y. Jin, D. Czaplewski, et al., "Nonlinear nanomechanical resonators approaching the quantum ground state", Nature Physics, 1–5 (2023).

[49] R. M. Geilhufe, "Quantum buckling in metal–organic framework materials", Nano Letters **21**, 10341–10345 (2021).

5

5

Finite Element-based Nonlinear Dynamic Optimization of Nanomechanical Resonators

Nonlinear dynamic simulations of mechanical resonators have been facilitated by the advent of computational techniques that generate nonlinear reduced order models (ROMs) using the finite element (FE) method. However, designing devices with specific nonlinear characteristics remains inefficient since it requires manual adjustment of the design parameters and can result in suboptimal designs. Here, we integrate an FE-based nonlinear ROM technique with a derivative-free optimization algorithm to enable the design of nonlinear mechanical resonators. The resulting methodology is used to optimize the support design of high-stress nanomechanical Si_3N_4 string resonators, in the presence of conflicting objectives such as simultaneous enhancement of Q-factor and nonlinear Duffing constant. To that end, we generate Pareto frontiers that highlight the trade-offs between optimization objectives and validate the results both numerically and experimentally. To further demonstrate the capability of multi-objective optimization for practical design challenges, we simultaneously optimize the design of nanoresonators for three key figure-of-merits in resonant sensing: power consumption, sensitivity and response time. The presented methodology can facilitate and accelerate designing (nano)mechanical resonators with optimized performance for a wide variety of applications.

Parts of this chapter have been published in *Microsystems & Nanoengineering* **11**, 16 (2025) by Zichao Li, Farbod Alijani, Ali Sarafraz, Minxing Xu, Richard A. Norte, Alejandro M. Aragón, Peter G. Steeneken.

5.1. INTRODUCTION

Design of mechanical structures that move or vibrate in a predictable and desirable manner is a central challenge in many engineering disciplines. This task becomes more complicated when these structures experience large-amplitude vibrations, since linear analysis methods fail and nonlinear effects need to be accounted for. This is particularly important at the nanoscale, where forces on the order of only a few pN can already yield a wealth of nonlinear dynamic phenomena worth exploiting [1–5].

Although design optimization of micro and nanomechanical resonators in the linear regime is well-established [6], the use of design optimization for engineering nonlinear resonances has received less attention [7]. This is because designers tend to avoid the nonlinear regime, and optimizing structures' nonlinear dynamics is more complex, which requires extensive computational resources. As a result, available literature on nonlinear dynamic optimization is limited, although some recent advances have been made that combine analytical methods with gradient-based shape optimization, to optimize nonlinearities in micro beams [8, 9]. For nonlinear modeling of more complex structures, several approaches have been developed based on nonlinear reduced order modeling (ROM) of finite element (FE) simulations [10–12]. A particularly attractive class known as STEP (STiffness Evaluation Procedure) [13] can determine nonlinear coefficients of an arbitrary mechanical structure and can be implemented in virtually any commercial finite element method (FEM) package. This, for instance, has been recently shown by using COMSOL to model the nonlinear dynamics of high-stress Si_3N_4 string [14] as well as graphene nanoresonators [15]. Since the number of degrees of freedom in the ROM is much smaller than that in the full FE model, the nonlinear dynamics of the structure can be simulated much more rapidly using numerical continuation packages [16].

In this chapter, we present a route for nonlinear dynamic optimization that is based on an FE-based ROM. The methodology, which is a combination of Particle Swarm Optimization (PSO) with STEP [13] (OPTSTEP), has several beneficial features. First of all, because it uses a derivative-free optimization routine for approaching the optimal design, it can be implemented and combined with FEM packages that are not able to obtain gradients easily. Secondly, the ROM parameters generated in OPTSTEP can facilitate explicitly expressing the optimization goals. Finally, as will be shown, the developed procedure allows using multiple objective functions to approximate a Pareto front, which can help designers in decision-making processes when having to balance performance trade-offs among different objectives. Considering the outstanding performance as ultrasensitive mechanical detectors and the mature fabrication procedure [17, 18], we select high-stress Si_3N_4 for the experimental validation of our methodology.

This chapter is structured as follows. We first introduce and describe the general OPTSTEP methodology. Then we demonstrate the method on the specific challenge of the optimization of the support structure for a high-stress Si_3N_4 nano string, while taking the maximization of its Q-factor and nonlinear Duffing constant β as examples of linear and nonlinear objectives. By comparing the PSO results to the Q and β values that result from a brute-force simulation of a large number of designs that span the design space, we validate that OPTSTEP finds the optimum designs much faster with the same computational resources. Subsequently, we turn to the problem of dealing with

multiple objective functions and focus on simultaneously maximizing both Q and β, demonstrated by a Pareto front. For validation, the results are compared to experimental measurements of fabricated devices. We conclude by demonstrating the potential of OPTSTEP for optimizing the performance of resonant sensors by using more complex objective functions that are relevant for engineering their response time, sensitivity, and power consumption.

5.2. OPTSTEP METHODOLOGY

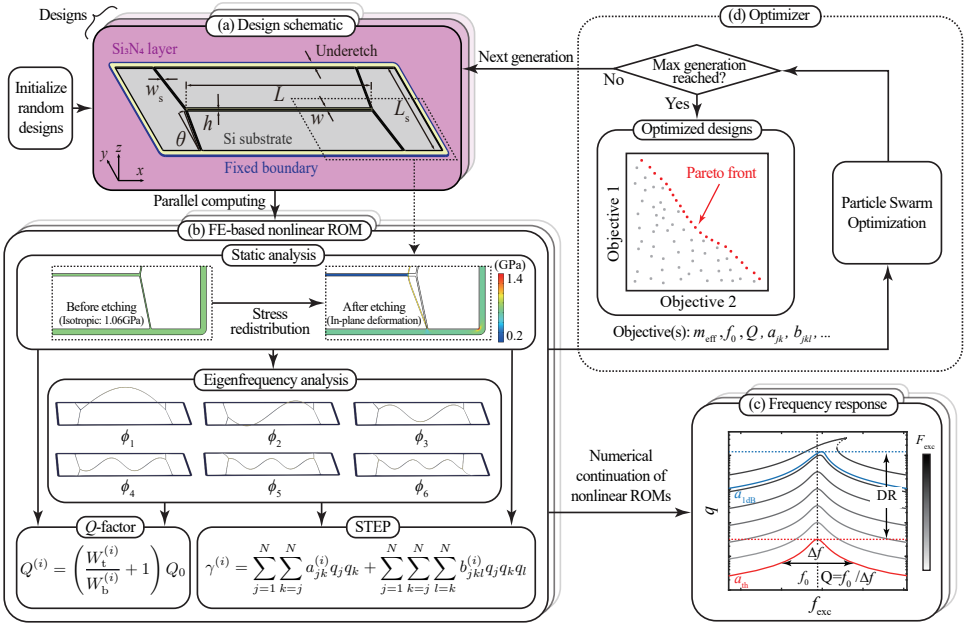

Figure 5.1: **Schematic of the OPTSTEP method** (a) A device geometry is chosen and parameterized by a set of design optimization variables. In this specific case a Si_3N_4 nanomechanical string resonator is chosen for demonstrating OPTSTEP. (b) All designs in one generation are simulated in parallel on a high-performance computing cluster. Static analysis is conducted to evaluate the stress redistribution and deformation after etching, followed by eigenfrequency analysis. Resonance frequencies, mode shapes, Q-factor and the ROM are obtained from the full FE model. (c) The ROM is simulated by numerical continuation. (d) Objective(s) selected from ROM are sent to an optimizer (PSO in this study) to generate design variables for the next generation.

An overview of the OPTSTEP method is schematically shown in Fig. 5.1. In the current work, we use it for engineering a parameterized geometry. We use nanomechanical string resonators with compliant supports, which are shown in Fig. 5.1a, to demonstrate the methodology. We keep the length L and width w of the central string constant, while varying the width w_s, length L_s and angle θ of the supports, as well as the thickness h of the device. It is noted that the OPTSTEP methodology might be used with a larger number of parameters, or even might be extended towards shape or topology optimization of nonlinear dynamic structures. However, such extension is out of the scope of the current

work.

For a certain set of geometrical parameters, a ROM for the parameterized structure is generated using the STEP method [13], which we implemented with shell elements in COMSOL [14]. Besides geometric parameters and boundary conditions (see Fig. 5.1a), the COMSOL simulation contains material parameters (see Section 2.1.1 in Chapter 2), and the initial pre-stress distribution is calculated using a static analysis [14]. We conduct this static analysis assuming the material is isotropic and pre-stressed ($\sigma_0 =$ 1.06 GPa). We then calculate the stress redistribution during the sacrificial layer underetching process, whereby the high-stress Si_3N_4 layer releases from the silicon substrate. Note that in the present study we only consider $\theta \geq 0$, such that the central string is always in tension (in contrast to Ref. [14]). After the static analysis, an eigenfrequency analysis is performed to obtain the out-of-plane eigenmodes ϕ_i (see Fig. 5.1b). These eigenmodes, together with the redistributed stress field obtained from the static analysis, are then used to determine the effective mass m_{eff}, resonance frequency f_0, and Q-factor. We can calculate Q-factors [19, 20] of the ith eigenmode $Q^{(i)}$ based on the stored tension energy $W_{\text{t}}^{(i)}$ and bending energy $W_{\text{b}}^{(i)}$:

$$
\begin{aligned}
W_{\text{t}}^{(i)} &= \frac{h}{2}\iint \sigma_{xx}\left(\frac{\partial\phi_i}{\partial x}\right)^2 + \sigma_{yy}\left(\frac{\partial\phi_i}{\partial y}\right)^2 + 2\sigma_{xy}\frac{\partial\phi_i}{\partial x}\frac{\partial\phi_i}{\partial y}\,\mathrm{d}x\mathrm{d}y, \\
W_{\text{b}}^{(i)} &= \frac{Eh^3}{24(1-\nu^2)}\iint \left(\frac{\partial^2\phi_i}{\partial x^2}\right)^2 + \left(\frac{\partial^2\phi_i}{\partial y^2}\right)^2 + 2\nu\frac{\partial^2\phi_i}{\partial x^2}\frac{\partial^2\phi_i}{\partial y^2} + 2(1-\nu)\left(\frac{\partial^2\phi_i}{\partial x\partial y}\right)^2 \mathrm{d}x\mathrm{d}y,
\end{aligned}
\tag{5.1}
$$

where σ_{xx}, σ_{yy} and σ_{xy} is the stress in the Cartesian coordinate, Q_0 is the intrinsic Q-factor of stress-free Si_3N_4 [21].

As indicated in Fig. 5.1b the STEP method generates a set of coupled nonlinear differential equations[13–15], where the effective nonlinear elastic force acting on the ith mode is given by the function $\gamma^{(i)}$ that depends on the quadratic a_{ij}, cubic b_{ijk} coupling coefficients, and the generalized coordinates q_i. q_i describes the instantaneous contribution of the corresponding mode shapes ϕ_i to the deflection of the structure. Thus, the finite element model with several thousand or even millions of degrees of freedom (DOFs) is reduced to a condensed ROM, that can usually describe the nonlinear dynamics to a good approximation with less than ten degrees of freedom. We can visualize the resulting frequency response curves for different harmonic drive levels by numerical continuation [16], as shown in Fig. 5.1c.

The resulting ROM parameters, including effective mass $m_{\text{eff}}^{(i)}$, Q-factor, linear stiffness $k^{(i)} = m_{\text{eff}}^{(i)}(2\pi f^{(i)})^2$ and nonlinear stiffness terms a_{jk}, b_{jkl}, are passed to the PSO optimizer (see Fig. 5.1d). The algorithm randomly generates many different initial designs by varying the geometric parameters, as shown in Fig. 5.1a. For each of these designs, known as a "particle" in PSO, a ROM is generated by STEP and the corresponding objective functions are computed accordingly and passed to the optimizer. The optimizer then generates a next generation of particles based on the designs from the current generation, the objective functions, and the constraints, with the aim of improving their design parameters to optimize the objectives (see Appendix Section 5.5.1). The optimization loop will iterate until it reaches the predefined maximum generation. If multiple objective functions are selected to be optimized, there is an additional step that

selects the nondominated particles according to Pareto dominance [22]. Because each particle is evaluated independently, PSO enables efficient parallel computing to evaluate all particles in one generation on a high-performance computing cluster.

5.3. OPTSTEP IMPLEMENTATION AND VALIDATION

5.3.1. SINGLE OBJECTIVE OPTIMIZATION WITH OPTSTEP

We implement the presented OPTSTEP methodology to optimize the support geometry of the string resonator shown in Fig. 5.1a. The motion of the fundamental mode of the resonator can be described with the following nonlinear equation of motion:

$$\ddot{q} + \frac{2\pi f_0}{Q}\dot{q} + (2\pi f_0)^2 q + \beta q^3 = F_{\text{exc}} \sin(2\pi f t), \tag{5.2}$$

where q is the displacement at the string center, f_0 is the resonance frequency, Q is the Q-factor, $\beta = b_{111}/m_{\text{eff}}$ is the mass-normalized Duffing constant, and $F_{\text{exc}} \sin(2\pi f t)$ is the mass-normalized harmonic drive force. To demonstrate the single-objective optimization capability of OPTSTEP, we present results for two optimization objectives, respectively: maximizing the Q-factor (shown in Figs. 5.2a,c,d) or maximizing the mass-normalized Duffing constant β (shown in Figs. 5.2b,e,f) of the fundamental mode. We emphasize that a maximum Q or β does not necessarily result in the best performance for all applications of nanomechanical resonators. We choose these optimization objectives as examples to demonstrate that the OPTSTEP methodology can be used to find extreme values of a single objective function, that can be suitably chosen depending on the application requirements. As design parameters, we use the support parameters (L_s, w_s, θ and h in Fig. 5.1a). The PSO algorithm can freely initialize and vary these variables between preset constraints $10\,\mu\text{m} < L_s < 100\,\mu\text{m}$, $1\,\mu\text{m} < w_s < 7\,\mu\text{m}$, $0\,\text{rad} < \theta < 0.4\,\text{rad}$, and $40\,\text{nm} < h < 340\,\text{nm}$.

We initialize the PSO algorithm with 10 randomly generated particles, as indicated by the blue circles at the first generation in Figs. 5.2a-b. The Q and β values of the best performing particle per generation are highlighted by the red line, which converges towards an optimum. Simulated response curves at different drive levels of the initial design (median performance of the initialized particles) and the optimized design are shown in Figs. 5.2c, d for Q and Figs. 5.2e, f for β. It is obvious that the resonance peaks become narrower from Fig. 5.2c to Fig. 5.2d, indicative of an increase in Q-factor. From the backbone curves shown in Figs. 5.2e, f, we see that the resonance frequency of the optimized device shifts more at the same vibration amplitude, which suggests a larger, optimized value of β.

5.3.2. NUMERICAL VALIDATION

In order to validate the PSO results, we compare them to a brute-force parametric study where we simulate a large number of designs that span the full design parameter space, and plot the resulting values of Q and β in the contour plots in Figs. 5.2g, h. Each of these subfigures consists of 16 small contour plots, each of which has a different combination of L_s and h, while along the axes the parameters w_s and θ are varied. The red-colored regions in the plots contain the optimal values of Q and β, which are indicated by a

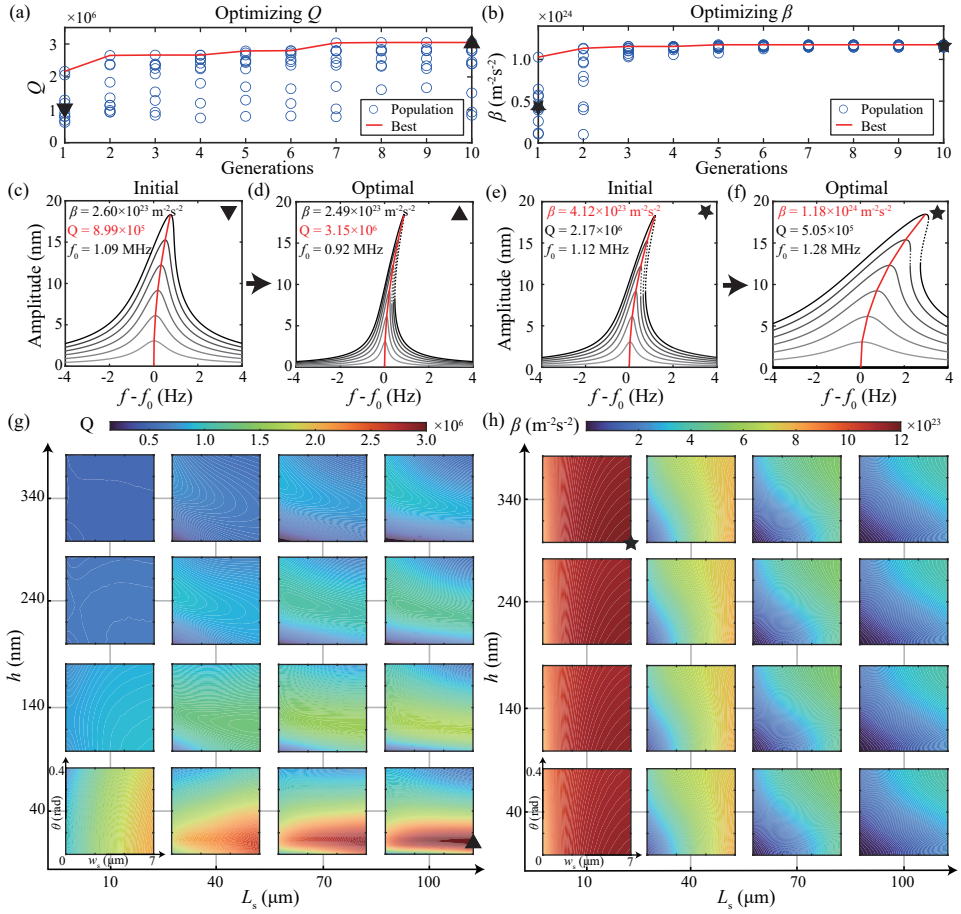

Figure 5.2: **Optimal designs found by particle swarm optimization (PSO) and simulation of different dynamical properties.** Four geometric parameters are selected as design variables in Fig. 5.1. w_s and θ represent x and y axis, respectively, of each contour plot. (a,b) PSO's evolution shows the procedure of searching for maximum (a) Q and (b) β, where the red lines mark the global best design of each generation. (c-f) Frequency response curves around the fundamental mode of (c,e) the designs with median performance in the initial generation and (d,f) the optimized designs, for Q maximization (c,d) and for β maximization (e,f), where the objectives and backbone curves are marked in red. The dotted lines are unstable solutions. The greyscale of response curves go from light to dark as the drive level increases. (g,h) Contour plots show the parametric study for (g) Q-factor and (h) mass-normalized Duffing constant β. The optimized designs found by PSO are marked as an upward-pointing triangle and a star, while the downward-pointing ones represent the designs with average objective values in the initial generation.

triangle and a star. In Appendix Table 5.1, we compare the optimized design parameters from the OPTSTEP method to the best devices from the parametric study. The close agreement between both approaches provides evidence that the OPTSTEP method is able to optimize both linear (Q) and nonlinear (β) parameters of the ROM. The results in Fig. 5.2a are obtained in 30 minutes using a high performance computing cluster, while the parametric study in Fig. 5.2g takes over 325 hours on the same cluster with the same amount of nodes. This illustrates the advantage in computation time that can be realized with OPTSTEP, although it is noted that these times strongly depends on the resolution of the parameter grid and other simulation parameters.

5.3.3. EXPERIMENTAL CHARACTERIZATION

To compare the OPTSTEP method to experimental results, we also perform an experimental parametric study on 15 string resonators with varying support design parameters. For this we fabricated a set of devices with $10\,\mu\text{m} < L_s < 90\,\mu\text{m}$ and $0\,\text{rad} < \theta < 0.2\,\text{rad}$, while keeping $h = 340\,\text{nm}$ and $w_s = 1.0\,\mu\text{m}$ fixed. Fig. 5.3a shows a Scanning Electron Microscope (SEM) image of an array of nanomechanical resonators with varying support designs made of high-stress Si_3N_4. The detailed fabrication and measurement procedures are listed in Section 2.1.1 and 2.1.2 in Chapter 2, respectively.

Fig. 5.3c shows the frequency response at the center of the string at various drive levels for a device with $L_s = 90\,\mu\text{m}$, $w_s = 1\,\mu\text{m}$, $\theta = 0.20\,\text{rad}$ and $h = 340\,\text{nm}$. We estimate the linear resonator parameters of all devices by fitting the measured frequency response curves at various drive levels with the following harmonic oscillator function[14] (see Section 2.1.2 in Chapter 2):

$$q_d(f) = \frac{q_{max,l}/Q}{\sqrt{\left[1-\left(f/f_0\right)^2\right]^2 + f^2/(f_0 Q)^2}}, \tag{5.3}$$

where $q_d(f)$ is the measured amplitude, $q_{max,l}$ is set equal to the maximum measured amplitude $q_{max,nl}$ as the peak amplitude of the linear oscillator, and f is the drive frequency. To determine the nonlinear stiffness, we measure the resonator's frequency response at increasing drive levels, construct the backbone curve, and use the relation between the nonlinear peak amplitude $q_{max,nl}$ and the peak frequency f_{max} to fit and obtain the mass-normalized Duffing constant β using the following equation[23, 24]:

$$f_{max}^2 = f_0^2 + \frac{3}{16\pi^2}\beta q_{max,nl}^2. \tag{5.4}$$

To compensate for small drifts in f_0 during the experiments, before fitting with Eq. (5.3), we plot the frequency response curves along the $f - f_0$ axis [14]. The fitting procedure to obtain f_0, Q and β using Eqs. (4.3) and (5.3) is explained in Section 2.1.2 in Chapter 2.

In Fig. 5.3d-f, we compare the dynamical properties between FE-based ROMs (dots) and measurements on 15 string resonators (diamonds) as a function of L_s and θ. It is evident that the fundamental resonance frequency f_0, Q-factor, and the mass-normalized Duffing constant β of the fabricated devices, are all well predicted by FE-based ROMs. It can also be seen that for short support lengths L_s the device performance is similar, whereas increasing L_s allows tuning f_0, Q and β as we studied in more detail earlier [14,

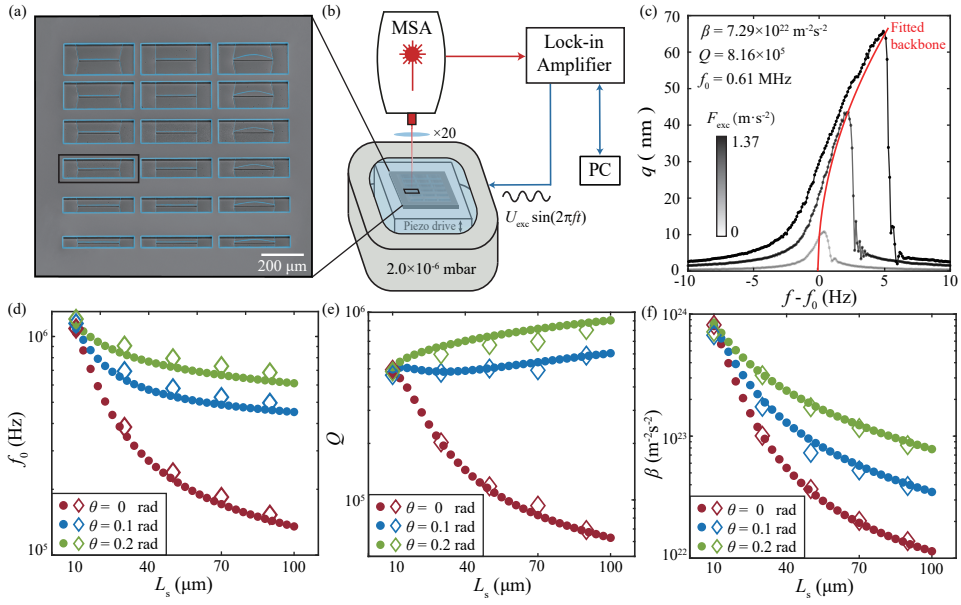

Figure 5.3: **Experimental set-up and experimental validation of the simulations.** (a) Scanning Electron Microscope (SEM) image of an array of devices (colored in blue) with thickness $h = 340$ nm and different design variables. (b) Schematics of the measurement set-up, which includes a Micro System Analyzer (MSA) Laser Doppler Vibrometer (LDV) for motion detection and a piezo-actuator for driving the resonator. (c) Frequency response curves measured around the fundamental resonance frequency of the device with $L_s = 90\,\mu$m, $w_s = 1\,\mu$m, $\theta = 0.20$ rad. The red curve is the fitted backbone. (d-f) Measured (diamonds) and FE-simulated (dots) resonance frequencies, Q-factor and Duffing constant β for various values of the support length L_s and angle θ, for devices with $w_s = 1\,\mu$m and $h = 340$ nm. Error bars of measured results are smaller than the size of diamonds.

19]. In the next section we will compare these experimental results to multi-objective optimization as further validation of OPTSTEP.

5.3.4. MULTI-OBJECTIVE OPTIMIZATION WITH OPTSTEP

For actual device design there are often multiple performance specifications that need to be met. It might sometimes be possible to condense these performance specifications into a single figure of merit, like the $f_0 \times Q$ product for nanomechanical resonators. However, to make the best design decisions, it is preferred that the optimizer works with two (or more) objective functions like enhancing f_0 and Q, simultaneously. To enable this, we implement OPTSTEP with a multi-objective particle swarm optimization (MOPSO), which is an extension of single-objective PSO. After multi-objective optimization, the nondominated particles in the swarm are used to determine an approximation of the Pareto front, which is the set of designs for which improving one of the objectives will always lead to a deterioration of the other objective(s). By performing MOPSO, we aim at finding the Pareto front in the design space for multiple objectives, that represents the boundary on which all optimized designs reside for the chosen variables. As the red dots

show in Fig. 5.1d illustrate, the Pareto front represents the boundary between feasible and unfeasible combinations of objectives and thus allows the designer to make the best trade-off among different objectives.

To demonstrate that multi-objective optimization can be combined with OPTSTEP, we use it to simultaneously maximize Q and β. Devices with high quality factor and nonlinear stiffness can be of interest in cases where we are looking for designs that can drive a string into the nonlinear regime with a minimum driving force and power consumption.

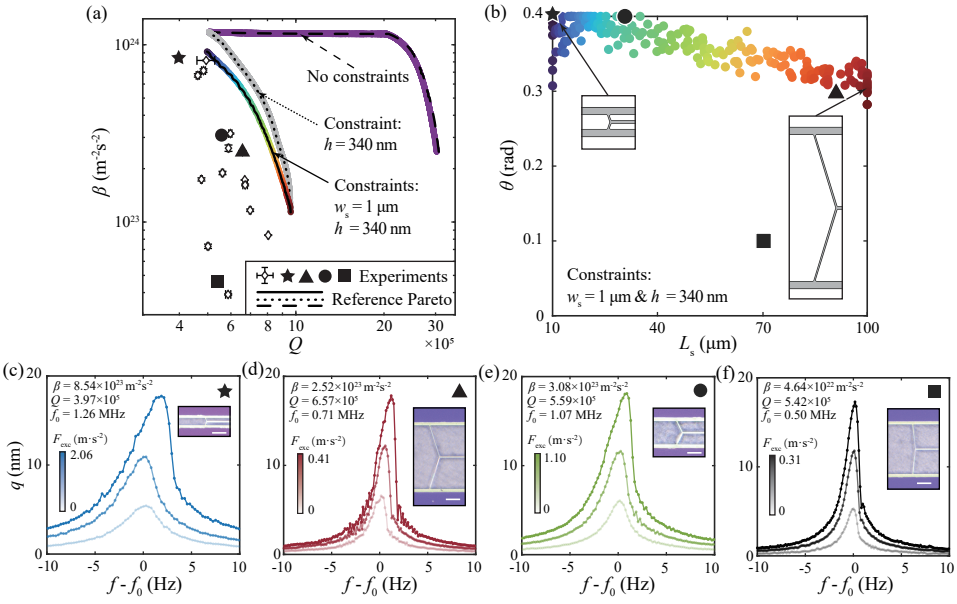

Figure 5.4: **Trade-offs between Q-factor and the mass-normalized Duffing constant β as obtained by combining OPTSTEP with multi-objective particle swarm optimization (MOPSO).** (a) Three Pareto fronts for different constraints (see main text) on design variables are shown in purple, grey and multi-colored dots. Measurements of devices that have the same design variables as the multi-colored Pareto front are shown by diamonds with error bars. The reference Pareto fronts (black solid, dotted and dashed lines) are generated by selecting the designs with maximum Q and β from the parametric study shown in Figs. 5.2g,h for the respective constraints (see Appendix Section 5.5.2). (b) Each dot from the multi-colored Pareto front in (a) is plotted in the design space with the same color. The insets show the support design for a device with maximum Q and a device with maximum β. (c-f) Measured frequency response curves for devices with maximum β (c), maximum Q (d), high Q & β (e), and low Q & β (f). Black symbols in the plots correspond with devices data points plotted in (a) and (b). The insets are images taken by Keyence digital microscope VHX-6000 and white scale bars are 20 µm.

The resulting Pareto fronts are shown in Fig. 5.4a. Since we are also interested in the effect of the constraints on the optimum solutions, we include Pareto fronts with: no constraint (purple), a thickness constraint of $h = 340$ nm (grey), and with thickness and support width constraint (multi-coloured). These 3 Pareto fronts show that there is a clear trade-off between Q and β, with higher Q-factor leading to lower nonlinearity β. The experimental devices share the same constraints ($w_s = 1$ µm and $h = 340$ nm) as the

multi-colored Pareto and are plotted as the hollow diamonds with error bars in Fig. 5.4a (see Appendix Table 5.2). We observe that all experimental points reside in the region on the left hand side of the Pareto front, confirming the area enclosed by the Pareto front indeed captures the feasible devices, and experimentally strengthening the confidence in the OPTSTEP approach for multi-objective designs. The color of the points links the points in the $Q-\beta$ graph in Fig. 5.4a to the corresponding design parameters in Fig. 5.4b. In Fig. 5.4b the schematic support geometries are shown as insets for both maximum β (dark blue) and maximum Q (dark red). We choose some of the fabricated devices close to the Pareto front to show typical measured frequency response curves and microscopic images in Figs. 5.4c-f, which correspond to the star, triangle, circle and square data markers in Figs. 5.4a and b. Together with the microscopic images, it is apparent that with minor alterations in the support region, the response of the string resonators can be largely tuned. To further explore the effect of other design parameters numerically, we release the constraint on w_s, keeping only $h = 340\,\text{nm}$ constrained, and conduct MOPSO (see the grey Pareto front). We can see from the comparison between the grey and multicolored fronts that the performance gain from changing w_s is not very large. In contrast, if we further relax the constraint on $h = 340\,\text{nm}$, which shares the same design space in Figs. 5.2g-h, we obtain the purple Pareto front. The thinner h pushes the Pareto front to have much higher Q. The long plateau at fixed β is mainly attributed to the increase in Q that results from the dependence of the intrinsic quality factor Q_0 on h (see Section 2.1.1 in Chapter 2). Besides validating the MOPSO approach by comparing with experimental data, we also use the data from the parametric study in Fig. 5.2 to extract and generate reference Pareto fronts that are shown as black solid, dotted, and dashed lines in Fig. 5.4a (see Appendix Section 5.5.2), with constraints that match those from the MOPSO optimization.

The OPTSTEP methodology that is presented in this work enables the optimization of the nonlinear dynamic properties of resonant structures using standard FEM software, since it is based on the STEP and uses a derivative-free optimization method. The exclusive reliance on FEM outputs, without requiring information from the full mass and stiffness matrices, increases its generality and allows multi-physics optimization, including also e.g. electromagnetic or thermodynamic phenomena. We note that although derivative-free techniques like PSO are able to efficiently find near-optimal values of design parameters, optimality guarantees can typically not be given, and the techniques are therefore also called metaheuristic optimization techniques. Here, in order to validate the OPTSTEP methodology numerically and experimentally, we have focused on β and Q maximization of the fundamental mode of a string resonator by geometric support design. After having established the methodology, it is now of interest to apply it to explore performance parameters that are more relevant to applications. For example, as shown in Fig. 5.5, our methodology can directly be extended to optimize the power consumption P, sensitivity determined by frequency stability (the limit of detection expressed in Allan Deviation, assuming averaging time $\tau = 1\text{s}$) σ_y and response time τ_r of resonant sensors [25, 26], since these figure-of-merits can be directly expressed in terms of m_{eff}, f_0, Q and β (see Appendix Section 5.5.3). We assume all devices operate at their respective onset of nonlinearity, with sensitivity affected only by thermomechanical noise. In Fig. 5.5, 1000 nondominated particles are found by OPTSTEP to form a

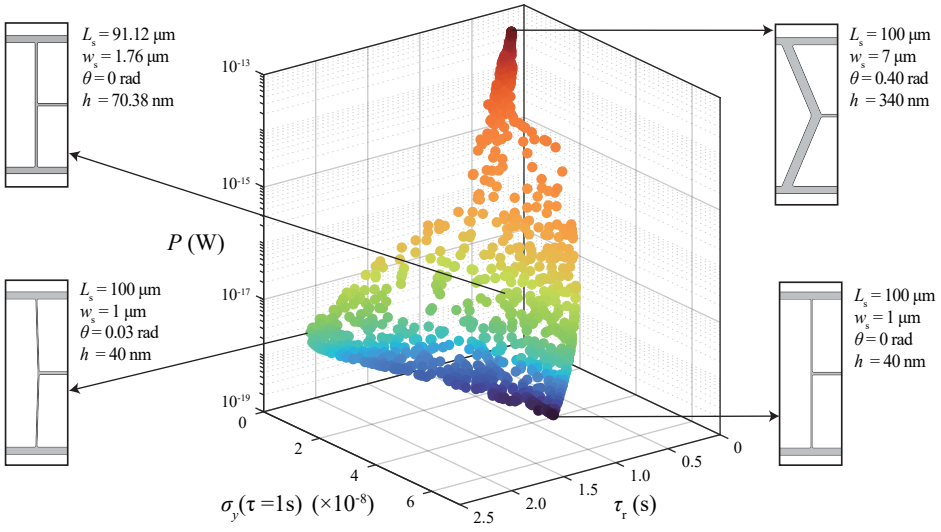

Figure 5.5: **Trade-offs among the power consumption P, sensitivity $\sigma_y(\tau = 1\text{s})$ and response time τ_r of a string resonator with four design parameters.** The insets show the geometries and design parameters of supports of five representative designs on the Pareto frontier. The gradual change of color from dark blue to dark red marks the increasing in power consumption P when operating the nanoresonator at the onset of nonlinearity $a_{1\text{dB}}$ to guarantee the maximum sensitivity.

3D surface that approaches the Pareto frontier with the objective of minimizing P, σ_y and τ_r simultaneously. The particles have the same design constraints as in the example in Fig. 5.2 and the purple Pareto front in Fig. 5.4a, which are $10\,\mu\text{m} < L_s < 100\,\mu\text{m}$, $1\,\mu\text{m} < w_s < 7\,\mu\text{m}$, $0\,\text{rad} < \theta < 0.4\,\text{rad}$, and $40\,\text{nm} < h < 340\,\text{nm}$. The competing design trade-offs between these three objective functions are obtained from OPTSTEP, and are visualized in Fig. 5.5 by showing four typical designs near the Pareto frontier. As demonstrated by the designs at the upper right corner of the Pareto frontier, we can conclude that the devices with shorter response time are more likely to have thicker supports, which lead to a higher resonance frequency f_0 combined with a low Q, thus resulting in a smaller Q/f_0 ratio. At the same time, these thicker supports also contribute to a larger onset of nonlinearity $a_{1\text{dB}}$ [14], so the resonators are able to work at much larger amplitudes in the linear regime, which provides a better sensitivity σ_y. However, the larger $a_{1\text{dB}}$ and m_{eff} will require more energy to sustain the oscillation at resonance that causes higher power consumption P. In contrast, the devices with much lower power consumption P while maintaining comparably high sensitivity σ_y, which are shown at the lower left corner in Fig. 5.5, are equipped with more slender supports. With only a slight increase of support angle θ from 0, the low torsional stiffness of supports is maintained while the stress in the central string can be significantly increased [19], leading to a higher Q, which can be confirmed by Fig. 5.2g. Consequently, when aiming at designing a resonant sensor with relatively low power consumption P, high sensitivity σ_y and short response time τ_r with compliant supports, a pair of slender and slightly angled supports, together with a medium thickness of Si_3N_4 layer is generally favored.

In other cases, like approaching the quantum regime with a nonlinear nanomechanical resonator [27], it is beneficial to maximize Q and β simultaneously. The OPTSTEP methodology can also be used for more complex design problems that involve multiple modes [5, 8, 14, 28], for avoiding or taking advantage of mode coupling, for instance by optimizing nonlinear coupling coefficients (a_{jk} and b_{jkl} in Fig. 5.1b) and resonance frequency ratios. Since OPTSTEP generates the ROM parameters at each generation, it is particularly suited for dealing with cases where the device specifications can be expressed in terms of these parameters. Interesting challenges include increasing frequency stability by coherent energy transfer [29, 30], signal amplification [31] and stochastic sensing [4, 32]. Moreover, intriguing paths for further research involve inclusion of nonlinear damping or extension to full topology optimization [6]. Also the use of alternative optimization strategies, like binary particle swarm optimization (BPSO) [33], that could generate radically new geometries, is an interesting direction.

5.4. CONCLUSION

To sum up, we presented a methodology (OPTSTEP) for optimizing the nonlinear dynamics of mechanical structures by combining an FE-based ROM method with a derivative-free optimization technique (PSO). We demonstrated and validated the methodology by optimizing the support design of high-stress Si_3N_4 nanomechanical resonators. The method was verified numerically by comparing its results to a brute-force parametric study, for both single- and multi-objective optimization. Experimental data on the Q-factor and Duffing nonlinearity were in correspondence with the OPTSTEP results. The capability of the method was also demonstrated by multi-objective optimization of the support for the nanomechanical resonator, targeting improvements in power consumption, sensitivity and response time in resonant sensing. We thus conclude that the method can be applied to a wide range of complex design challenges including nonlinear dynamics, and is expected to be compatible to most FE codes and derivative-free optimization routines. It holds the potential to facilitate and revolutionize the way (nano)dynamical systems are designed, thus pushing the ultimate performance limits of sensors, mechanisms and actuators for scientific, industrial, and consumer applications.

5.5. APPENDIX

5.5.1. PARTICLE SWARM OPTIMIZATION

Here, we elaborate the details in our optimizer as show in Fig. 5.6, which is based on the algorithms initiated by [22, 34]. For single objective function, the velocity of the ith particle of the $(j+1)$th generation is decided by three parts respectively:

$$v_i^{(j+1)} = C_0 v_i^{(j)} + C_1 \left(PBest_i^{(j)} - x_i^{(j)} \right) + C_2 \left(GBest^{(j)} - x_i^{(j)} \right), \tag{5.5}$$

where $v_i^{(j)}$ and $x_i^{(j)}$ are the velocity and position of the ith particle at the jth generation, $PBest_i^{(j)}$ is the best design that the ith particle has had, $GBest^{(j)}$ is the best design among particles in the jth generation. C_0 is the inertia weight, C_1 and C_2 are acceleration coefficients. C_0, C_1 and C_2 are all set as 2. Accordingly, we can update the design of

the ith particle at the $(j+1)$th generation as:

$$x_i^{(j+1)} = x_i^{(j)} + v_i^{(j+1)}. \tag{5.6}$$

In order to deal with multiple objectives, the concept of Pareto dominance is introduced [22]. A particle is Pareto optimal (nondominated) if there exists no other particles in the same generation that would improve some objectives without causing a simultaneous derogation in at least one other objective. According to the Pareto dominance, we selected nondominated particles from each generation and stored them in an external repository, which is updated for each iteration. The velocity of the ith particle of the $(j+1)$th generation is derived based on:

$$v_i^{(j+1)} = C_0 v_i^{(j)} + C_1 \left(PBest_i^{(j)} - x_i^{(j)} \right) + C_2 \left(Rep^{(j)} - x_i^{(j)} \right), \tag{5.7}$$

where $Rep^{(j)}$ is one nondominated particle chosen from the repository. The design space is divided into hypercubes and the nondominated particles fall into different hypercubes randomly. The hypercubes with more nondominated particles are assigned a lower weight that are less likely to be selected according to roulette-wheel selection. This promotes a more equidistantly distributed nondominated particles along the Pareto front.

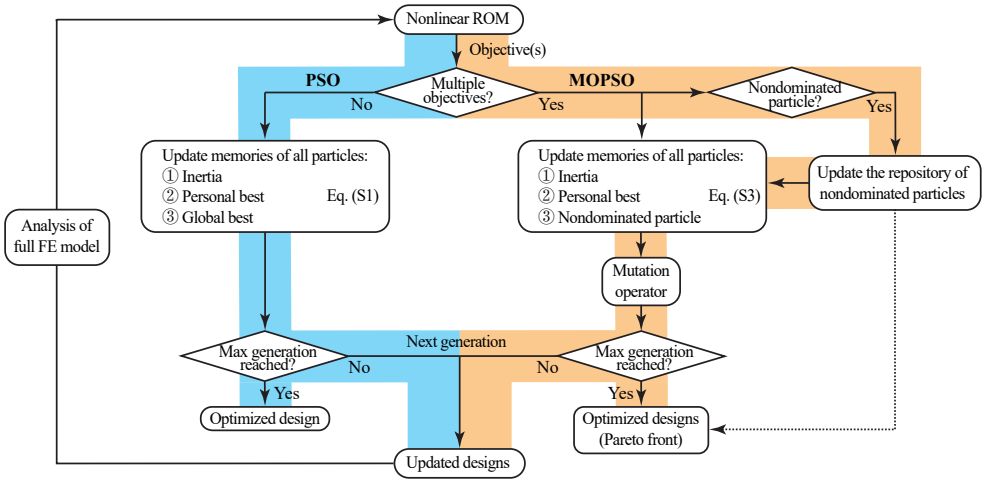

Figure 5.6: **Details of the optimizer in Fig. 5.1.** According to the amount of objective functions, two routes based on particle swarm optimization (PSO) are available, respectively. A repository for nondominated particles is built additionally for multi-objective particle swarm optimization (MOPSO).

Besides, to reduce the drawbacks of PSO that it may converge to a local minimum due to a high convergence speed, a mutation operator is introduced after the design update of all particles. The mutation rate is designed to drop as the generation increases, which guarantees a high exploration of the whole design space at the beginning of the optimization.

Table 5.1: Values and corresponding geometric design parameters for Q and β in Fig. 5.2

Dynamical properties	Values	L_s (μm)	w_s (μm)	θ (rad)	h (nm)
Optimized Q from PSO	3.05×10^6	83.51	6.87	0.06	40.00
Maximum Q from parametric study	3.15×10^6	100.00	7.00	0.06	40.00
Optimized β from PSO	1.18×10^{24} ($m^{-2}s^{-2}$)	10.00	7.00	0.03	340.00
Maximum β from parametric study	1.18×10^{24} ($m^{-2}s^{-2}$)	10.00	7.00	0	340.00

In Appendix Table 5.1, we list the values and corresponding geometric design parameters of both Q-factor and the mass-normalized Duffing constant β obtained by PSO and by searching the parametric study results in Fig. 5.2 of the main text.

5.5.2. VALIDATION OF MOPSO

We generate reference Pareto fronts from parametric studies according to the Pareto criterion mentioned in Appendix Section 5.5.1, as shown in Fig. 5.7. We evenly discretize the design space $L_s = 10 \sim 100\,\mu m$, $\theta = 0 \sim 0.4 rad$, $w_s = 1 \sim 7\,\mu m$ and $h = 40 \sim 340\,nm$ and build the 1-dof nonlinear reduced-order model according to the finite element analysis of the full model. The black lines are used in Fig. 5.4 of the main text as references for the MOPSO-generated Pareto fronts.

Table 5.2: Values and corresponding geometric design parameters for Q and β in Fig. 5.4

θ (rad)	L_s(μm)	Q	β($m^{-2}s^{-2}$)	Mark
0.4	90	671081	1.62×10^{23}	
0.4	70	561570	1.89×10^{23}	
0.4	50	588671	2.61×10^{23}	
0.4	30	558798	3.08×10^{23}	●
0.4	10	397014	8.54×10^{23}	★
0.3	90	657047	2.52×10^{23}	▲
0.2	90	804593	8.44×10^{22}	
0.2	70	698133	1.17×10^{23}	
0.2	50	668694	1.73×10^{23}	
0.2	30	597314	3.15×10^{23}	
0.2	10	483734	7.15×10^{23}	
0.1	90	587378	3.90×10^{22}	
0.1	70	541695	4.64×10^{22}	■
0.1	50	501157	7.30×10^{22}	
0.1	30	475866	1.74×10^{23}	
0.1	10	462534	6.71×10^{23}	
0	90	69112	1.38×10^{22}	
0	70	93174	2.02×10^{22}	
0	50	118166	3.68×10^{22}	
0	30	202588	1.01×10^{23}	
0	10	493902	8.15×10^{23}	

Besides, we show the measured Q-factor and the mass-normalized Duffing constant β of our fabricated devices with constraints $w_s = 1\,\mu m$ and $h = 340\,nm$. We observe that

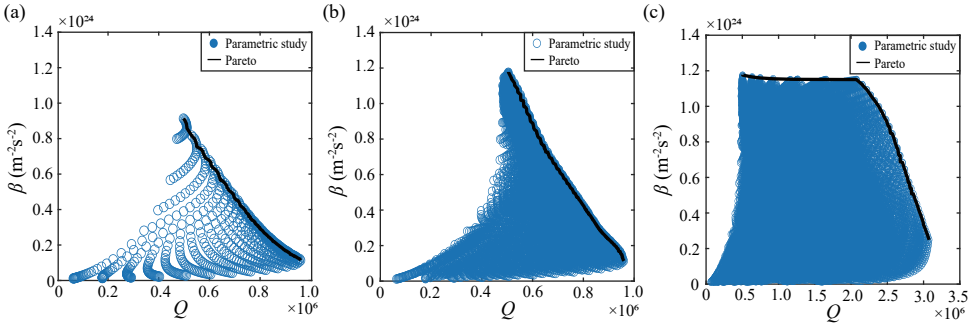

Figure 5.7: **Reference Pareto fronts of different design spaces.** (a) Pareto front of varying L_s and θ while fixing $w_s = 1\,\mu m$ and $h = 340\,nm$. (b) Pareto front of varying L_s ,θ and w_s while fixing $h = 340\,nm$. (c) Pareto front of varying L_s ,θ, w_s and h. The blue circles show the FE-based ROMs of devices corresponding to different design spaces.

they all reside in the lower left side compared to the colored Pareto front, which proves the reliability of Pareto fronts found by MOPSO. In Appendix Table 6.2, we list the geometric parameters of the measured devices, which are shown as diamonds with error bars in Fig. 4(a), and their corresponding Q and β. Some of the devices listed in Appendix Table 6.2 is out of the range of Fig. 4(a) because of low Q or β.

5

5.5.3. FIGURE-OF-MERITS IN A RESONANT SENSOR

Firstly, the response time τ_r demonstrates the responsivity of a resonant sensor subjected to external stimuli, which is related to the resonance frequency and the corresponding Q-factor [25]:

$$\tau_r = \frac{Q}{\pi f_0}. \tag{5.8}$$

Secondly, for a resonant sensor that operates in linear regime, the sensitivity is determined by its frequency stability that is influenced by noise. The highest signal-to-noise ratio can be obtained by operating it at the onset of nonlinearity a_{1dB}, where it has the largest amplitude [25, 35, 36]. Assuming the thermomechanical noise dominates the noise floor, we use Allan Deviation as the measure of frequency stability in the closed loop measurement to evaluate the sensitivity of our devices:

$$\sigma_y(\tau) = \frac{1}{2\sqrt{2}QSNR\sqrt{\Delta f}}\frac{1}{\sqrt{\tau}}, \tag{5.9}$$

where SNR can be expressed as the ratio between the onset of nonlinearity a_{1dB} and the thermomechanical noise a_{th} [14]:

$$SNR = \frac{a_{1dB}}{a_{th}} = \frac{0.9244\sqrt{\frac{\alpha}{Q\beta}}}{\sqrt{\frac{4k_BTQ\Delta f}{m_{eff}\alpha^{\frac{3}{2}}}}} = 0.4622\left(k_BT\Delta f\right)^{-\frac{1}{2}} m_{eff}^{\frac{1}{2}} Q^{-1}\alpha^{\frac{5}{4}}\beta^{-\frac{1}{2}}. \tag{5.10}$$

k_B is the Boltzmann's constant and $\alpha = (2\pi f_0)^2$ equals to the mass-normalized linear stiffness. We assume the resonator operates in room temperature $T = 298$K with the measurement bandwidth $\Delta f = 1$Hz. After substituting Eq. 5.10 into Eq. 5.9, we can have the relationship between $\sigma_y(\tau)$ and other parameters from ROM, which is irrelevant to Q:

$$\sigma_y(\tau) = 0.765\,(k_B T)^{\frac{1}{2}}\, m_{\text{eff}}^{-\frac{1}{2}}\, \alpha^{-\frac{5}{4}}\, \beta^{\frac{1}{2}}\, \tau^{-\frac{1}{2}}. \tag{5.11}$$

Thirdly, we define the power consumption P as the energy that is needed to be fed to the devices per second, i.e., the energy dissipated per second:

$$P = \frac{\Delta W}{T_0} = f_0 \Delta W, \tag{5.12}$$

where ΔW is the energy dissipated per oscillation cycle, T_0 is the period of one oscillation cycle. Considering the definition of damping ratio:

$$\zeta = \frac{1}{2Q} = \frac{\Delta W}{4\pi W}, \tag{5.13}$$

and the total energy stored in the resonator supposed that it is operated at the onset of nonlinearity $a_{1\text{dB}}$ for the best sensitivity:

$$W = \frac{1}{2} m_{\text{eff}} \alpha\, a_{1\text{dB}}^2, \tag{5.14}$$

we can derive the power consumption P as:

$$P = \frac{2\pi f_0}{Q} \cdot \frac{1}{2} m_{\text{eff}} \alpha\, a_{1\text{dB}}^2. \tag{5.15}$$

It is worth noticing that when the resonator is operated at the onset of nonlinearity, the potential energy stored in the geometric nonlinearity is several magnitudes smaller than W, that can be neglected.

BIBLIOGRAPHY

[1] S. O. Erbil, U. Hatipoglu, C. Yanik, M. Ghavami, A. B. Ari, M. Yuksel, and M. S. Hanay, "Full electrostatic control of nanomechanical buckling", Physical Review Letters **124**, 046101 (2020).

[2] M. Yuksel, E. Orhan, C. Yanik, A. B. Ari, A. Demir, and M. S. Hanay, "Nonlinear nanomechanical mass spectrometry at the single-nanoparticle level", Nano Letters **19**, 3583–3589 (2019).

[3] F. Bayram, D. Gajula, D. Khan, and G. Koley, "Mechanical memory operations in piezotransistive GaN microcantilevers using au nanoparticle-enhanced photoacoustic excitation", Microsystems & Nanoengineering **8**, 1–14 (2022).

[4] W. J. Venstra, H. J. Westra, and H. S. van Der Zant, "Stochastic switching of cantilever motion", Nature Communications **4**, 2624 (2013).

[5] J. M. Miller, A. Gomez-Franco, D. D. Shin, H.-K. Kwon, and T. W. Kenny, "Amplitude stabilization of micromechanical oscillators using engineered nonlinearity", Physical Review Research **3**, 033268 (2021).

[6] D. Høj, F. Wang, W. Gao, U. B. Hoff, O. Sigmund, and U. L. Andersen, "Ultra-coherent nanomechanical resonators based on inverse design", Nature Communications **12**, 5766 (2021).

[7] D. Schiwietz, M. Hörsting, E. M. Weig, M. Wenzel, and P. Degenfeld-Schonburg, "Shape optimization of geometrically nonlinear modal coupling coefficients: an application to mems gyroscopes", arXiv preprint arXiv:2403.17679 (2024).

[8] S. Dou, B. S. Strachan, S. W. Shaw, and J. S. Jensen, "Structural optimization for nonlinear dynamic response", Philosophical Transactions of the Royal Society A: Mathematical, Physical and Engineering Sciences **373**, 20140408 (2015).

[9] L. L. Li, P. M. Polunin, S. Dou, O. Shoshani, B. Scott Strachan, J. S. Jensen, S. W. Shaw, and K. L. Turner, "Tailoring the nonlinear response of mems resonators using shape optimization", Applied Physics Letters **110**, 081902 (2017).

[10] M. P. Mignolet, A. Przekop, S. A. Rizzi, and S. M. Spottswood, "A review of indirect/non-intrusive reduced order modeling of nonlinear geometric structures", Journal of Sound and Vibration **332**, 2437–2460 (2013).

[11] C. Touzé, A. Vizzaccaro, and O. Thomas, "Model order reduction methods for geometrically nonlinear structures: a review of nonlinear techniques", Nonlinear Dynamics **105**, 1141–1190 (2021).

[12] M. Cenedese, J. Axås, B. Bäuerlein, K. Avila, and G. Haller, "Data-driven modeling and prediction of non-linearizable dynamics via spectral submanifolds", Nature Communications **13**, 872 (2022).

[13] A. A. Muravyov and S. A. Rizzi, "Determination of nonlinear stiffness with application to random vibration of geometrically nonlinear structures", Computers & Structures **81**, 1513–1523 (2003).

[14] Z. Li, M. Xu, R. A. Norte, A. M. Aragón, P. G. Steeneken, and F. Alijani, "Strain engineering of nonlinear nanoresonators from hardening to softening", Communications Physics **7**, 53 (2024).

[15] A. Ke şkekler, V. Bos, A. M. Aragón, P. G. Steeneken, and F. Alijani, "Multimode nonlinear dynamics of graphene resonators", Phys. Rev. Appl. **20**, 064020 (2023).

[16] A. Dhooge, W. Govaerts, Y. A. Kuznetsov, H. G. E. Meijer, and B. Sautois, "New features of the software matcont for bifurcation analysis of dynamical systems", Mathematical and Computer Modelling of Dynamical Systems **14**, 147–175 (2008).

[17] M. Xu, D. Shin, P. M. Sberna, R. van der Kolk, A. Cupertino, M. A. Bessa, and R. A. Norte, "High-strength amorphous silicon carbide for nanomechanics", Advanced Materials **36**, 2306513 (2024).

[18] A. Cupertino, D. Shin, L. Guo, P. G. Steeneken, M. A. Bessa, and R. A. Norte, "Centimeter-scale nanomechanical resonators with low dissipation", Nature Communications **15**, 4255 (2024).

[19] Z. Li, M. Xu, R. A. Norte, A. M. Aragón, F. van Keulen, F. Alijani, and P. G. Steeneken, "Tuning the Q-factor of nanomechanical string resonators by torsion support design", Applied Physics Letters **122**, 013501 (2023).

[20] D. Shin, A. Cupertino, M. H. de Jong, P. G. Steeneken, M. A. Bessa, and R. A. Norte, "Spiderweb nanomechanical resonators via bayesian optimization: inspired by nature and guided by machine learning", Advanced Materials, 2106248.

[21] L. G. Villanueva and S. Schmid, "Evidence of surface loss as ubiquitous limiting damping mechanism in SiN micro-and nanomechanical resonators", Physical Review Letters **113**, 227201 (2014).

[22] C. A. C. Coello, G. T. Pulido, and M. S. Lechuga, "Handling multiple objectives with particle swarm optimization", IEEE Transactions on Evolutionary Computation **8**, 256–279 (2004).

[23] A. H. Nayfeh and D. T. Mook, *Nonlinear oscillations* (John Wiley & Sons, 2008).

[24] S. Schmid, L. G. Villanueva, and M. L. Roukes, *Fundamentals of nanomechanical resonators*, Vol. 49 (Springer, 2016).

[25] A. Demir and M. S. Hanay, "Fundamental sensitivity limitations of nanomechanical resonant sensors due to thermomechanical noise", IEEE Sensors Journal **20**, 1947–1961 (2019).

[26] T. Manzaneque, M. K. Ghatkesar, F. Alijani, M. Xu, R. A. Norte, and P. G. Steeneken, "Resolution limits of resonant sensors", Physical Review Applied **19**, 054074 (2023).

[27] C. Samanta, S. De Bonis, C. Møller, R. Tormo-Queralt, W. Yang, C. Urgell, B. Stamenic, B. Thibeault, Y. Jin, D. Czaplewski, et al., "Nonlinear nanomechanical resonators approaching the quantum ground state", Nature Physics, 1–5 (2023).

[28] A. Foster, J. Maguire, J. Bradley, T. Lyons, A. Krysa, A. Fox, M. Skolnick, and L. Wilson, "Tuning nonlinear mechanical mode coupling in gaas nanowires using cross-section morphology control", Nano Letters **16**, 7414–7420 (2016).

[29] D. Antonio, D. H. Zanette, and D. López, "Frequency stabilization in nonlinear micromechanical oscillators", Nature Communications **3**, 1–6 (2012).

[30] C. Chen, D. H. Zanette, D. A. Czaplewski, S. Shaw, and D. López, "Direct observation of coherent energy transfer in nonlinear micromechanical oscillators", Nature Communications **8**, 1–7 (2017).

[31] R. L. Badzey and P. Mohanty, "Coherent signal amplification in bistable nanomechanical oscillators by stochastic resonance", Nature **437**, 995–998 (2005).

[32] P. Belardinelli, W. Yang, A. Bachtold, M. Dykman, and F. Alijani, "Hidden mechanical oscillatory state in a carbon nanotube revealed by noise", arXiv preprint arXiv:2312.14034 (2023).

[33] J. J. Lake, A. E. Duwel, and R. N. Candler, "Particle swarm optimization for design of slotted mems resonators with low thermoelastic dissipation", Journal of Microelectromechanical Systems **23**, 364–371 (2013).

[34] R. C. Eberhart, Y. Shi, and J. Kennedy, *Swarm intelligence* (Elsevier, 2001).

[35] A. Cleland and M. Roukes, "Noise processes in nanomechanical resonators", Journal of applied physics **92**, 2758–2769 (2002).

[36] K. Ekinci, Y. T. Yang, and M. Roukes, "Ultimate limits to inertial mass sensing based upon nanoelectromechanical systems", Journal of applied physics **95**, 2682–2689 (2004).

6

6

Cascade of Modal Interactions in Nanomechanical Resonators with Soft Clamping

Mode coupling in nanoresonators provides an efficient way to transfer energy between vibrational modes. In this work, we show that soft-clamping techniques—widely used to obtain high-Q nanomechanical resonators—can be harnessed to effectively tune intermodal couplings. Using Si_3N_4 nanostrings with soft-clamping supports, we obtain successive modal interactions between five mechanical modes, achieving a quasi-constant amplitude of the targeted mode across a broad frequency range. Through analytical and nonlinear reduced-order modeling, we reveal how soft-clamping supports influence the onset of coupling and significantly amplify the spring hardening nonlinearity—enhancing it by more than an order of magnitude via multiple dispersive couplings. We further discuss the design potential of the soft-clamping supports to tailor nanoresonators with desired nonlinear couplings.

Parts of this chapter have been published in *arXiv* (2025) by Zichao Li, Minxing Xu, Richard A. Norte, Alejandro M. Aragón, Peter G. Steeneken, Farbod Alijani.

6.1. INTRODUCTION

MICRO- and nanoscale mechanical systems are highly susceptible to nonlinear oscillations owing to their small dimensions. A wealth of nonlinear phenomena have been observed and studied in these systems [1–8], among which mode coupling stands out as it offers opportunities for frequency stabilization [9, 10], energy harvesting [11], and frequency comb generation [12, 13]. Mode coupling in a resonant structure occurs when two or more vibrational modes interact at relatively large amplitudes [14]. Among different mechanical systems, high-Q nanoresonators are particularly well suited to exploit mode coupling due to their rapid activation of nonlinearities [15]. In these systems, modal interactions are typically achieved by modulating tension or incorporating symmetry-breaking forces through optomechanical or electromechanical couplings [12, 16]. These effects however can introduce higher-order nonlinearities [17, 18] or undesirable back-action [19], which can limit their practical utility. Consequently, geometric design strategies, particularly those leveraging soft-clamping techniques, have received significant attention for their potential to finely tune both linear [20–22] and nonlinear [23] properties of nanomechanical systems.

Here, we experimentally and numerically demonstrate that soft-clamping techniques can serve as effective knobs for achieving intermodal couplings in nanoresonators. By performing measurements on softly clamped nanostrings, we observe multiple modal interactions between out-of-plane (OOP) vibrational modes. Through combined analytical and finite element (FE)-based reduced-order models (ROMs), we quantify the coupling strength and uncover how mode coupling shapes and enhances the tunability of spring hardening nonlinearity. These studies allow us to experimentally amplify the effective Duffing constant of nanostrings by more than an order of magnitude via leveraging a cascade of dispersive couplings between five mechanical modes. This confirms that quasi-constant nonlinear dynamic responses are attainable by engineering mode coupling over a wide frequency range. Finally, we discuss how soft-clamping supports can be engineered to manipulate the onset and strength of mode couplings through geometric optimization.

6.2. MODE COUPLING IN HIGH-Q STRING RESONATORS

Our measurements are performed on Si_3N_4 nanostrings (thickness $h = 90\,\text{nm}$, pre-stress $\sigma_0 = 1.08\,\text{GPa}$) featuring slender support beams at the boundaries to mediate soft clamping (see Section 2.1.1 in Chapter 2). Fig. 6.1a shows our measurement set-up, with the inset illustrating the geometric parameters of one fabricated device. To investigate the influence of the supports on large-amplitude oscillations and nonlinear coupling of the nanoresonators, an array of devices is fabricated. All devices have central strings with identical dimensions ($L = 200\,\mu\text{m}$, $w = 2\,\mu\text{m}$), but differ in support length L_s, width w_s, and angle θ. We note that the presence of soft-clamping supports tunes the in-plane stress in the central string [20, 23].

To characterize the nonlinear dynamics of softly clamped string resonators, we fix the chip comprising suspended resonators to a piezo actuator that provides a harmonic base excitation in the OOP direction. We use a Zurich Instruments HF2LI lock-in amplifier to perform frequency sweeps in the spectral neighborhood of the fundamental resonance,

and then use a MSA400 Polytec laser Doppler vibrometer (LDV) to detect the mechanical vibrations of our devices. The measurement laser is focused at the position $1/12L$ from the support on the central string, ensuring it is distant from nodal points of the three lowest OOP modes (see Appendix Section 6.7.1). We perform all measurements at room temperature in a vacuum chamber with a pressure below 2×10^{-6} mbar to minimize air damping.

To probe the geometric nonlinearity of our devices, we perform forward frequency sweeps at different drive levels and measure the vibrations of the central string [23]. Fig. 6.1b shows the frequency responses at various drive levels, ranging from $U_{\text{exc}} = 10\,\text{mV}$ to 100 mV, for a device with $w_s = 1\,\mu\text{m}$, $L_s = 50\,\mu\text{m}$, and $\theta = 0$. During frequency sweeps around the fundamental resonance frequency f_1, the detected higher harmonics are negligible in comparison to the driven one, indicating that the device operates in its fundamental mode without coupling to other mechanical modes. To quantify the strength of nonlinearity, we use the Duffing equation:

$$\ddot{q}_1 + c_1 \dot{q}_1 + \omega_1^2 q_1 + \beta_1 q_1^3 = F_{\text{exc}} \sin(2\pi f t), \tag{6.1}$$

where q_1 is the generalized coordinate of the fundamental mode, $F_{\text{exc}} \sin(2\pi f t)$ is its effective harmonic drive with excitation frequency f from the piezo. Furthermore, $\omega_1 = 2\pi f_1$, $c_1 = \omega_1/Q_1$ and β_1 are the angular resonance frequency, mass-normalized damping coefficient and Duffing constant, respectively, where Q_1 is the quality factor. We extract β_1 by fitting the backbone (red line in Fig. 6.1b) of the measured frequency response curves using the expression: $f_{\text{max}}^2 = f_1^2 + \frac{3}{16\pi^2}\beta_1 A_{\text{max}}^2$, where f_{max} is the drive frequency at the maximum amplitude A_{max} [24, 25].

In Fig. 6.1c, we show the frequency response of the same device measured in Fig. 6.1b driven at a stronger excitation level ($U_{\text{exc}} = 6\,\text{V}$) around the fundamental resonance. Apart from the signal demodulated with the drive frequency f, we also observe a noticeable increase in higher harmonics demodulated at $2f$ and $3f$, whose frequency responses are shown in yellow and ochre lines, respectively. We note that the frequency response of the fundamental mode deviates from the backbone curve of the Duffing response (see the red line in Fig. 6.1c) when the higher harmonics are detected. Since the resonance frequencies of higher modes of a string resonator are close to integer multiples of the fundamental mode, we attribute the deviation from the backbone curve to modal interactions between the fundamental and higher-order modes. We note that the frequency ratios $f_2/f_1 = 2$ and $f_3/f_1 = 3$ suggest the presence of modal interactions between the fundamental mode (f_1) with the second (f_2) and third (f_3) OOP modes, respectively. We further observe a drop in the frequency response of the fundamental mode which we attribute to the energy redistribution among the three OOP modes [4]. When the oscillations of the coupled modes drop, the energy stored in the higher modes transfers back to the driven mode, bringing its amplitude closer to its backbone, as indicated by the arrows in Fig. 6.1c. In Fig. 6.1d, we present the spectrum and the time trace under $U_{\text{exc}} = 6\,\text{V}$, showing the coupling between the first and second modes at $f = 209.89\,\text{kHz}$, and the coupling between the first and third modes at $f = 216.26\,\text{kHz}$.

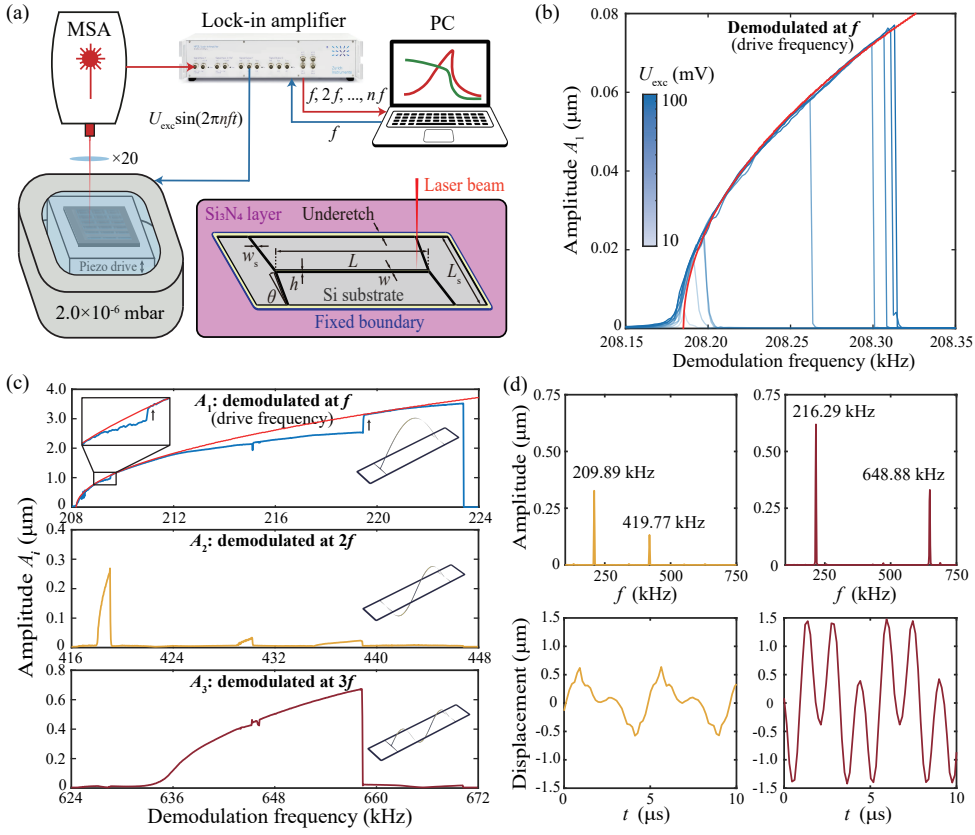

Figure 6.1: **Measurement of mode couplings in nanomechanical string resonators with soft-clamping supports.** (a) Schematic of the measurement set-up comprising an MSA400 laser Doppler vibrometer (LDV) for reading-out the motion at different harmonics of the drive frequency (f, $2f$, ..., nf) and a piezo-actuator for generating the excitation. The inset illustrates the design parameters of a Si_3N_4 nanomechanical string resonator with soft-clamping supports. The laser shows the measurement position, which avoids the nodal points of the three lowest OOP modes. (b) Duffing nonlinear response curves of the lowest OOP mode of the device with $w_s = 1\,\mu m$, $L_s = 50\,\mu m$, and $\theta = 0$, under different drive levels without mode coupling. (c) Nonlinear response curves of the same device under a stronger drive level ($U_{exc} = 6\,V$). The second (yellow) and third (ochre) OOP modes are both activated by mode coupling. The arrows in the first graph indicate the direction of the energy transfer back to the driven fundamental mode (lowest OOP) from higher modes activated by mode coupling. (d) Frequency spectrum and time domain signals of mode coupling between the first and second modes at $f = 209.89\,kHz$ (yellow), and between the first and third modes at $f = 216.29\,kHz$ (ochre), respectively.

6.3. IMPACT OF SOFT CLAMPING ON MODE COUPLING

To further quantify the influence of support design on mode coupling, we measure four devices with $w_s = 1\mu m$, $\theta = 0$ undergoing intermodal coupling between the lowest two modes, for different support lengths L_s (see Fig. 6.2a). Here, the blue lines represent the response curves of the fundamental mode during the forward sweep, while the yellow lines depict the response curves of the higher-frequency coupled modes, demodulated at $2f$. The colors gradually fade as L_s decreases. These curves indicate that strings with longer supports have smaller values of detuning $f - f_1$ at the same vibration amplitude. This occurs because slender supports offer lower rigidity to in-plane motion, allowing the central string to relax more during large-amplitude vibrations and thus resulting in weaker geometric nonlinearity [23]. The Scanning Electron Microscope (SEM) image of the measured devices is also shown in Fig. 6.2a.

To understand the influence of soft-clamping supports on the coupled dynamics of the first two OOP modes of the string, we further develop a simplified model of a string with finite in-plane stiffness k_{in} at both ends [23] (see Appendix Section 6.7.2):

$$\ddot{q}_1 + c_1\dot{q}_1 + \omega_1^2 q_1 + \beta_1 q_1^3 + \gamma q_1 q_2^2 = 0, \tag{6.2a}$$

$$\ddot{q}_2 + c_2\dot{q}_2 + \omega_2^2 q_2 + \beta_2 q_2^3 + \gamma q_1^2 q_2 = 0. \tag{6.2b}$$

Here, q_2 is the generalized coordinate of the second mode. $\omega_2 = 2\pi f_2$, $c_2 = \omega_2/Q_2$ and β_2 are the angular resonance frequency, mass-normalized damping coefficient and Duffing constant, respectively, where Q_2 is the quality factor of the second mode. We shall note that the devices in our work are subjected to high tension, with no broken symmetry or offset from flat configuration. Consequently, there are no quadratic couplings which can lead to 1:2 internal resonance [12]. Yet, here γ represents the mass-normalized dispersive coupling term between the two modes that promotes energy transfer [14]. Accordingly, we derive the analytical expressions for nonlinear coefficients β_1, β_2 and γ (see Section 2.2.2 in Chapter 2):

$$\beta_1 = \frac{\pi^4 E}{4\rho L^4}\left(1 + \frac{2Ewh}{k_{in}L}\right)^{-1}, \tag{6.3a}$$

$$\beta_2 = \frac{4\pi^4 E}{\rho L^4}\left(1 + \frac{2Ewh}{k_{in}L}\right)^{-1}, \tag{6.3b}$$

$$\gamma = \frac{\pi^4 E}{\rho L^4}\left(1 + \frac{2Ewh}{k_{in}L}\right)^{-1}. \tag{6.3c}$$

E is the Young's modulus, ρ is the mass density, and dimensional parameters are indicated in Fig. 6.1a. It is evident from Eqs. (6.3a), (6.3b) and (6.3c) that there is a factor four difference between the nonlinear coefficients: $\beta_2 = 4\gamma = 16\beta_1$. At the same time, all these nonlinear coefficients are scaled by the same factor $[(1 + 2Ewh/(k_{in}L)]^{-1}$, which captures the effect of the finite in-plane stiffness k_{in} of the soft-clamping supports. We plot their relationships with the support length L_s in Fig. 6.2b with the blue, yellow and green lines, respectively, and observe a decrease of two orders of magnitude for all terms caused by the reduction of k_{in} for longer supports. In addition to the simplified string model, we also use FE models to understand the influence of geometric parameters on

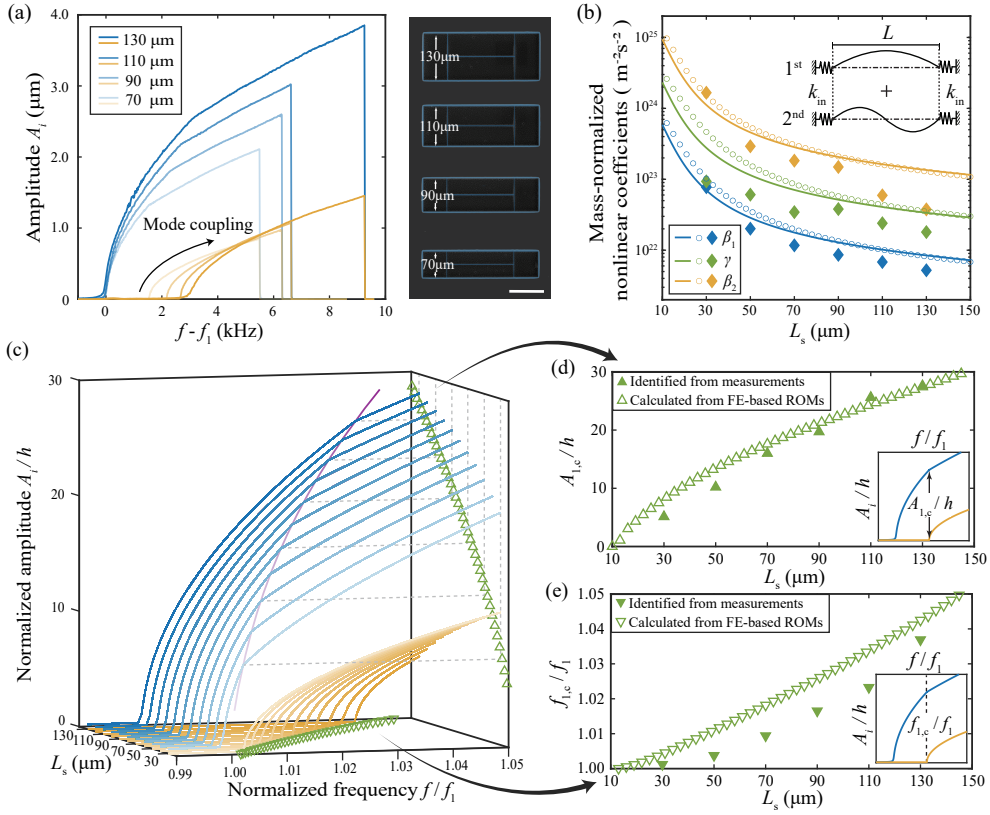

Figure 6.2: **Influence of the soft-clamping supports on the coupled dynamics of the lowest two modes of high-stress nanomechanical string resonators driven near the fundamental resonance frequency f_1.** (a) Measured response curves of the coupled response between the lowest two modes of string resonators with four different L_s. The blue lines are the response curves of forward frequency sweeps, which are demodulated by the drive frequency f around the first OOP mode, while the yellow lines are the ones of the second OOP mode demodulated by $2f$. The colors of the curves gradually fade as the support length decreases. The Scanning Electron Microscope (SEM) image shows the measured devices (colored in blue) with different L_s. The white bar is 100μm. (b) Analytical (solid lines), FE-based ROM (hollow circles) and experimentally measured (solid diamonds) nonlinear coefficients (β_1, β_2, γ) of devices with $w_s = 1$μm, $\theta = 0$, and varying L_s. (c) Simulated response curves using the FE-based ROMs of devices with $w_s = 1$μm, $\theta = 0$, and varying L_s. The blue lines represent the first OOP modes and the yellow ones represent the second OOP modes. The upward and downward hollow triangles represent the onset frequency of the coupled mode ($f_{1,c}/f_1$) and the corresponding amplitude ($A_{1,c}/h$), respectively, as predicted by Eqs. (6.5a) and (6.5b). The purple line plots the onset of internal resonance ($f_{1,c}/f_1$, $A_{1,c}/h$) for different L_s, which coincides with the kink in the blue frequency response curves. (d)(e) Comparison of the onset amplitude $A_{1,c}/h$ and frequency $f_{1,c}/f_1$ of the coupled mode obtained from FE-based ROMs (hollow triangles) and identified directly from measurements (solid triangles). The insets show the definitions of $f_{1,c}/f_1$ and $A_{1,c}/h$, respectively.

our fabricated nanoresonators, based on which we build a two-degree-of-freedom (2-dof) ROM that comprises the lowest two OOP modes (see previous works for more details [23, 26, 27]). The hollow circles in Fig. 6.2b represent values of β_1, β_2 and γ obtained from FE-based ROMs, which show good agreement with the analytical results.

Adding to these, we also fit the measured response curves in Fig. 6.2a to experimentally obtain the values of β_1, β_2 and γ. To perform the fitting, we use the Harmonic Balance Method (HBM) and obtain analytical backbone expressions of the coupled dynamics with the excitation frequency $\omega = 2\pi f$ as follows:

$$\omega^2 = \omega_1^2 + \frac{1}{2}\gamma A_2^2 + \frac{3}{4}\beta_1 A_1^2 \tag{6.4a}$$

$$\omega^2 = \frac{1}{4}\omega_2^2 + \frac{1}{8}\gamma A_1^2 + \frac{3}{16}\beta_2 A_2^2. \tag{6.4b}$$

Here, A_1 and A_2 are the amplitudes of the driven mode q_1 and the coupled mode q_2, respectively. We note that when $A_2 = 0$, Eq. (6.4a) yields the backbone expression of the first mode. In Fig. 6.2b, we plot the experimentally fitted values of the nonlinear coefficients β_1, β_2 and γ with solid diamonds, whose values follow the same pattern as the analytical and FE-based ROMs (see Appendix Section 6.7.4 for the measurement data). Next, by using Eqs. (6.4a) and (6.4b), we obtain analytical expressions to predict the onset of coupling with the second mode by assuming $\omega = \omega_{1,c}$, $A_1 = A_{1,c}$ and $A_2 = 0$:

$$\omega_{1,c} = \sqrt{\frac{\omega_2^2 - \frac{2\gamma}{3\beta_1}\omega_1^2}{4 - \frac{2\gamma}{3\beta_1}}}, \tag{6.5a}$$

$$A_{1,c} = \sqrt{\frac{\omega_2^2 - 4\omega_1^2}{3\beta_1 - \frac{1}{2}\gamma}}. \tag{6.5b}$$

Here, $\omega_{1,c} = 2\pi f_{1,c}$ represents the onset frequency of the coupled mode, and $A_{1,c}$ denotes the amplitude of the first mode at $\omega_{1,c}$, corresponding to the frequency and amplitude where the slope of the Duffing curve changes. We note that the onset of coupling with the second mode does not occur exactly at $f = 1/2 f_2$ (see Eq. (6.5a)).

To verify Eqs. (6.5a) and (6.5b), Fig. 6.2c presents $f_{1,c}/f_1$ (upward triangles) and $A_{1,c}/h$ (downward triangles) calculated using the parameters from FE-based 2-dof ROMs of devices with $w_s = 1\,\mu\text{m}$, $\theta = 0$, and varying L_s. These results are shown together with the frequency response obtained from simulating the same ROMs by numerical continuation [28]. The blue lines show the response curves of the driven mode when the frequency is swept forward, while the yellow lines represent the ones of the second mode activated through mode coupling. We observe that the gradual change of $f_{1,c}/f_1$ and $A_{1,c}/h$ with L_s (see purple curve) aligns closely with the trend indicated by the green triangles. In Figs. 6.2d and e, we present the same results (hollow triangles) alongside values identified directly from measured response curves (solid triangles). The strong consistency between measured and simulated values confirms that the derived Eqs. (6.5a) and (6.5b) can reliably predict the onset of coupling between the first and second modes.

6.4. MODAL INTERACTIONS BETWEEN MULTIPLE MODES

Apart from the onset of two-mode coupling, we can see from Fig. 6.2a that this coupled response also has an impact on the spring-hardening nonlinearity of the driven mode. In order to investigate this tuning effect further, we derive the relationship between A_1 and ω due to mode coupling by eliminating A_2 from Eqs. (6.4a) and (6.4b) (see Appendix Section 6.7.2):

$$\omega^2 = \frac{\omega_1^2 - \frac{2\gamma}{3\beta_2}\omega_2^2}{1 - \frac{8\gamma}{3\beta_2}} + \frac{\frac{3}{4}\beta_1 - \frac{\gamma^2}{3\beta_2}}{1 - \frac{8\gamma}{3\beta_2}} A_1^2. \tag{6.6}$$

Since Eq. (6.6) remains a parabolic expression similar to a backbone curve, we define the coefficient of A_1^2 as the effective mass-normalized Duffing constant $\beta_{1,\text{eff}}$ to characterize the amplitude-frequency relationship of the first mode undergoing dispersive couplings. As a natural extension, we also introduce additional coupled modes to explore the influence of successive dispersive couplings on the Duffing response of the first mode $\beta_{1,\text{eff}}$ (see Appendix Section 6.7.5):

$$\beta_{1,\text{eff}}^{(i)} = \frac{3}{4}\beta_{1,\text{eff}}^{(i-1)} + \frac{3i^2\beta_{1,\text{eff}}^{(i-1)}\gamma_{1,i} - 2\gamma_{1,i}^2}{6\beta_i - 4i^2\gamma_{1,i}}, \tag{6.7}$$

where $\beta_{1,\text{eff}}^{(i)}$ is the effective Duffing constant by including up to the ith mode ($i \geq 2$), β_i is the Duffing constant of the ith mode, $\gamma_{1,i}$ is the dispersive coupling strength between the first and ith modes. $\beta_{1,\text{eff}}^{(2)}$ is identical to the effective Duffing constant in Eq. (6.6) and $\beta_{1,\text{eff}}^{(1)}$ refers to β_1. Substituting dynamical parameters obtained from the FE-based ROMs for the device with $w_s = 1\,\mu\text{m}$, $L_s = 50\,\mu\text{m}$ and $\theta = 0$, we find 52% increase in $\beta_{1,\text{eff}}$ by including two-mode dispersive coupling. Moreover, through successive dispersive couplings among five mechanical modes, Eq. (6.7) predicts that $\beta_{1,\text{eff}}$ can increase beyond 26 times (see Table 6.1 in Appendix Section 6.7.5).

To further verify this analytical prediction, we simulate the frequency response of an FE-based 5-dof ROM for the same device. In Fig. 6.3a, as we sweep the drive frequency f forward, the second (yellow), third (ochre), fourth (cyan), and fifth (purple) OOP modes sequentially engage in the coupled response, leading to a quasi-constant amplitude- frequency response where $\beta_{1,\text{eff}}^{(5)} \to \infty$ [29]. The additional tuning effect compared to the values calculated by Eq. (6.7) is attributed to the inclusion of all coupling terms related to cubic geometric nonlinearity, rather than limiting the analysis to only dispersive couplings for deriving the analytical backbone expression. The kinks in the blue response curves of the first mode can be explained by Eq. (6.7), which appear whenever a higher-order mechanical mode starts to interact with the fundamental mode. The significant suppression of the vibration amplitude in the driven mode can be explained by treating the coupled modes as energy reservoirs, which absorb the additional energy pumped into the driven mode [30, 31].

We also experimentally carry out frequency sweeps on a device with the same geometry as used for the simulation in Fig. 6.3a. To activate all five modes simultaneously, we use an even stronger drive level ($U_{\text{exc}} = 20\,\text{V}$) compared to our measurements shown in Fig. 6.1c. As shown in Fig. 6.3b, the measured frequency response is consistent with our simulation result, except for the amplitude levels, which we attribute to the differences

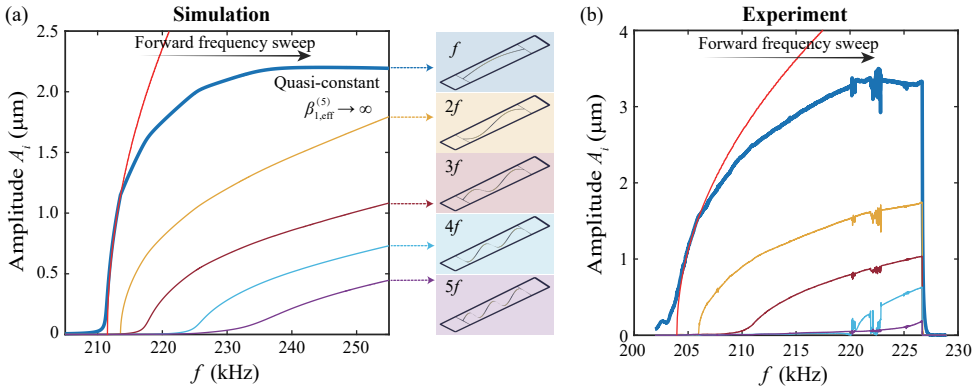

Figure 6.3: **Multi-mode interactions in a nanostring.** (a) Simulated response curves of a forward frequency sweep under five-mode couplings of the device with $w_s = 1\,\mu\text{m}$, $L_s = 50\,\mu\text{m}$, and $\theta = 0$. The bold blue line is the frequency response of the first mode, while the others represent the second (yellow), third (ochre), fourth (cyan) and fifth (purple) OOP modes, respectively. The mode shapes from the eigenfrequency analysis of the FE full model are shown on the right. (b) Measured response curves of a forward frequency sweep under five-mode couplings of the same device as in (a). The bold blue line is the frequency response demodulated by the drive frequency f, while the others represent the signals demodulated by $2f$ (yellow), $3f$ (ochre), $4f$ (cyan) and $5f$ (purple), respectively. The red lines in (a) and (b) represent the fitted backbone curves of the first mode before mode couplings initiate.

from measurement conditions and material properties. We shall note that the amplitude fluctuations after the onset of the fourth mode are attributed to the energy leakage to higher modes, where we observe a series of higher harmonics ($n > 5$) emerging in the frequency spectrum. In summary, both simulations and experiments confirm that soft clamping allows for substantial tuning of driven mode's Duffing response by facilitating nonlinear couplings with other vibrational modes in nanoresonators.

6.5. ENGINEERING MODE COUPLING BETWEEN TWO MODES BY GEOMETRIC OPTIMIZATION

The close agreement between the analytical/numerical results and the experimental findings not only clarifies the effect of support beams on the nonlinear coupling coefficients, but also suggests that their geometric engineering can be used to suppress or enhance dispersive couplings. To that end, we conduct a parametric study considering only two-mode dispersive coupling to assess the extent to which designing the support beams can tune the frequency response curve. We use three design parameters, namely: $10\,\mu\text{m} < L_s < 100\,\mu\text{m}$, $1\,\mu\text{m} < w_s < 7\,\mu\text{m}$, and $0\,\text{rad} < \theta < 0.5\,\text{rad}$. In Figs. 6.4a-b, we show the onset amplitude of mode coupling A_{IR} and the backbone's tuning ratio β_{eff}/β, respectively, calculated from the FE-based ROMs (see Appendix Section 6.7.2). This parametric study allows us to identify the geometric conditions that lead to two-mode dispersive coupling by driving either the first or second mode. We plot $A_{1,c}$ and β_{eff}/β as functions of the three design parameters L_s, w_s, and θ, and indicate the boundaries between modal couplings that can be achieved by driving the first and second modes with

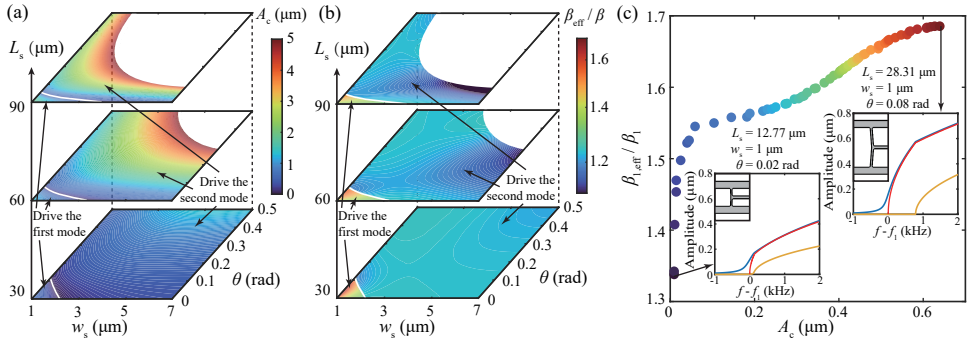

Figure 6.4: **Design potential of the dispersive coupling between the lowest two OOP modes in nanomechanical string resonators with soft-clamping supports.** (a-b) Contour plots of the onset amplitude of the dispersive coupling $A_{1,c}$ and the backbone's tuning ratio β_{eff}/β_1 of the driven mode, respectively. The white solid line in each contour plot marks the boundary between the coupled response that can be achieved by driving the first and the second modes. The empty zones are devices with $A_{1,c} > 5$μm, whose $A_{1,c}$ is so large that is limited by the 5μm gap between the suspended Si_3N_4 devices and the silicon substrate. (c) Pareto fronts found by multi-objective particle swarm optimization. The insets display simulated response curves of the device with the lowest onset amplitude of $A_{1,c}$ and the highest backbone's tuning ratio $\beta_{1,eff}/\beta_1$, under dispersive coupling between the lowest two modes, respectively. The corresponding design parameters of the soft-clamping supports are provided for each case. The blue lines represent the response curves of the first mode during forward frequency sweeps near its resonance, while the yellow lines correspond to those of the second mode.

white lines. The contours reveal that designs near these boundaries have lower $A_{1,c}$, thus facilitating mode coupling. In the same figures, the empty zones represent designs with $A_{1,c} > 5$μm, which exceed the 5μm limit imposed by the gap between the suspended Si_3N_4 devices and the silicon substrate.

Facilitated by Multi-Objective Particle Swarm Optimization (MOPSO) [32, 33], we then optimize for designs with the lowest $A_{1,c}$ and the largest $\beta_{1,eff}/\beta_1$. MOPSO is capable of handling multiple design objectives while considering the trade-offs between them based on Pareto dominance. As depicted in Fig. 6.4c on the Pareto front, the obtained nondominated designs share the same design space as the lower-left regions in Figs. 6.4a-b when driving the first mode. We can see the trade-off between $A_{1,c}$ and $\beta_{1,eff}/\beta_1$, achieving a maximum increase in the effective Duffing constant of approximately 70%. Additionally, we show the simulated response curves for the designs with the lowest $A_{1,c}$ and the highest $\beta_{1,eff}/\beta_1$ in the insets, respectively, where the backbones of the first mode are highlighted in red to visualize the impact of dispersive coupling. Since the design with maximum $\beta_{1,eff}/\beta_1$ does not lie at the boundary of the design space for L_s and θ, $\beta_{1,eff}/\beta_1$ can only be increased by reducing w_s below the boundary of 1μm, which would risk breaking the high-stress devices. Therefore, we conclude that further increasing $\beta_{1,eff}/\beta_1$ will require more complex support geometries or more coupled modes, as suggested in Fig. 6.3.

6.6. CONCLUSION

In conclusion, we investigated the influence of soft clamping on dispersive modal couplings in nanomechanical resonators and proposed a geometric engineering strategy accordingly. By both theoretical and experimental studies, we demonstrated that soft-clamping supports can tune the Duffing constant and the coupling strength of high-Q string resonators by more than an order of magnitude. This tuning capability is enabled by the high Q factor achieved through soft clamping, which facilitates the activation of a large number of mechanical modes and minimizes the total input energy required to trigger modal couplings. Moreover, the flexibility of the design with soft-clamping supports allows for effective tuning of frequency ratios to activate the coupling of higher modes by driving the lower ones, or vice versa [33]. For instance, as shown in the inset with minimum $A_{1,c}$ in Fig. 6.3c, a resonance frequency ratio close to two between the first two modes enables rapid entry into the coupling regime without requiring excessively high vibrational amplitudes to compensate for large frequency detuning. This not only allows for control over the onset of mode coupling but also significantly enhances the flexibility in introducing additional coupled modes, enabling a cascade of modal interactions and a substantial rescaling of the Duffing response. The proposed tuning method relies exclusively on geometrical adjustments, making it highly compatible with FE-based ROMs and metaheuristic optimization algorithms to program the nonlinear dynamics of nanoresonators through geometric design. By engineering modal couplings during the design phase, this method lays the basis for developing large arrays of nanomechanical resonators with intentionally tailored nonlinear functionalities, for applications as varied as energy harvesting [11], frequency comb generation [12, 34], and computing [35–37].

6.7. APPENDIX

6.7.1. SIMULTANEOUS MEASUREMENT OF DIFFERENT RESONANCE MODES

In order to detect the low-order OOP modes simultaneously under mode couplings, we focus the laser beam of the MSA LDV on the central string at $1/12L$ away from the support, as shown in Fig. 6.5, which avoids the nodes (zero amplitude) of these modes. We use Zurich lock-in amplifier to demodulate the measured signal with the driven frequency f and its higher harmonics nf (n=2, 3, ...). Next, we convert the measured displacements of different modes to their corresponding maximum displacements q_1, q_2, ..., q_n according to different mode shapes, in order to facilitate the comparison with analytical and FE-based ROMs. Moreover, since mode couplings induced by the geometric nonlinearity normally happens in strong nonlinear regime with large amplitude, it is also beneficial to measure locations with relatively smaller amplitudes, away from the peaks of various modes. This approach helps to ensure that the measured signals remain within the limited measurement range of the MSA LDV.

6.7.2. TWO-MODE DISPERSIVE COUPLING

Our devices can be treated as simply supported string resonators, so the effective mass of the low-order OOP modes are approximately the same [38]. Since our resonators are symmetric in the vibration direction, we only consider cubic nonlinear terms in our

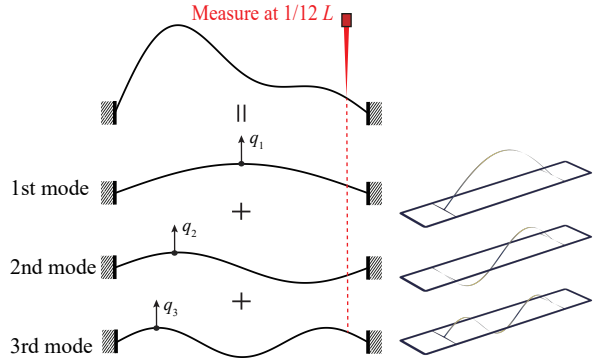

Figure 6.5: **Simultaneous measurement of multiple modes by LDV.** q_1, q_2 and q_3 are the maximum displacements of the three lowest OOP modes, respectively. The mode shapes obtained by eigenfrequency analysis of the FE full model are listed next to the simplified ones.

mass-normalized equations of motion [23]:

$$\begin{aligned}\ddot{q}_1 + c_1\dot{q}_1 + \omega_1^2 q_1 + k_{111}^{(1)} q_1^3 + k_{112}^{(1)} q_1^2 q_2 + k_{122}^{(1)} q_1 q_2^2 + k_{222}^{(1)} q_2^3 = 0 \\ \ddot{q}_2 + c_2\dot{q}_2 + \omega_2^2 q_2 + k_{111}^{(2)} q_1^3 + k_{112}^{(2)} q_1^2 q_2 + k_{122}^{(2)} q_1 q_2^2 + k_{222}^{(2)} q_2^3 = 0.\end{aligned} \tag{6.8}$$

in which q_1 and q_2 represent the displacement of the first and second modes, c_1 and c_2 represent the mass-normalized damping coefficients, ω_1 and ω_2 are the eigenfrequencies, k with superscripts and subscripts are mass-normalized nonlinear stiffness. It is worth noting that in Eq. (6.8), not all terms are resonant under the interaction between two modes of a string with a resonance frequency ratio close to two. To recover the resonant terms, we assume harmonic motions of the form $q_1 = A_1\cos(\omega t)$ and $q_2 = A_2\cos(2\omega t)$ as a first approximation, and simplify Eq. (6.8) as:

$$\begin{aligned}\ddot{q}_1 + c_1\dot{q}_1 + \omega_1^2 q_1 + k_{111}^{(1)} q_1^3 + k_{122}^{(1)} q_1 q_2^2 = 0 \\ \ddot{q}_2 + c_2\dot{q}_2 + \omega_2^2 q_2 + k_{112}^{(2)} q_1^2 q_2 + k_{222}^{(2)} q_2^3 = 0,\end{aligned} \tag{6.9}$$

where the resonant dispersive coupling term could be written as $\gamma = k_{122}^{(1)} = k_{112}^{(2)}$, and the mass-normalized Duffing constant of the first and second modes could be written as $\beta_1 = k_{111}^{(1)}$ and $\beta_2 = k_{222}^{(2)}$, respectively. For simplicity, we rewrite Eq. (6.9) as:

$$\begin{aligned}\ddot{q}_1 + c_1\dot{q}_1 + \omega_1^2 q_1 + \beta_1 q_1^3 + \gamma q_1 q_2^2 = 0 \\ \ddot{q}_2 + c_2\dot{q}_2 + \omega_2^2 q_2 + \gamma q_1^2 q_2 + \beta_2 q_2^3 = 0.\end{aligned} \tag{6.10}$$

To understand the influence of the dispersive coupling on the kink observed in the frequency response curves in Fig. 6.2a, next we use the harmonic balance method (HBM), and assume the solution to be of the form: $q_1 = A_1\cos(\omega t)$ and $q_2 = A_2\cos(2\omega t)$.

Replacing these harmonic responses in Eq. (6.10), gives:

$$\omega^2 = \omega_1^2 + \frac{1}{2}\gamma A_2^2 + \frac{3}{4}\beta_1 A_1^2 \tag{6.11a}$$

$$\omega^2 = \frac{1}{4}\omega_2^2 + \frac{1}{8}\gamma A_1^2 + \frac{3}{16}\beta_2 A_2^2. \tag{6.11b}$$

We assume the second mode is activated at $\omega_{1,c}$, where $A_2 = 0$ and $A_1 = A_{1,c}$. Then Eqs. (6.11a) and (6.11b) become:

$$\omega_{1,c}^2 = \omega_1^2 + \frac{3}{4}\beta_1 A_{1,c}^2 \tag{6.12a}$$

$$\omega_{1,c}^2 = \frac{1}{4}\omega_2^2 + \frac{1}{8}\gamma A_{1,c}^2. \tag{6.12b}$$

There are two unknown parameters ($\omega_{1,c}$ and $A_{1,c}$) in Eqs. (6.12a) and (6.12b). By solving them, we can analytically derive the position where the first mode's backbone undergoes a kink, as shown in Fig. 6.6a:

$$\omega_{1,c} = \sqrt{\frac{\omega_2^2 - \frac{2\gamma}{3\beta_1}\omega_1^2}{4 - \frac{2\gamma}{3\beta_1}}} \tag{6.13a}$$

$$A_{1,c} = \sqrt{\frac{\omega_2^2 - 4\omega_1^2}{3\beta_1 - \frac{1}{2}\gamma}}. \tag{6.13b}$$

Furthermore, by eliminating A_2 from Eqs. (6.11a) and (6.11b) we can obtain the backbone of the first mode during mode coupling as follows:

$$\omega^2 = \frac{\omega_1^2 - \frac{2\gamma}{3\beta_2}\omega_2^2}{1 - \frac{8\gamma}{3\beta_2}} + \frac{\frac{3}{4}\beta_1 - \frac{\gamma^2}{3\beta_2}}{1 - \frac{8\gamma}{3\beta_2}} A_1^2. \tag{6.14}$$

We define the coefficient of A_1^2 term as effective Duffing constant $\beta_{1,\text{eff}}$ of the first mode during mode coupling.

Similar to the way we get Eqs. (6.11a) and (6.11b), if we harmonically drive the system around ω_2 with ω, we can also get the backbone expression for both modes:

$$\omega^2 = 4\omega_1^2 + 2\gamma A_2^2 + 3\beta_1 A_1^2 \tag{6.15a}$$

$$\omega^2 = \omega_2^2 + \frac{1}{2}\gamma A_1^2 + \frac{3}{4}\beta_2 A_2^2, \tag{6.15b}$$

We assume the coupled first mode is activated at $\omega_{2,c}$, where $A_1 = 0$ and $A_2 = A_{2,c}$. Then Eqs. (6.15a) and (6.15b) become:

$$\omega_{2,c}^2 = 4\omega_1^2 + 2\gamma A_{2,c}^2 \tag{6.16a}$$

$$\omega_{2,c}^2 = \omega_2^2 + \frac{3}{4}\beta_2 A_{2,c}^2. \tag{6.16b}$$

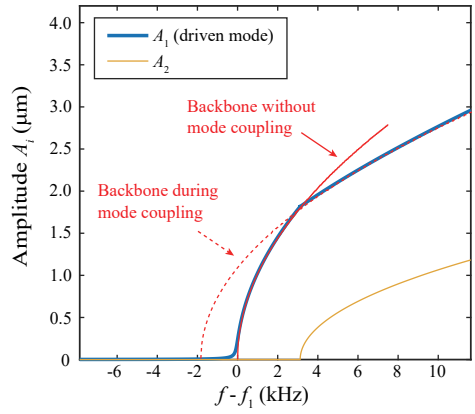

Figure 6.6: **Derivation of the effective backbone curve under two-mode dispersive coupling.** The simulated response curve of a forward frequency sweep near the first mode's resonance, activating the coupling of the second mode.

There are two unknown parameters ($\omega_{2,c}$ and $A_{2,c}$) in Eqs. (6.16a) and (6.16b). By solving them, we can analytically derive the position where the second mode's backbone undergoes a kink:

$$\omega_{2,c} = \sqrt{\frac{4\omega_1^2 - \frac{8\gamma}{3\beta_2}\omega_2^2}{1 - \frac{8\gamma}{3\beta_2}}} \tag{6.17a}$$

$$A_{2,c} = \sqrt{\frac{4\omega_1^2 - \omega_2^2}{\frac{3}{4}\beta_2 - 2\gamma}}. \tag{6.17b}$$

Furthermore, by eliminating A_1 in Eqs. (6.15a) and (6.15b), we can have the relationship between A_2 and ω, which is still a parabola similar to the backbone curve:

$$\omega^2 = \frac{\omega_2^2 - \frac{2\gamma}{3\beta_1}\omega_1^2}{1 - \frac{\gamma}{6\beta_1}} + \frac{\frac{3}{4}\beta_2 - \frac{\gamma^2}{3\beta_1}}{1 - \frac{\gamma}{6\beta_1}} A_2^2. \tag{6.18}$$

We define the coefficient of A_2^2 term as effective Duffing constant $\beta_{2,\text{eff}}$ of the second mode during mode coupling.

6.7.3. FITTING NONLINEAR COEFFICIENTS BY A SINGLE FREQUENCY SWEEP

We developed a fitting strategy for the fast characterization of nonlinear properties of high-Q nanomechanical resonators that undergo dispersive coupling. In Fig. 6.7a, we present the measured frequency response curve for a device with $w_s = 1\,\mu\text{m}$, $L_s = 90\,\mu\text{m}$, and $\theta = 0$, where we observed the activation of the second OOP mode by driving the first OOP mode in the nonlinear regime. It is worth noticing that in high-Q Duffing resonators, frequency sweeps in the nonlinear regime can bring the oscillations to their

high-amplitude stable branches, which are in close proximity to their backbones [24]. Consequently, we can approximately fit for unknown coefficients in the backbone expressions using the frequency responses. We select the data marked as red circles in Fig. 6.7a to fit the surface described by Eq. (6.11a), as shown in Fig. 6.7b. With the measured ω^2, A_1^2 and A_2^2 from one frequency sweep, we can simultaneously fit for the three unknowns ω_1, β_1 and γ. The values of ω_2 and β_2 can be obtained by fitting the frequency responses obtained by driving the system around ω_2 in the nonlinear regime.

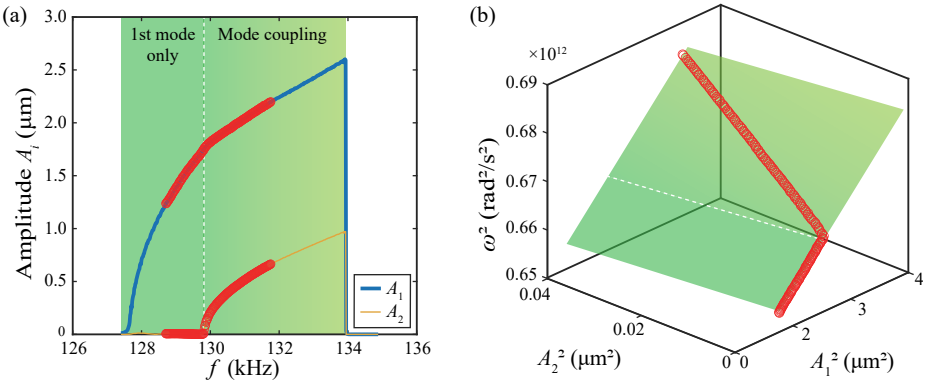

Figure 6.7: **Fitting the nonlinear coefficients of a 2-dof nonlinear dynamical system exhibits dispersive coupling in a single frequency sweep.** (a) The measured coupled response between the lowest two OOP modes are from the device with $w_s = 1\,\mu$m, $L_s = 90\,\mu$m, and $\theta = 0$. The bold blue line represents the frequency response of the driven first OOP mode, which is demodulated with the driven frequency (f). The yellow line represents the frequency response of the second OOP mode, which is demodulated with twice the driven frequency ($2f$). The selected data for fitting are marked as red circles. (b) The fitted surface described by Eq. (6.11a) with the selected data.

6.7.4. MEASUREMENT DATA OF THE COUPLED DYNAMICS FOR THE LOWEST TWO OOP MODES

In Table 6.1, we provide all the measured values (solid diamonds and triangles) in Fig. 6.2b, d and e. The resonance frequencies f_1, f_2 and nonlinear coefficients β_1, β_2, γ are fitted from measured frequency response curves using the method introduced in Appendix Section 6.7.3. The onset frequency $f_{1,c}$ and the onset amplitude $A_{1,c}$ of the coupled response are directly determined from the measured frequency response curves.

6.7.5. MULTI-MODE DISPERSIVE COUPLING

To study the tuning effect due to successive mode couplings in a string resonator, here we derive the expression of the effective Duffing constant of the first mode undergoing dispersive couplings with higher-order modes. For simplicity, we only consider coupling terms that are derived from the interaction potential $\frac{1}{2}\gamma_{1,i}A_1^2A_i^2$ ($i \geq 2$). This approximation neglects the interactions of the coupled mode with modes other than the first mode.

Table 6.1: Measurement data in Fig. 6.2b, d and e

L_s(μm)	f_1(Hz)	f_2(Hz)	β_1($m^{-2}s^{-2}$)	β_2($m^{-2}s^{-2}$)	γ($m^{-2}s^{-2}$)	$\Delta f_{1,c}$(Hz)	$A_{1,c}$(μm)
130	93700	189958	5.21×10^{21}	3.76×10^{22}	1.80×10^{22}	97157	2.48
110	107676	217257	6.81×10^{21}	5.93×10^{22}	2.40×10^{22}	110179	2.30
90	127701	256128	8.60×10^{21}	1.49×10^{23}	3.80×10^{22}	129810	1.77
70	156532	314299	1.17×10^{22}	1.83×10^{23}	3.44×10^{22}	158005	1.44
50	207892	416427	2.01×10^{22}	2.92×10^{23}	6.07×10^{22}	208676	0.92
30	347320	694724	7.73×10^{22}	1.66×10^{24}	9.33×10^{22}	347739	0.46

Similar to our approach in deriving Eqs. (6.11a) and (6.11b), if we consider the effective backbone of the first mode is coupled with the ith mode, we have:

$$4\omega^2 = 4\omega_{1,\mathrm{eff}}^{(i-1)^2} + 3\beta_{1,\mathrm{eff}}^{(i-1)} A_1^2 + 2\gamma_{1,i} A_i^2, \tag{6.19a}$$

$$4i^2\omega^2 = 4\omega_i^2 + 2\gamma_{1,i} A_1^2 + 3\beta_i A_i^2, \tag{6.19b}$$

where β_i is the Duffing constant of the ith mode, $\gamma_{1,i}$ is the dispersive coupling strength between the first and ith mode. By eliminating A_i from Eqs. (6.19a) and (6.19b), we can derive the new effective Duffing constant of the first mode:

$$\beta_{1,\mathrm{eff}}^{(i)} = \frac{9\beta_{1,\mathrm{eff}}^{(i-1)}\beta_i - 4\gamma_{1,i}^2}{12\beta_i - 8i^2\gamma_{1,i}}. \tag{6.20}$$

By separating $\frac{3}{4}\beta_{1,\mathrm{eff}}^{(i-1)}$ from Eq. (6.20), we can quantitatively visualize the influence of successive coupled modes on the Duffing constant:

$$\beta_{1,\mathrm{eff}}^{(i)} = \frac{3}{4}\beta_{1,\mathrm{eff}}^{(i-1)} + \frac{3i^2\beta_{1,\mathrm{eff}}^{(i-1)}\gamma_{1,i} - 2\gamma_{1,i}^2}{6\beta_i - 4i^2\gamma_{1,i}}. \tag{6.21}$$

In Table 6.2, we present the dynamical parameters obtained by the FE-based ROMs for the device in Fig. 6.3a. The effective Duffing constants $\beta_{1,\mathrm{eff}}^{(i)}$ during successive dispersive couplings are calculated using Eq. (6.21), based on the Duffing constants of different modes and their dispersive coupling coefficients with the first mode. The increasing values of $(\beta_{1,\mathrm{eff}}^{(i)} - \beta_1)/\beta_1$ demonstrate that the effective Duffing constant of the first mode can be significantly tuned via successive couplings to other vibrational modes.

Table 6.2: Tuning of the effective Duffing constant $\beta_{1,\mathrm{eff}}^{(i)}$ by successive dispersive mode coupling

Mode number	1	2	3	4	5
β_i($m^{-2}s^{-2}$)	3.76×10^{22}	5.44×10^{23}	2.73×10^{24}	8.61×10^{24}	2.10×10^{25}
$\gamma_{1,i}$($m^{-2}s^{-2}$)	—	1.58×10^{23}	3.53×10^{23}	6.22×10^{23}	9.70×10^{23}
$\beta_{1,\mathrm{eff}}^{(i)}$($m^{-2}s^{-2}$)	—	5.72×10^{22}	1.24×10^{23}	3.39×10^{23}	1.04×10^{24}

To more quantitatively show the tunability of the driven mode's response by incorporating multiple coupled modes, in Fig. 6.8, we simulate the frequency response of our

string resonators with $w_s = 1\mu m$, $\theta = 0$ and varying L_s with FE-based ROMs up to five modes. We can see the flattening of the frequency response of the first mode of the device with $L_s = 50\mu m$ (same with Fig. 6.3a in the main text) and even the drop in the one with $L_s = 30\mu m$, which represent the effective Duffing constant $\beta_{1,\text{eff}} \to \infty$ and $\beta_{1,\text{eff}} < 0$, respectively. The additional tuning effect compared to the values shown in Table 6.2 is attributed to the inclusion of all coupling terms related to cubic geometric nonlinearity in the FE-based ROMs, as opposed to the assumption for Eq. (6.21). Both analytical and numerical investigations confirm that, through geometric design and multi-mode interaction, one can engineer the coupled dynamical response of a resonator to a large extent.

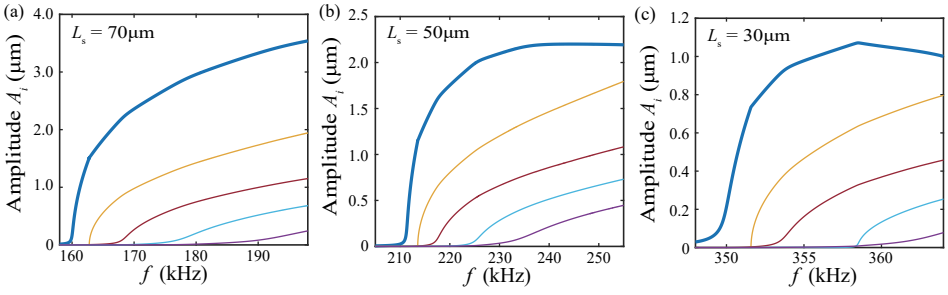

Figure 6.8: **Simulated frequency response curves based on FE-based ROMs under multi-mode coupling of devices with different support lengths.** The first modes of all three devices is driven by forward frequency sweeps at the same drive level. The blue, yellow, ochre, cyan and purple lines represent the first to the fifth OOP modes, respectively.

BIBLIOGRAPHY

[1] S. O. Erbil, U. Hatipoglu, C. Yanik, M. Ghavami, A. B. Ari, M. Yuksel, and M. S. Hanay, "Full electrostatic control of nanomechanical buckling", Physical Review Letters **124**, 046101 (2020).

[2] X. Chen, T. de Lint, F. Alijani, and P. G. Steeneken, "Nonlinear dynamics of diamagnetically levitating resonators", Nonlinear Dynamics **112**, 18807–18816 (2024).

[3] F. Bayram, D. Gajula, D. Khan, and G. Koley, "Mechanical memory operations in piezotransistive GaN microcantilevers using au nanoparticle-enhanced photoacoustic excitation", Microsystems & Nanoengineering **8**, 1–14 (2022).

[4] J. Güttinger, A. Noury, P. Weber, A. M. Eriksson, C. Lagoin, J. Moser, C. Eichler, A. Wallraff, A. Isacsson, and A. Bachtold, "Energy-dependent path of dissipation in nanomechanical resonators", Nature Nanotechnology **12**, 631–636 (2017).

[5] A. Keşkekler, O. Shoshani, M. Lee, H. S. van der Zant, P. G. Steeneken, and F. Alijani, "Tuning nonlinear damping in graphene nanoresonators by parametric–direct internal resonance", Nature communications **12**, 1–7 (2021).

[6] K. Asadi, J. Yu, and H. Cho, "Nonlinear couplings and energy transfers in micro-and nano-mechanical resonators: intermodal coupling, internal resonance and synchronization", Philosophical Transactions of the Royal Society A: Mathematical, Physical and Engineering Sciences **376**, 20170141 (2018).

[7] M. Fu, O. Ameye, F. Yang, J. Košata, J. del Pino, O. Zilberberg, and E. Scheer, *Fluctuation instabilities via internal resonance in a multimode membrane as a mechanism for frequency combs*, 2024.

[8] M. Monteil, C. Touzé, O. Thomas, and S. Benacchio, "Nonlinear forced vibrations of thin structures with tuned eigenfrequencies: the cases of 1: 2: 4 and 1: 2: 2 internal resonances", Nonlinear Dynamics **75**, 175–200 (2014).

[9] D. Antonio, D. H. Zanette, and D. López, "Frequency stabilization in nonlinear micromechanical oscillators", Nature Communications **3**, 806 (2012).

[10] O. Shoshani, S. Strachan, D. Czaplewski, D. Lopez, and S. W. Shaw, "Extraordinary frequency stabilization by resonant nonlinear mode coupling", Physical Review Applied **22**, 054055 (2024).

[11] L.-Q. Chen and Y. Fan, "Internal resonance vibration-based energy harvesting", Nonlinear Dynamics **111**, 11703–11727 (2023).

[12] A. Keskekler, H. Arjmandi-Tash, P. G. Steeneken, and F. Alijani, "Symmetry-breaking-induced frequency combs in graphene resonators", Nano Letters **22**, 6048–6054 (2022).

[13] J. Sun, S. Yu, H. Zhang, D. Chen, X. Zhou, C. Zhao, D. D. Gerrard, R. Kwon, G. Vukasin, D. Xiao, et al., "Generation and evolution of phononic frequency combs via coherent energy transfer between mechanical modes", Physical Review Applied **19**, 014031 (2023).

[14] Y. Yang, E. Ng, P. Polunin, Y. Chen, S. Strachan, V. Hong, C. H. Ahn, O. Shoshani, S. Shaw, M. Dykman, et al., "Experimental investigation on mode coupling of bulk mode silicon mems resonators", in 2015 28th ieee international conference on micro electro mechanical systems (mems) (IEEE, 2015), pp. 1008–1011.

[15] O. Shoshani and S. W. Shaw, "Resonant modal interactions in micro/nano-mechanical structures", Nonlinear Dynamics **104**, 1801–1828 (2021).

[16] P. Zhang, Y. Jia, S. Yuan, Z. Liu, and R. Yang, "Tunable stochastic state switching in 2d mos2 nanomechanical resonators with nonlinear mode coupling and internal resonance", Nano Letters **24**, 11043–11050 (2024).

[17] T. Kaisar, J. Lee, D. Li, S. W. Shaw, and P. X.-L. Feng, "Nonlinear stiffness and nonlinear damping in atomically thin mos2 nanomechanical resonators", Nano Letters **22**, 9831–9838 (2022).

[18] M. H. de Jong, A. Ganesan, A. Cupertino, S. Gröblacher, and R. A. Norte, "Mechanical overtone frequency combs", Nature Communications **14**, 1458 (2023).

[19] P. Belardinelli, W. Yang, A. Bachtold, M. Dykman, and F. Alijani, "Hidden mechanical oscillatory state in a carbon nanotube revealed by noise", arXiv preprint arXiv:2312.14034 (2023).

[20] Z. Li, M. Xu, R. A. Norte, A. M. Aragón, F. van Keulen, F. Alijani, and P. G. Steeneken, "Tuning the Q-factor of nanomechanical string resonators by torsion support design", Applied Physics Letters **122**, 013501 (2023).

[21] D. Shin, A. Cupertino, M. H. de Jong, P. G. Steeneken, M. A. Bessa, and R. A. Norte, "Spiderweb nanomechanical resonators via bayesian optimization: inspired by nature and guided by machine learning", Advanced Materials, 2106248.

[22] S. A. Fedorov, A. Beccari, N. J. Engelsen, and T. J. Kippenberg, "Fractal-like mechanical resonators with a soft-clamped fundamental mode", Physical Review Letters **124**, 025502 (2020).

[23] Z. Li, M. Xu, R. A. Norte, A. M. Aragón, P. G. Steeneken, and F. Alijani, "Strain engineering of nonlinear nanoresonators from hardening to softening", Communications Physics **7**, 53 (2024).

[24] A. H. Nayfeh and D. T. Mook, *Nonlinear oscillations* (John Wiley & Sons, 2008).

[25] S. Schmid, L. G. Villanueva, and M. L. Roukes, *Fundamentals of nanomechanical resonators*, Vol. 49 (Springer, 2016).

[26] A. A. Muravyov and S. A. Rizzi, "Determination of nonlinear stiffness with application to random vibration of geometrically nonlinear structures", Computers & Structures **81**, 1513–1523 (2003).

[27] A. Keşkekler, V. Bos, A. M. Aragón, P. G. Steeneken, and F. Alijani, "Multimode nonlinear dynamics of graphene resonators", Physical Review Applied **20**, 064020 (2023).

[28] A. Dhooge, W. Govaerts, Y. A. Kuznetsov, H. G. E. Meijer, and B. Sautois, "New features of the software matcont for bifurcation analysis of dynamical systems", Mathematical and Computer Modelling of Dynamical Systems **14**, 147–175 (2008).

[29] F. Yang, F. Hellbach, F. Rochau, W. Belzig, E. M. Weig, G. Rastelli, and E. Scheer, "Persistent response in an ultrastrongly driven mechanical membrane resonator", Physical Review Letters **127**, 014304 (2021).

[30] D. Antonio, D. H. Zanette, and D. López, "Frequency stabilization in nonlinear micromechanical oscillators", Nature Communications **3**, 1–6 (2012).

[31] C. Chen, D. H. Zanette, D. A. Czaplewski, S. Shaw, and D. López, "Direct observation of coherent energy transfer in nonlinear micromechanical oscillators", Nature Communications **8**, 1–7 (2017).

[32] C. A. C. Coello, G. T. Pulido, and M. S. Lechuga, "Handling multiple objectives with particle swarm optimization", IEEE Transactions on Evolutionary Computation **8**, 256–279 (2004).

[33] Z. Li, F. Alijani, A. Sarafraz, M. Xu, R. A. Norte, A. M. Aragón, and P. G. Steeneken, "Finite element-based nonlinear dynamic optimization of nanomechanical resonators", Microsystems & Nanoengineering **11**, 16 (2025).

[34] D. A. Czaplewski, C. Chen, D. Lopez, O. Shoshani, A. M. Eriksson, S. Strachan, and S. W. Shaw, "Bifurcation generated mechanical frequency comb", Physical Review Letters **121**, 244302 (2018).

[35] L. Wang, P. Zhang, Z. Liu, Z. Wang, and R. Yang, "On-chip mechanical computing: status, challenges, and opportunities", Chip **2**, 100038 (2023).

[36] N. Casilli, T. Kaisar, L. Colombo, S. Ghosh, P. X.-L. Feng, and C. Cassella, "Parametric frequency divider based ising machines", Physical Review Letters **132**, 147301 (2024).

[37] P. Álvarez, D. Pittilini, F. Miserocchi, S. Raamamurthy, G. Margiani, O. Ameye, J. Del Pino, O. Zilberberg, and A. Eichler, "Biased ising model using two coupled kerr parametric oscillators with external force", Physical Review Letters **132**, 207401 (2024).

[38] B. Hauer, C. Doolin, K. Beach, and J. Davis, "A general procedure for thermomechanical calibration of nano/micro-mechanical resonators", Annals of Physics **339**, 181–207 (2013).

7

7

Conclusions and outlook

This thesis focuses on optimizing the dynamics of nanomechanical resonators. Using lithographically fabricated nanostrings, we explored both the linear and nonlinear behaviors of these devices, encompassing single-mode responses as well as interactions among multiple modes. We developed experimental techniques for rapid and precise characterization of nonlinear dynamic responses, which can be accurately explained by analytical and numerical simulations. Based on the experimentally validated modeling techniques, we established a broadly applicable optimization framework, leveraging finite element-based reduced-order models and a gradient-free optimization technique, to engineer the mechanical properties of resonators. This final chapter summarizes the key results from each chapter and outlines potential future research directions.

7.1. CONCLUSIONS

7.1.1. INTRODUCTION AND METHODOLOGY

In Chapter 1, we discussed the background and motivation for optimizing nonlinear dynamics in nanomechanical systems. We introduced the design opportunities that linear and nonlinear mechanics offer in MEMS and NEMS, followed by an overview of the techniques relevant to incorporating nonlinearity.

In Chapter 2, we presented the experimental and theoretical methodologies employed in this thesis. The experimental section covered the fabrication techniques for nanomechanical Si_3N_4 devices, the measurement set-up with laser Doppler vibrometer, and the fast characterization approaches for assessing the linear and nonlinear dynamics of the devices. We proposed a technique for the measurement of geometric nonlinearity under frequency drift, which commonly exist in micro- and nanoresonators. This can lead to the change of frequency response curves with time that distorts the backbone curve, deteriorating the fitting procedure of the Duffing constant. In this thesis, we mainly focused on nanostring resonators with a pair of soft-clamping beams to demonstrate our strategies about engineering dynamical properties by the geometric design. In order to capture the influence of soft-clamping supports, the theoretical section started with a static analysis of the softly clamped high-stress string, followed by the derivation of its governing equations as a nonlinear resonator. Finally, we elaborated on the widely applicable procedure of building finite element (FE)-based reduced order models (ROMs) for nonlinear resonators, which are used throughout the thesis to explain the observed physics and build the basis for the geometric optimization.

7.1.2. ENGINEERING SINGLE-MODE NANOMECHANICAL RESONATORS

In this thesis we chose to experiment with Si_3N_4 nanomechanical resonators as they offer high-Q factors and at the same time low onset of nonlinearities which facilitate nonlinear dynamic studies. Since both linear and nonlinear dynamics of a resonator are closely tied to its stress, we proposed incorporating a pair of compliant supports to adjust the stress in the nanostrings. In Chapter 3, we analyzed the impact of this specific support design in tuning the stress in the central string accordingly. We found these supports can function as soft-clamping that that allowed us to tune the dissipation dilution in the string resonator. Through both analytical models and fabricated Si_3N_4 nanomechanical devices, we revealed the trade-off between stress and clamping stiffness in tuning both resonance frequencies and Q-factors. This finding consequently suggested that resonators exhibiting perimeter modes with periodic clamping can take advantage of soft-clamping, while maintaining the initial high stress. Our study provides insights into approaching dissipation limits in high-Q nanoresonators with a confined design footprint.

After the thorough study of dynamical properties in linear regime, such as resonance frequencies and Q-factors, we found that the supports could also significantly tune the geometric nonlinearity if the devices are driven stronger in the nonlinear regime. In Chapter 4, we proposed an analytical model that can show the tunability of nonlinear stiffness through compliant supports. Next, by introducing the support angle as an additional design variable, we showed that it is possible to induce compressive forces in

the string resonator and obtain buckled configurations. This breaking of symmetry in vibrations results in quadratic nonlinear terms in the equations of motions, that compete with the cubic (Duffing) nonlinear terms when buckled resonators enter the nonlinear regime. Being able to tune both linear and nonlinear properties of the string resonators using soft-clamping supports, we investigated the tunability of dynamic range (DR) using the support design, demonstrating that the design could either extend or reduce DR. Furthermore, by FE-based ROMs, we were able to quantify the influence from soft-clamping supports on nonlinear dynamic responses of nanoresonators, showing the possibilities to program nanodevices with different functionalities on a single chip.

7.1.3. DYNAMIC OPTIMIZATION OF NANOMECHANICAL RESONATORS

Based on the validation of our FE-based ROMs by measurements in both linear and nonlinear regime, we were well-positioned to numerically design the highly coupled dynamical properties of high-stress nanomechanical resonators. In Chapter 5, we integrated our modeling technique with a metaheuristic algorithm, specifically Particle Swarm Optimization (PSO). This algorithm, which can be accelerated through parallel computing and does not require derivative information, proved advantageous over brute-force parametric studies by significantly reducing the time required to locate optimal designs. Additionally, PSO is versatile in handling both single- and multi-objective optimization problems. We showed its capability and reliability by maximizing Q-factor and the cubic (Duffing) nonlinear coefficient, both individually and simultaneously. When dealing with multiple objectives, we could also visualize the trade-offs among them with a Pareto front. In this way, our optimization procedure allows for the design of resonators where multiple objectives need to be satisfied simultaneously.

7.1.4. ENGINEERING OF MODE COUPLING IN NANOMECHANICAL RESONATORS

To fully explore the design potential of soft-clamping supports, we further increased the drive levels to operate our Si_3N_4 nanostrings in the strong nonlinear regime. In Chapter 6, we observed modal interactions between different mechanical modes of our nanoresonators. To better understand and further exploit this nonlinear phenomenon, we first developed a model for a two-degree-of-freedom (2-DOF) dynamic system that consists of two modes undergoing mode coupling, and conducted a theoretical analysis on the impact of soft-clamping supports on mode coupling. Using the analytically derived expressions for the backbone curves of the 2-DOF system, we developed a fitting strategy for the rapid characterization of nonlinear properties in high-Q nanomechanical resonators undergoing mode coupling with one single frequency sweep. To achieve a greater tunability on the dynamic response of resonators, we experimentally and numerically showcased the multi-mode dispersive couplings involving up to five modes. Moreover, to demonstrate the geometric design potential offered by soft clamping, we also quantified and optimized the onset conditions of mode coupling and its tuning strength in the driven mode. The predictable intermodal couplings provide additional design opportunities for tuning nonlinear responses of nanomechanical resonators.

7.2. OUTLOOK

7.2.1. ADVANCING THE NONLINEAR DYNAMIC SIMULATION PROCEDURE

Simulation is the art of simplification, offering an idealized approximation of real experimental conditions. Achieving a balance between simulation accuracy and computational efficiency requires a thorough understanding of the essential physics to be incorporated. Our work derives the equations of motion solely from the geometry and material properties of nanomechanical resonators, eliminating the need for fitting parameters such as damping and stiffness terms. The simulated dynamic responses align closely with experimental measurements, as our ROMs effectively capture the underlying physics of the measured devices. However, this strong agreement between simulations and experiments relies on specific assumptions as I enumerate below:

On the one hand, this work primarily focused on damping from the friction loss, as our resonators operate at relatively low resonance frequencies (below 2 MHz) within a vacuum chamber. However, other sources of damping may play a significant role and should not be overlooked. For instance, the radiation loss caused by acoustic waves propagating into the surrounding substrate becomes increasingly important as the resonance frequency of the operational mode rises. Addressing this requires additional simulation steps, such as incorporating the substrate in the FE model and applying a Perfectly Matched Layer (PML) to calculate the radiation loss. PML is an artificial layer added to simulate an infinite domain by absorbing outgoing waves at the boundaries of the computational domain. Furthermore, in practical applications of micro- and nanomechanical resonators, such as resonant sensors that often operate in air or liquid environments, damping from the ambient environment typically dominates. To capture the influences arising from the viscous ambient, empirical formula or Fluid-Structure Interaction (FSI) simulations can be included to model damping from the medium loss.

On the other hand, considering the STiffness Evaluation Procedure (STEP) which is detailed in Chapter 2 for extracting nonlinear stiffnesses, we limited our formulation of nonlinearity up to cubic terms for simplicity. Higher-order nonlinearities may need to be incorporated as well to accurately predict dynamic responses in the strong nonlinear regime, or in cases of modeling nonlinearities in actuation or detection. Notably, based on our method for extracting nonlinear terms from FE analysis, this ROM technique could also evaluate nonlinear effects from multiphysics, such as electrostatic, magnetic, or optical forces that can be modeled as functions of vibration amplitude of the resonators.

Further work is expected to enhance the generality and scalability of the simulation procedure, which includes incorporating more damping sources and higher-order nonlinearities. By addressing these challenges, the simulation approach could turn into an even more versatile and comprehensive design framework for a broader range of applications, ranging from sensing and actuation to signal processing and energy harvesting.

7.2.2. BUCKLED NANORESONATORS

Nanomechanical resonators are gaining attention for their high force sensitivity and low energy loss, making them useful for sensing, transduction, and studying physics in classical and quantum systems. The need to enhance the signal-to-noise ratio (SNR) in sens-

ing and protect quantum states from decoherence have driven efforts to improve their mechanical Q-factors, as discussed in Chapter 3. However, in addition to our designed high-Q devices with tension, we anticipate a broad range of topics related to buckled resonators.

In Chapter 4, we have demonstrated that it is possible to create buckled configurations with a high-stress Si_3N_4 film by geometric design. In terms of linear dynamics, we have measured Q-factors on buckled devices with even lower values than the intrinsic Q-factor that are without dissipation dilution. In contrast to the flat devices under tension, this observation implied that the compressive force in the structure can lead to dissipation "concentration", which can be harnessed to intentionally decrease Q-factor. We foresee this strategy can facilitate the design of metamaterials for achieving extreme vibration suppression in micro- and nano-devices.

Regarding nonlinear dynamics in buckled nanoresonators, we observed that the geometric hardening nonlinearity can be largely nullified by the softening nonlinearity arising from the symmetry-breaking vibrations right after the onset of its buckling. By leveraging these two opposing nonlinear effects, we can finely adjust the geometry of a resonant sensor to achieve a much higher onset amplitude of nonlinearity, significantly improving the SNR. Apart from operating the structure dynamically, the minimized static stiffness right before the onset of buckling also offers the opportunity to detect minimal changes in various physical quantities, like the small variation in the local gravitational acceleration. As a result, it is worth comparing whether a resonant sensor with extremely high Q-factor or a non-resonant sensor with almost zero stiffness is more sensitive, based on different target objects and operating conditions.

Additionally, with the buckled resonators, we were able to detect secondary Hopf bifurcation and thus quasi-periodicity both numerically and experimentally. With our developed modeling technique, it is worth continuing to investigate the influence of geometric parameters on the generated frequency combs and possible chaos generation under higher drive levels. The pure mechanical way to achieve chaos would be an ideal test platform for understanding and engineering this fascinating phenomenon, since it minimizes noise introduced into the system by electrostatic or magnetic tuning schemes.

7.2.3. ENGINEERING NONLINEAR DYNAMICS BY TOPOLOGY OPTIMIZATION

In Chapter 5, we laid the foundation for nonlinear dynamic optimization of nanomechanical resonators, which is mainly based on size optimization of only a few geometric parameters in a limited design space. As the demand for smaller, more powerful chips continues to grow, maximizing space efficiency becomes a key challenge in MEMS/NEMS design. Linking ROM to topology optimization algorithms as a next step would offer the opportunity to fully exploit a limited design space by removing constraints on the number of design parameters inherent in size or shape optimization. Topology optimization has not only been used in solid mechanics, but has also extended its influence to a variety of other fields, including fluid mechanics, structural dynamics, electromagnetics, and even biomedical engineering. Originally developed for optimizing material distribution in solid structures to achieve the best mechanical performance, topology optimization has proven to be a powerful tool for solving a wide range of design challenges across different disciplines. For nanomechanical resonators

which is our primary focus, topology optimization has already been applied to optimize their linear dynamical properties, such as resonance frequencies and Q-factors. We envision the next step as integrating topology optimization with ROM techniques to tailor nonlinear properties.

However, for nonlinear ROM techniques, obtaining gradient information can be challenging when the nonlinear analysis involves iterative solvers, which is the case for STEP in our work. Instead, this obstacle can be circumvented by implementing a gradient-free topology optimization procedure with Binary Particle Swarm Optimization (BPSO), which is designed specifically for problems with binary ("0" or "1") design variables rather than continuous values. The design space could thus be discretized into fine pixels, each in a binary state: filled ("1") or void ("0"). Along with connectivity analysis to guarantee the continuity of the optimized design space, the BPSO will identify an optimal combination of "0"s and "1"s that generates a topologically new geometry. Like standard Particle Swarm Optimization (PSO), BPSO can efficiently explore a large search space. The swarm of particles in BPSO can explore multiple solutions simultaneously, increasing the chances of finding a global optimum, rather than getting stuck in the local optima, which is particularly useful in complex and highly nonlinear optimization problems. Besides, the nature of the PSO algorithm enables parallel exploration of the search space. This is a key advantage for large-scale problems, as multiple candidate designs (particles) are evaluated simultaneously, potentially speeding up the search process compared to other sequential optimization methods.

ACKNOWLEDGEMENTS

"What's past is prologue." — William Shakespeare, *The Tempest*

I feel incredibly fortunate to have joined TU Delft as a PhD candidate four years ago. Due to the pandemic, I arrived in the Netherlands during the strictest lockdown since World War II. This period challenged all of us, even those with the strongest resolve, but we made it through. I want to express my heartfelt gratitude to everyone I've encountered over these past four years. I'll do my best to capture as much as I can in writing, so that, even decades from now, my memories of you will remain vivid.

First, I want to express my sincere gratitude to my supervisory team. Throughout my four-year PhD journey, I had the privilege of learning from four remarkable gentlemen with different backgrounds and characteristics, each bringing unique expertise and perspectives. **Farbod**, you are an incredible blend of many excellent traits. As a teacher, you are one of the most welcomed and, who won the Best Teacher Award for three times. As a researcher, your sharp intuition allows you to swiftly identify key insights and seamlessly navigate diverse projects, ranging from from studying bacteria on graphene to applying machine learning to aircraft coatings. As a manager, you successfully secured highly competitive grants and hosted prestigious international conferences one after another. Most importantly, as a supervisor, you have been consistently present on the front lines of research, working alongside me. I still vividly recall the hours we spent together using Mathematica to derive the closed-form solutions for a stressed doubly clamped beam. Apart from other activities that demonstrate your omnipotence, I genuinely believe your passion and wisdom will propel you toward even greater opportunities to showcase your exceptional talent.

Peter, you are the one who I would like to model myself after in the future. It's rare to find someone who maintains such strong enthusiasm for both research and people. You consistently come up with compelling ideas based on current research, while also nurturing everyone's curiosity for new knowledge. Your pursuit for the analytical explanation and improvement in details continuously expands the boundaries of my understanding in my research. Every interaction with you is as pleasant as a gentle spring breeze. Your quick responses to every request ensure I never feel helpless, even late at night or during weekends—a sentiment echoed by other DMN members as well. I often marvel at how you manage to be so responsible for everyone, which requires both unwavering determination and immense energy. Your selfless dedication, even at the expense of your own leisure time, inspires others to follow your lead. I am confident that under your management, both the DMN group and the PME department will continuously thrive.

Alejandro, you are the vigilant watcher for the optimization part in my work. You are rigorous about the details and motivates me with your infectious confidence. Thanks for

understanding and sometimes helping to explain my concerns about technical details during the weekly meetings. Your passion and directness add great value to our meetings, providing a perfect balance to my more conservative tendencies.

Fred, your questions are always right to the point that some of those I can fully understand after further study. I will also keep your customized suggestions about my career in minds, and hopefully one day, I can prove that I have successfully put them into practice. By the way, thanks for the recommendation of the website for cycling routes, I have thoroughly enjoyed recording numerous vlogs of my rides and the breathtaking scenery along the country roads of the Netherlands. I believe Faculty of Mechanical Engineering will become better and better under your leadership.

Meanwhile, I greatly appreciate the financial support from China Scholarship Council, without which my PhD research would not be possible.

I would like to extend my heartfelt gratitude to all the committee members, including Prof. Herre van der Zant, Prof. Steven W. Shaw, Prof. Silvan Schmid, Dr. Alexander Eichler, and the reserve member Prof. Urs Staufer, for dedicating their valuable time to read my thesis and give comments. Thank you for accepting the role of being on the committee and I am looking forward to our discussions.

Amidst Farbod's two ERC grants, ENIGMA and NCANTO, I have witnessed the successful graduation of numerous PhD students and the start of many new academic journeys. **Xianfeng**, the first Chinese in DMN who worked with diamagnetic levitation. You remain humble despite being a master in many areas, from LDV measurement to ping pong. Your resilience and wisdom beneath the calm exterior are lessons that I will try to learn forever. Thank you for sharing your experiences on different topics. With your unwavering determination and resourceful mind, I have no doubt you will become a successful researcher. **Ata**, my comrade in nonlinear dynamics. I heard about your legendary deeds during Covid time, but it wasn't until ENOC2020+2 in Lyon that I truly experienced your style firsthand. I was impressed by your questions and discussions with other researchers, which showcased your deep understanding of nonlinear phenomena. Beyond research, you are the DJ for all parties we have, always bringing energy to the atmosphere. The "3 eggs + yogurt (+ avocado)" muscle-building diet is something I might try—if my stomach can handle it. I will treasure the memory of our the fruitful discussions on nonlinear dynamics and life. I look forward to your future works that demonstrate your talents in your chosen field, like the impact you already made on graphene drums, racket net and guitar strings. Thank you for taking the time to be my paranymph despite your busy schedule. **Irek**, the energetic CEO with an infectious smile. You are always confident of your work and make good use of the resources you have. I first noticed your exceptional ability in business during our graduate school course Effective Negotiation. You bargained so skillfully that your poor counterpart had to make major concessions. I eagerly await the day I see SoundCell making headlines on TV. **Ali**, a rigorous researcher with exceptional enthusiasm and profession in mechanical details, whose comments always remind me of the research field where I came from. Thanks for showing me the tricks of using the cluster and teaching me Farsi. **Abhilash**, the professional bodybuilder with a tough exterior yet a love for cute Japanese anime. My salute to a quietly reliable friend. **Nick**, our conversations never seem to run out of topics. You are systematic in your research and uphold a strong sense of order in your life. You surprised

me with your broad knowledge about international histories, even Chinese ancient classics. I enjoy the discussions with you and I am certain you will definitely be influential in the future, not only in academia. **Santiago**, the machine learning expert with extraordinary presentation skills. You told me you usually practice for that at home, but I do think you have a talent to convey your ideas clearly and persuasively. **Lara**, an enthusiastic lady with sharp mind. Thanks for sharing the delicious cake you made on your birthday, which tasted just as good as any store-bought one. **Kushal**, even though we have only few interactions, I could sense the responsibility and reliability from you during our TA for Nonlinear Dynamics. I knew Farbod had selected the right person for his biological project. **Enise**, as the only PhD candidate who joined our group from another university in a different country, you've shown remarkable adaptability and skill in extending your expertise from Si_3N_4 to 2D materials—something truly impressive. **Chris**, the *Cum Laude* with outstanding talent in coordination and management. The calm smile on your face always conveys a confident assurance that everything is under control. As an independent researcher who solve problems in an orderly manner, I am sure you will achieve even greater success during your PhD journey. Thank you for helping me translate the abstract of this thesis into Dutch. **Zhiwei**, a zodiac enthusiast with a talent for thinking and planning. You indeed bring energy to everyone during tea breaks, perfectly in line with your fiery zodiac sign. Thank you for introducing me to biological experiments. **Alberto**, our optics expert with broad knowledge in micro- and nanosystems. Thank you for providing a thorough introduction to the measurement techniques and for creating a comprehensive guidebook for the experimental setups. Meanwhile, I also want to mention **Sandro**, **Makar**,**Hadi**, **Arthur**, **Giovanni**, who were previously part of the group. Thank you all for your valuable suggestions and comments during our discussions—I deeply appreciate them.

Since my entire PhD journey has revolved around working with Si_3N_4, I've frequently collaborated with Richard's group. **Richard**, you consistently bring insightful comments and fascinating ideas to our DMN meetings. Your quick strides around PME square mirror the speed of your thoughts. I appreciate all your constructive suggestions on my papers and inspiring conversations we've had about the cutting-edge possibilities about nanomechanics. **Minxing**, a.k.a "Dalao", Sage of Kavli Nanolab, Tiger of Wall Street, God of Texas Hold'em, etc. Despite your enthusiasm for a wide range of business plans, you remain a true purist towards your research project as a PhD candidate. Thanks for helping me get started with the measurement of Si_3N_4 strings and improve my tennis skills. I'll always treasure the times we brainstormed research ideas and the heated discussions on news around the world. **Lucas**, the noise-maker next to me. Your contagious laughter and sharp sense of humor never fail to lift the spirits of those around you. Thanks for the invitation to your BBQ, and I really enjoyed the medium-rare steak for the first time. I hope one day you'll launch the Si_3N_4 sail beyond the Milky Way–so I can point to the sky and proudly say, "I know the guy who did that." **Andrea**, another expert on nanofabrications endlessly chasing crazy aspect ratios for the ever-vibrating nanostrings. At the same time, you are the one with inclusive international visions and enthusiastic about improving communications between PhDs and their supervisors. I admire your commitment to the greater good and wish you all the best in your efforts. **Dongil**, another expert in machine learning. I want to thank you for the meetings we had at the start of

my PhD project, where you gave an introduction of Beyesian optimization and showed me simulation techniques for *Q*-factor analysis. **Matthijs**, an optomehanical physicist with a meticulous approach to both his research and his life. You have a unique talent for storytelling—your rich life experiences always draw everyone in. It's been a pleasure learning from both your research and your tales.

There are more stories to tell in the DMN group. **Gerard**, just as your appropriate comments on our presentations are always spot-on, your passes on the soccer field are equally precise. It's a real pleasure playing alongside such a skilled playmaker. **Sabina**, the rising star of DMN–I'm constantly amazed at how much you've accomplished so early in your career. Thank you for organizing the group activities that have brought everyone closer together. **Wouter**, I appreciate your research style that seamlessly bridges practical applications and academic theories. I hope you will get well soon. **Hanqing**, the most hard-working and optimistic one. Rarely, you have the keen insight and the strong execution at the same time. Thank you for assisting me during the application and beginning of my PhD. I wish you score more points on the basketball court and become Prof. Liu soon. **Ruben**, one of the nicest person I've ever met. You always behave like the warm-hearted protagonist we often see in anime–always gentle, caring, and enthusiastic about looking out for those around you. Besides, I am also impressed by the breadth of research interests, as evidenced by the insightful comments you provided on others' works. **Satadal**, the one with extensive knowledge and serves as a translator between humans and plants. I still remember the suggestions you gave me about weekly meetings, from which I have benefited a lot. **Xiliang**, the wizard of femtosecond laser cutter, always full of brilliant ideas for harnessing the power of light. Coming from the old capital of ancient China, you are dedicated to organizing group activities and promoting traditional Chinese culture at the same time. I believe you will excel just as much in your future career. Thank you for taking the time to be my paranymph. **Ze**, my good old brother who manipulates DNA. I was amazed to discover that we attended the same high school when we first met in a foreign land. Congratulations on rekindling your bond with Nankai and embracing your new role as a father. I wish you, Xiaotong, and your newborn baby all the happiness in the future. **Tufan**, the calm voice and slow speaking imply your steadiness and wisdom, which correspond to the roles you play in DOTA. I will keep an eye on our plan for the poster business. **Hande**, thanks so much for showing me how to make 2D resonators–and for patiently explaining the origin of Turkish family names. **Paulina**, thank you for the introduction of Canary Islands–we had a wonderful time exploring and really enjoyed the trip. **Vincent**, an intelligent researcher with incredible contributions during master project. Thanks for transferring your neat and well-commented codes to me as well as the detailed instructions during our meetings. I wish you all the best for your PhD study and some day to be rewarded for your kindness. **Frederike**, thank you for organizing the research coffee with Ruben, which is an nice innovation for people in the department to get to know each other's research. **Daria**, **Sahar**, **Mohammadjavad**, **Megha**, **Murat**, **Kai**, **Martin**, **Dong Hoon**, thank you all for making DMN feel like a home where everyone can progress together.

In the PME department, I want to begin by expressing my gratitude to all our PIs. You serve as role models for us in many aspects. **Hans**, the prop guide for medieval films as part-time hobbies, I appreciate your style and enjoy talking with you when we are

waiting for the boiling water for our tea. **Murali**, the expert with broad knowledge about MEMS/NEMS. I can always learn something from our discussions. **Davood**, during our supervision of master projects together with Farbod, I found you could easily come up with ideas to achieve desired motions with compliant mechanism. I find your research fascinating and will follow your research. **Matthijs**, thanks for the detailed and patient instructions when I started using the cluster. **Tomas**, my predecessor of the administrator for Polytec MSA400. Thank you for the professional instructions on Lock-in Amplifier and sharing the information about frequency stability. I hope you will be busy with different grants and successfully promoted as professor at EWI.

Besides, during the lunch time and coffee breaks, I really enjoy talking with people from different cultural backgrounds. **Endre**, one of the strongest trainers at the X gym, in contrast with his quiet voice. I was amazed when I saw you lift 80kg for the narrow-grip bench press. **Aditya**, a low-key researcher with excellent dribbling techniques on the soccer field. Thanks for helping me getting started with the cluster. **Casper**, the insightful thinker who is curious and reflects on almost everything. Our conversations are always in depth and inspiring. I am sure you are the one who deserves to be called the Doctor of Philosophy. **Nils**, the one always has a relaxed vibe that effortlessly lightens the atmosphere around you. **Joran**, the straightforward guy who shows inclusivity in his own way. Thanks for recommending the combination of baked bread and hummus–it has now replaced my old breakfast routine. **Stijn**, the master of optimization, always seen in his signature hoodie and hat. You are not only polishing your skills in research, but also in bouldering and management. I believe you will be a capable and cool supervisor for future generations. **Maarten**, another optimization expert with incredibly long papers. Thanks for the recommendation of papers for my problem. **Tanveer**, thanks for sharing your opinions about the society. I appreciate your rational and objective comments.

We also have many nice PhDs and Postdocs around PME, who make our department like a huge family. They are: **Domas**, **Pierre**, **Hava**, **Ahmed**, **Giulio**, **Francesco**, **George**, **Stavros**, **Serena**, **Qais**, **Aditya**, **Inge**, **Malte**, **Pieter**, **Marcin**, **Ali**, **Yoo-Seong**, **Marek**, **Dilek**, **Vivek**, **Thomas**, **Dave**, **Jelle**, ...This is quite a lengthy list, and I can't name everyone individually, but I wish you all the best of luck and success in your careers.

I would like to extend my gratitude to all support staff. I want to thank **Marli** for providing me facilities timely; **Sylviane** for arranging the monthly birthday celebration; **Spiridon**, **Gideon** and **Bradley** for helping me with measurement set-up meticulously; and **Lisette**, **Eveline**, **Gaby**, **Natalija**, **Birgit**, **Marianne**, **Annemieke**, **Xander**, **Rob**, **Patrick**, **Alex**, without whom my PhD journey would not have gone so smoothly.

Of course, my Chinese colleagues at PME worth being acknowledged separately, since we spent most of the leisure time together: **Yong**, **Jian**, **Yujiang**, **Xuerong**, **Huihui**, **Lidan**, **Zhichao**, **Kai**, **Xinxin**, **Binibin**, **Yuheng**, **Chao**, **Xueying**, **Yang**[2], **Sifeng**, **Mingkai**, **Zhilin**, **Ruibo**, **Peiyu**, **Yuchen** and **Rui**, I enjoyed all the parties, games and trips we had together. Your presence throughout my PhD has meant a lot–thank you.

In role of daily supervisors for master students, I did gain valuable insights from various perspectives. **Haolang**, like many Chinese student, you have all the merits that makes you a hard-working and humble researcher. I have witnessed your efficiency when the goal is clearly defined for you. I believe you have already brought your talents as a mechanical engineer back to China and contributed to the research in Huawei.

Hendrik, our Mr. *Cum Laude* attribute to the outstanding work you accomplished during the project. You are a quick learner with enthusiasm, that's why you can now speak and even type basic Chinese. Apart from the geometry of a resonator, you also know how to optimize the resources available to your research. I hope you all the best in your future PhD journey at Technion-Israel Institute of Technology. Including **Nick**, who has already enrolled in Farbod's group as a PhD candidate, I see parts of myself in all of you. You remind me of the ambitious and proactive young man I have always been.

Good health is the foundation of productivity. Throughout my PhD journey, I've been fortunate to have some comrades with whom I could relieve work stress through various forms of physical exercise. **Juncheng**, a reliable and sporty friend. We met in 2020 when queuing for our Covid vaccines. On the beautiful country roads of the Netherlands, we chased the wind with our bikes and broke our records one by one. In the gym, even though we have opposite goals for our body weights, we are both making progress (albeit with some difficulty). In addition, I've learned so much from you, including how to make Biangbiang noodles, cut hair, and your positive attitude towards life. I hope you and Jiechen all the happiness in the future. **Zhaochong**, my coach for bouldering with strong athletic talent. Your life is like a practice that you continuously challenge yourself under extreme conditions, including hiking in snow mountains and running Marathon. Based on the guidance you've given me in bouldering, I'm confident that you would make an excellent supervisor, with your clear and patient instructions for beginners. Congratulations on becoming a father recently! **Liqi**, another training partner in the gym whose strength is approaching competition level. Since we have to frequently change the barbell weights during our shifts (our strength levels are not even close), I hope this doesn't end up boosting your training volume too much. I benefit a lot from your training concepts and schedules.

At the same time, I also want to acknowledge my family members and friends in China. Thanks for your remote mental supports and hospitality when I was back. I will always remember and cherish the joy and laughter we shared, keeping those moments in my memory forever.

In the end, some words to **my parents**:

爸爸妈妈，感谢你们给我相对自由的成长环境，和一直以来对我选择的尊重与支持。
无论何时，你们都是我坚实的后盾和前进的动力。

Zichao Li
April 2025

Curriculum Vitæ

Zichao Li

06-10-1994 Born in Tianjin, China.

Education

2010–2013 High School
Tianjin Nankai High School
Tianjin, China

2013–2017 Bachelor of Engineering in Flying Vehicle Power Engineering
Beihang University, Beijing, China
Thesis: Analysis of Vibration Suppression in Thin-walled Gears Structure by Damper Rings
Promotor: Prof. dr. Yanrong Wang

2017–2020 Master of Engineering in Aerospace Propulsion Theory and Engineering
Beihang University, Beijing, China
Thesis: Analysis on Vibration Reduction Characteristics of Thin-walled Gear Structure with Ring Damper
Promotor: Prof. dr. Yanrong Wang

2020–2024 PhD in Precision and Microsystems Engineering
Delft University of Technology, Delft, The Netherlands
Thesis: Optimization of Nonlinear Dynamics in Nanomechanical Resonators
Promotor: Prof. dr. Peter G. Steeneken
Promotor: Dr. Farbod Alijani
Promotor: Dr. Alejandro M. Aragón

List of Publications

8. **Z. Li**, M. Xu, R. A. Norte, A. M. Aragón, P. G. Steeneken, F. Alijani, *Cascade of Modal Interactions in Nanomechanical Resonators with Soft Clamping*, under review, (2025).

7. H. J. Algra, **Z. Li**, M. Langelaar, F. Alijani, A. M. Aragón, *Dissipation Dilution-Driven Topology Optimization for Maximizing the Q-Factor of Nanomechanical Resonators*, under review, (2025).

6. **Z. Li**, F. Alijani, A. Sarafraz, M. Xu, R. A. Norte, A. M. Aragón, P. G. Steeneken, *Finite Element-based Nonlinear Dynamic Optimization of Nanomechanical Resonators*, published on: Microsystems & Nanoengineering, 11, 16, (2025).

5. **Z. Li**, M. Xu, R. A. Norte, A. M. Aragón, P. G. Steeneken, F. Alijani, *Strain Engineering of Nonlinear Nanoresonators from Hardening to Softening*, published on: Communications Physics, 7, 53 (2024).

4. **Z. Li**, M. Xu, R. A. Norte, A. M. Aragón, F. van Keulen, F. Alijani, P. G. Steeneken, *Tuning the Q-factor of Nanomechanical String Resonators by Torsion Support Design*, published on: Applied Physics Letters, 122, 013501 (2023).

3. **Z. Li**, Y. Wang, X. Jiang, H. Ye, W. Yang, *Energy Dissipation of Damper Rings for Thin-Walled Gears*, published on: Proceedings of ASME 2019 International Design Engineering Technical Conferences & Computers and Information in Engineering Conference, (2019).

2. **Z. Li**, Y. Wang, X. Jiang, Y. Wu, W. Yang, *The Optimal Design of Damper Rings for Aviation Gears*, published on: Proceedings of AIAA 2019 Propulsion and Energy Forum and Exposition, (2019).

1. W. Yang, Y. Wang, L. Han, X. Zhang, **Z. Li**, *Effect of Rotating Instabilities on Aerodynamic Damping of Axial Flow Fan Blades*, published on: Proceedings of ASME Turbo Expo 2019: Turbomachinery Technical Conference and Exposition, (2019).

ISBN 978-94-6384-776-6